Doctoral Dissertation

Optimal power system operation with dynamic line ratings for increased intermittent renewable energy utilization

間欠的な再生可能エネルギーの増加に向けた
動的送電定格を考慮した電力システムの最適運用手法

Bonface Oduor Ngoko

July 2018

Division of Electrical, Electronic, and Information Engineering
Graduate School of Engineering
Osaka University

To Mum,

for showing me the right way.

Abstract

This dissertation demonstrates the potential benefits that dynamic line rating (DLR) of overhead transmission lines can have on the utilization of intermittent renewable energy (IRE) sources i.e. solar photovoltaic (PV) and wind power. In contrast to the traditional static line rating (SLR) which is determined for worst-case conductor cooling conditions, the DLR of an overhead conductor is calculated in real-time using short-term forecasts of ambient weather conditions thereby almost always resulting in increased transmission line loadability. DLR therefore allows for more flexibility in the operation of the transmission system thereby reducing congestion that could impact power flow and optimal generation schedules. Increased power generation by IRE sources in power systems increases uncertainty in transmission line power flows and consequently increases the risk of violating conductor thermal limits. It is demonstrated in this thesis that a DLR approach on lines operated near their thermal limits could allow larger current/power fluctuations thereby impacting on the levels of utilizable IRE generation.

This thesis covers several aspects of power system operation with IRE sources and dynamic line ratings. First, a probabilistic model for solar PV power is presented. The model simulates high-temporal resolution (1-minute) fluctuations in solar irradiation as a Markov process. The empirically derived model can be used for probabilistic studies and assessments of various risks in the power system. It is used in this thesis to generate scenarios of solar power fluctuations for transmission line overload risk assessment. Secondly, a simple conductor temperature model that allows for fast estimation of the thermal status of a transmission line is presented. The model reduces the computational effort and computation time that would be required to include conductor temperature calculations in the determination of optimal system operation. The model used in this thesis explicitly incorporates conductor thermal dynamics in the solution of the optimal power flow (OPF) problem in a system with significant IRE generation. Finally, a new formulation of the optimal power flow problem is presented. The proposed formulation uses explicit conductor temperature limits instead of the traditional maximum current method and adds an uncertainty cost component to the objective function which offers a means of handling increased uncertainty in power generation due to IRE sources. Simulation results demonstrate the effect of the direct conductor temperature approach on the obtained optimal power generation schedules.

In general, this thesis presents strong arguments for power system operators to implement DLR of overhead transmission lines as a method of addressing the challenge of increased line flow fluctuations due to increased integration of IRE sources.

Acknowledgments

I have carried out the research described in this thesis during my PhD studies (Oct-2015 to Sept-2018) at the Division of Electrical, Electronic, and Information Engineering, Graduate School of Engineering, Osaka University under the guidance of Professor Tsuyoshi Funaki. During this period, I have had the help of many people and I would like to take this opportunity to sincerely thank all of them.

First and foremost, I would like to extend my heartfelt appreciation to Professor Tsuyoshi Funaki for his guidance, invaluable comments, paper revisions, and overall supervision throughout my postgraduate studies. I would also like to thank him for allowing me the opportunity to carry out my research in his laboratory. During this period I have learnt a lot from Professor Funaki and other members of the laboratory, not just in my own area of research but also in other topics both in power systems and power electronics.

I am also extremely grateful to my immediate supervisor, Associate Professor Hideharu Sugihara for his invaluable guidance, many hours of insightful discussions, and constant encouragement and support. Sugihara Sensei has without doubt shaped my research work and guided me to focus which has saved me lots of invaluable time and energy.

In addition, I am also extremely grateful to Associate Professor Hideharu Sugihara for allowing me to join his research group in the Japan Science and Technology (JST) agency CREST research project on system theory for harmonized power system control based on photovoltaic power prediction. The financial support that I have received from this project has made my PhD studies and general life in Japan much easier.

I would like to extend my sincere appreciation to Professor Shigemasa Takai and Professor Hiroyuki Shiraga for reviewing my thesis and serving as members of my dissertation committee. Their comments and insights have been really helpful.

I would also like to thank other members of staff from the Division of Electrical, Electronic, and Information Engineering, Graduate School of Engineering, Osaka University including Professor Toshifumi Ise, Associate Professor Yushi Miura, and Associate Professor Toshiyuki Miyamoto. I have learnt a lot from all of them during both my Masters and PhD studies.

I am also thankful to Assistant Professor Takaaki Ibuchi and other members of Funaki laboratory for their kind advice, useful comments, and great support throughout my stud-

ies. I would like to especially thank Ms. Fumie Imura from Funaki Laboratory for all the help and for being so kind.

A warm thanks to my PhD colleagues in the laboratory during my studies: Taehwa Kim, Natthawuth Somakettarin, Ramos Nino, Kei Hayashi, and Shuhei Fukunaga for creating a great work environment and for their honest friendship both in and out of the laboratory. I am especially grateful to Ramos-san for sharing the PhD study experience with me from literally the first day.

A special thank you goes to all the special friends I have made in Japan and who have supported me a great deal. I am especially thankful to the family of Dr. Donald Gagner and Ms. Midori Gagner for great support that I can never pay back and constant encouragement in both my studies and in my private life.

I would also like to state my sincere gratitude to the Japanese government, and, by extension, to all Japanese people for the financial and non-financial support I have received during my postgraduate studies. I feel blessed to have come to Japan and learnt a whole new way of life. The experience has without a doubt made me a better individual.

A deep felt thanks to my dad and mum back home in Kenya and to the rest of my family for their support and encouragement. Dad taught me how to understand mathematics thereby laying the foundation for all my studies and mum made life in this world much, much easier. I am really grateful for their selfless sacrifices.

Finally, I would like to thank my family in the most special way. My wife Adline who has been the truest meaning of the phrase *partner in life* and who has literally paused her own life for my sake. My appreciation to our lovely boys Brandon and Ryan who have been nothing but joy and support. I am eternally indebted to you guys. Thank you.

Bonface Oduor Ngoko
Osaka University, Osaka, Japan.
July 2018.

Contents

List of Figures

List of Tables

List of Acronyms

AC	Alternating current
ACF	Auto Correlation Function
ACSR	Aluminum Conductor Steel Reinforced
AIC	Akaike Information Criterion
AR	Auto Regressive
ARMA	Auto Regressive Moving Average
CIGRE	International Council on Large Electric Systems
CSP	Congestion Shadow Price
DC	Direct current
DOPF	Deterministic Optimal Power Flow
DETR	Dynamic Electro-Thermal Rating
DLR	Dynamic Line Rating
ED	Economic Dispatch
ETC	Electro-Thermal Coordination
HBE	Heat Balance Equation
IEEE	Institute of Electrical and Electronics Engineers
IEEJ	Institute of Electrical Engineers of Japan
IRE	Intermittent Renewable Energy
JMA	Japan Meteorological Agency
LMP	Locational Marginal Price
MIPS	MATLAB Interior Point Solver
MTM	Markov Transition Matrix
NLP	Non-Linear Programming
ODE	Ordinary Differential Equation
OPF	Optimal Power Flow
PACF	Partial Auto Correlation Function
PV	Photovoltaic
SLR	Static Line Rating
TACSR	Thermal-resistant Aluminum-alloy Conductor Steel Reinforced
UC	Unit Commitment

CHAPTER 1

Introduction

1.1 Background and motivation

The traditional sources of electricity generation i.e. hydro, nuclear, and fossil fuel (coal, oil and natural gas), etc., are to a large extent, controllable i.e. the output of the generators driven by these sources can be regulated by the plant operator. Such electricity generators are therefore referred to as being *dispatchable*. Intermittent renewable energy (IRE) sources i.e. solar photovoltaic (PV) and wind power are however *non-dispatchable* because, unlike the conventional sources of electricity generation, the input fuel i.e. solar radiation and blowing wind cannot be stored [1, 2]. Intermittency means that the outputs of these sources are variable and therefore uncertain. The amount of electricity that will be generated by a solar PV or wind based power plant cannot be guaranteed with a 100% accuracy. Even though forecasting models have improved over the years, the levels of uncertainty with IRE sources is still significantly higher than typical in traditional large power systems [3, 4]. In recent years, storage systems are becoming more economically viable e.g. large scale batteries can provide higher IRE output control, but these options are still relatively expensive [5]. The variability and uncertainty of IRE generation is thus a relatively new challenge to power system operators who have to ensure a constant balance between electric power demand and supply to ensure stability of the system [6, 7].

Recent literature on large scale integration of IRE sources in power networks provides various options to address the challenge of supply-demand balance due to the variability and uncertainty of IRE sources [8, 9, 10, 11, 12, 13]. The proposed options can broadly be divided into two categories. The first category targets stricter operating reserve settings [8, 9, 10] i.e. either increasing the capacity of fast responding generating units in the system to ensure that they can fully respond to the fluctuations in IRE output; or curtailing the IRE outputs at certain levels determined by the available fast acting spinning reserves in the system. Such operational rules are usually deterministically set from a conservative point-of-view hence they tend to lead to relatively expensive operation. The second approach is targeted at changes to system operational practices i.e. use less conservative rules in operation [11, 12, 13]. This option has the advantage of being less expensive in general but, on the flip side, many system operators are not comfortable with the higher levels of risk in system operation.

There are several options available to system operators in terms of changes to system operation including increased interconnection with neighboring areas, demand side management, and large-scale storage [14]. This dissertation focuses on a more dynamic utilization of the transmission network in what is generally referred to in the industry as *dynamic line rating* (DLR) [15, 16, 17]. The rating of overhead transmission lines can have a significant impact on the power flows in the network and consequently on the utilizability of IRE sources within the network. The traditional static line rating (SLR) is usually a conservative[1] value that could lead to network congestion and may necessitate IRE curtailment [18, 19]. On the other hand, the less conservative DLR has several benefits including leveling electricity prices, reduction of operational costs, and better contingency management [20, 21, 22, 23]. In this thesis, several aspects of DLRs are studied with the main focus being the effect on utilizability of IRE sources.

Given the background presented in the preceding paragraphs, the research detailed in this thesis is motivated by the realization that DLR of overhead transmission lines has the potential to increase the amount of utilizable IRE generation in power systems. Several topics are addressed including modeling of physical phenomenon, determination of simple safety factors for DLRs and finally the formulation and solution of a new optimal power flow model with DLR and IRE generation.

1.2 Objective

The main objective of this research was:

> *to develop a methodology for directly incorporating dynamic line rating of overhead transmission lines in optimal power system operation tools with the specific target of handling uncertainty due to intermittent renewable energy sources thereby increasing their utilizable capacity.*

1.3 Thesis contributions

The main outputs of the research published as journal and conference papers (see appendix A) are detailed as:

1. A probabilistic model for high temporal resolution solar radiation fluctuations is developed [24]. The model uses Markov transition matrices to simulate the stochastic transitions in 1-minute global solar irradiation data. The use of a Markov model correctly captures the statistical characteristics of high temporal resolution solar irradiation data as illustrated in the model validation section. The proposed model is used to synthetically generate scenarios of solar PV power (extrapolated[2] from

[1] A "conservative approach" to line rating refers to a situation in which the system operator targets as much as possible to ensure that the probability of line overload is practically zero.

[2] Starting from the generated solar irradiation data (in W/m^2), a multiplication factor that accounts for the area of solar panels (in m^2) and the system conversion efficiency (a dimensionless constant) is used to get solar power in Watts.

global solar radiation) in probabilistic studies with solar PV generation including the assessment of fluctuations in conductor current and, by extension, conductor temperature.

2. A simple mathematical model for estimating overhead conductor temperature under varying weather conditions is proposed [25]. The proposed model is used to quickly approximate the conductor temperature in both steady-state and transient-state conditions for given conductor current and ambient weather conditions. Mathematical and experimental validations of the proposed model are also detailed. The simplicity of the proposed model reduces the computational effort when integrating conductor thermal dynamics in the determination of optimal system operation i.e. optimal schedules for both thermal and IRE generation.

3. A new formulation of the optimal power flow (OPF) problem incorporating the thermal characteristics of overhead conductors for a system with significant IRE-source generation is proposed [26]. The conductor thermal characteristics are calculated from monitored weather parameters using the simplified conductor temperature model developed in [25] and described in point 2 above. The application of the proposed formulation is demonstrated using simulations on a standard test system with IRE generation. The simulations based on the proposed OPF formulation demonstrates the potential of dynamic line ratings in accommodating more uncertainty in the system due to IRE generation which translates to increased use of IRE sources.

1.4 Thesis outline

Chapter 2 gives an introductory description of the state of the art in power system operation with regard to intermittent renewable energy (IRE), transmission line ratings, and optimal scheduling. Recent trends in electric power generation by IRE sources and the operational challenges due to their variability and uncertainty are described. Also, a simple explanation in the difference between static line rating and dynamic line rating is given. Finally, the meaning of optimal system operation, specifically the optimal power flow problem is described with an explanation of the differences introduced by IRE generation and the application of dynamic line ratings.

Chapter 3 details a probabilistic model for high temporal resolution solar irradiation data that is used for synthetic generation of fluctuating solar PV scenarios in probabilistic assessment of various aspects of the power system. The probabilistic model uses a Markov formulation and details of the formation of the transition matrices, model order selection, and a methodology for synthetic generation of data from the model are given. The proposed model is validated by comparing the model generated data with actual measured solar irradiation data. The work presented here is a fundamental study on the probabilistic modeling of solar irradiation using data measured at a single location. The methodology can be extended to data from multiple locations so as to simulate the interaction of several PV generators in a power system.

Chapter 4 presents a simple overhead conductor temperature evaluation model for use

in dynamic line rating systems. First, the original electro-thermal model developed by CIGRE is described followed by details of the simplifications of its various terms from which the simplified model is derived. Numerical and experimental validations of the simple model for both steady-state and transient-state conditions are also described. A couple of application areas of the model are also described.

Chapter 5 discusses the general options available to system operators with respect to the rating of overhead transmission lines. After a definition of the two types of ratings currently in use i.e. the SLR and DLR, a new transient rating – referred to as the dynamic electro-thermal rating (DETR) – is presented. The advantage that the DETR in accommodating fluctuations due to IRE generation is illustrated. Also included in the chapter is a methodology for determining safety factors to be applied to DLRs to ensure a safe operation of overhead transmission lines. Using actual weather data, the nature of the safety factors required to ensure various levels of line overload risks are illustrated.

Chapter 6 presents a new formulation of the optimal power flow (OPF) problem incorporating conductor thermal characteristics (i.e. DLR) while simultaneously considering uncertainty due to IRE generation. The nature of costs due to IRE uncertainty, which are included in the objective function, is detailed. Then, the optimization problem, which includes a maximum conductor temperature constraint – replacing the traditional maximum conductor current constraint, is described. Numerical simulations carried out on a standard test system illustrates the application of the proposed formulation and the effects of various parameters on the obtained optimal solutions are discussed.

Chapter 7 summarizes the main conclusions from the work presented in this dissertation.

1.5 References

[1] J. F. DeCarolis and D. W. Keith, "The economics of large-scale wind power in a carbon constrained world," *Energy Policy*, vol. 34, no. 4, pp. 395 – 410, 2006. doi: https://doi.org/10.1016/j.enpol.2004.06.007.

[2] A. Mills, M. Ahlstrom, M. Brower, A. Ellis, R. George, T. Hoff, B. Kroposki, C. Lenox, N. Miller, J. Stein, and Y. huei Wan, "Understanding variability and uncertainty of photovoltaics for integration with the electric power system," 2009. Available from: https://escholarship.org/uc/item/58z9s527.

[3] B.-M. Hodge, C. B. Martinez-Anido, Q. Wang, E. Chartan, A. Florita, and J. Kiviluoma, "The combined value of wind and solar power forecasting improvements and electricity storage," *Applied Energy*, vol. 214, pp. 1 – 15, 2018. doi: https://doi.org/10.1016/j.apenergy.2017.12.120.

[4] G. Giebel, R. Brownsword, G. Kariniotakis, M. Denhard, and C. Draxl, *The State-Of-The-Art in Short-Term Prediction of Wind Power: A Literature Overview, 2nd edition*. ANEMOS.plus, 2011. doi: https://doi.org/10.11581/DTU:00000017.

[5] P. Denholm, E. Ela, B. Kirby, and M. Milligan, "Role of energy storage with renewable electricity generation." NREL/TP-6A2-47187. Available from: https://www.nrel.gov/docs/fy10osti/47187.pdf.

[6] M. Black and G. Strbac, "Value of bulk energy storage for managing wind power fluctuations," *IEEE Transactions on Energy Conversion*, vol. 22, pp. 197–205, March 2007. doi: https://doi.org/10.1109/TEC.2006.889619.

[7] R. Wang, P. Wang, G. Xiao, and S. Gong, "Power demand and supply management in microgrids with uncertainties of renewable energies," *International Journal of Electrical Power & Energy Systems*, vol. 63, pp. 260 – 269, 2014. doi: https://doi.org/10.1016/j.ijepes.2014.05.067.

[8] M. A. Ortega-Vazquez and D. S. Kirschen, "Estimating the spinning reserve requirements in systems with significant wind power generation penetration," *IEEE Transactions on Power Systems*, vol. 24, pp. 114–124, Feb 2009. doi: https://doi.org/10.1109/TPWRS.2008.2004745.

[9] Živa Bricman Rejc and M. Čepin, "Estimating the additional operating reserve in power systems with installed renewable energy sources," *International Journal of Electrical Power & Energy Systems*, vol. 62, pp. 654 – 664, 2014. doi: https://doi.org/10.1016/j.ijepes.2014.05.019.

[10] F. Liu, Z. Bie, S. Liu, and T. Ding, "Day-ahead optimal dispatch for wind integrated power system considering zonal reserve requirements," *Applied Energy*, vol. 188, pp. 399 – 408, 2017. doi: https://doi.org/10.1016/j.apenergy.2016.11.102.

[11] F. Bouffard and F. D. Galiana, "Stochastic security for operations planning with significant wind power generation," vol. 23, pp. 306–316, May 2008. doi: https://doi.org/10.1109/TPWRS.2008.919318.

[12] L. Roald, M. Vrakopoulou, F. Oldewurtel, and G. Andersson, "Risk-based optimal power flow with probabilistic guarantees," *International Journal of Electrical Power & Energy Systems*, vol. 72, pp. 66 – 74, 2015. doi: https://doi.org/10.1016/j.ijepes.2015.02.012.

[13] T. Summers, J. Warrington, M. Morari, and J. Lygeros, "Stochastic optimal power flow based on conditional value at risk and distributional robustness," *International Journal of Electrical Power & Energy Systems*, vol. 72, pp. 116 – 125, 2015. doi: https://doi.org/10.1016/j.ijepes.2015.02.024.

[14] M. Milligan, B. Frew, E. Zhou, and D. J. Arent, "Advancing system flexibility for high penetration renewable integration." NREL/TP-6A20-64864. Available from: https://www.nrel.gov/docs/fy16osti/64864.pdf.

[15] S. D. Foss and R. A. Maraio, "Dynamic line rating in the operating environment," *IEEE Transactions on Power Delivery*, vol. 5, pp. 1095–1105, Apr 1990. doi: https://doi.org/10.1109/61.53127.

[16] T. Krontiris, A. Wasserrab, and G. Balzer, "Weather-based loading of overhead lines - consideration of conductor's heat capacity," in *2010 Modern Electric Power Systems*, pp. 1–8, Sept 2010. Available from: https://ieeexplore.ieee.org/iel5/5996359/6007154/06007162.pdf.

[17] L. C. Cradden and G. P. Harrison, "Adapting overhead lines to climate change: Are dynamic ratings the answer?," *Energy Policy*, vol. 63, pp. 197 – 206, 2013. doi: https://doi.org/10.1016/j.enpol.2013.08.052.

[18] J. Heckenbergerová, P. Musilek, and K. Filimonenkov, "Quantification of gains and risks of static thermal rating based on typical meteorological year," *International Journal of Electrical Power & Energy Systems*, vol. 44, no. 1, pp. 227 – 235, 2013. doi: https://doi.org/10.1016/j.ijepes.2012.07.005.

[19] M. Simms and L. Meegahapola, "Comparative analysis of dynamic line rating models and feasibility to minimise energy losses in wind rich power networks," *Energy Conversion and Management*, vol. 75, pp. 11 – 20, 2013. doi: https://doi.org/10.1016/j.enconman.2013.06.003.

[20] H. Banakar, N. Alguacil, and F. D. Galiana, "Electrothermal coordination part I: theory and implementation schemes," *IEEE Transactions on Power Systems*, vol. 20, pp. 798–805, May 2005. doi: https://doi.org/10.1109/TPWRS.2005.846196.

[21] N. Alguacil, M. H. Banakar, and F. D. Galiana, "Electrothermal coordination part II: case studies," *IEEE Transactions on Power Systems*, vol. 20, pp. 1738–1745, Nov 2005. doi: https://doi.org/10.1109/TPWRS.2005.857836.

[22] S. Uski, "Estimation method for dynamic line rating potential and economic benefits," *International Journal of Electrical Power & Energy Systems*, vol. 65, pp. 76 – 82, 2015. doi: https://doi.org/10.1016/j.ijepes.2014.09.034.

[23] B. Xu, A. Ulbig, and G. Andersson, "Impacts of dynamic line rating on power dispatch performance and grid integration of renewable energy sources," in *IEEE PES ISGT Europe 2013*, pp. 1–5, Oct 2013. doi: https://doi.org/10.1109/ISGTEurope.2013.6695410.

[24] B. Ngoko, H. Sugihara, and T. Funaki, "Synthetic generation of high temporal resolution solar radiation data using markov models," *Solar Energy*, vol. 103, pp. 160 – 170, 2014. doi: https://doi.org/10.1016/j.solener.2014.02.026.

[25] B. Ngoko, H. Sugihara, and T. Funaki, "Validation of a simplified model for estimating overhead conductor temperatures under dynamic line ratings," *IEEJ Transactions on*

Power and Energy, vol. 138, no. 4, pp. 284–296, 2018. doi: https://doi.org/10.1541/ieejpes.138.284.

[26] B. Ngoko, H. Sugihara, and T. Funaki, "Optimal power flow considering line-conductor temperature limits under high penetration of intermittent renewable energy sources," *International Journal of Electrical Power & Energy Systems*, vol. 101, pp. 255 – 267, 2018. doi: https://doi.org/10.1016/j.ijepes.2018.03.023.

CHAPTER 2

Power system operation with intermittent renewable energy

2.1 Introduction

This chapter describes the state of the art regarding the main themes of this dissertation i.e. power generation by intermittent renewable energy (IRE) sources; transmission system operation in terms of setting the capacity of transmission lines; and optimal system operation in terms of minimizing operational costs. The relationship between IRE generation and transmission line ratings is established by the fact that, the maximum capacity of a transmission line can dictate the usability of a given IRE source especially when the line directly carries power from the IRE source. Therefore, a more flexible approach to the utilization of the transmission lines could lead to increased utilization of IRE sources within the power network. This chapter outlines recent trends in power generation by IRE sources, approaches used by system operators in setting transmission line capacity, and optimal system operation through the solution of the optimal power flow problem.

2.2 Intermittent renewable energy sources

2.2.1 Trends in power generation by IRE sources

Worldwide, the share of electric power supplied by intermittent renewable energy (IRE) sources in power grids is steadily increasing. The REN21 2017 global status report states that *the world now adds more renewable power capacity annually than it adds (net) capacity from all fossil fuels combined* [1]. In 2016, renewables accounted for nearly 62% of net additions to global power generating capacity and represented far higher shares of capacity added in several countries around the world [1]. Figs. 2.1 and 2.2 show the trends in global capacity and new additions in wind power and solar PV respectively over the past decade [1]. The main drivers for the steadily increasing trend depicted in Figs. 2.1 and 2.2 are mitigation of climate change, reduction of air pollution, concerns over energy security, and improving cost-competitiveness of IRE technologies [1].

A look at the situation in Japan, a country that is making large strides towards majority power generation from renewables, the installed capacity of renewable energy (ex-

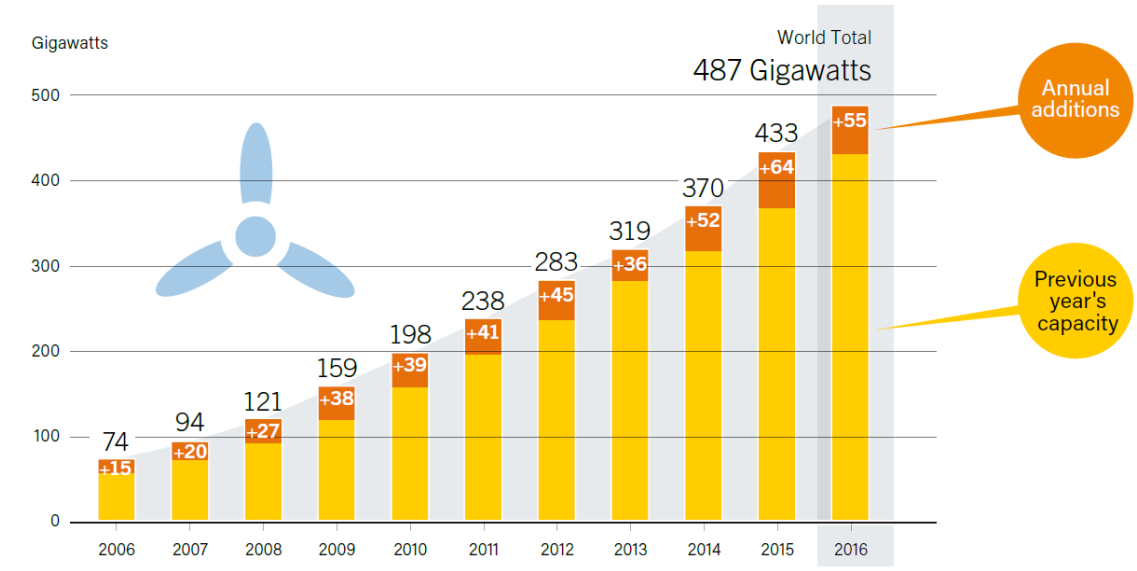

Fig. 2.1: Wind power global capacity and annual additions, 2006-2016 [1].

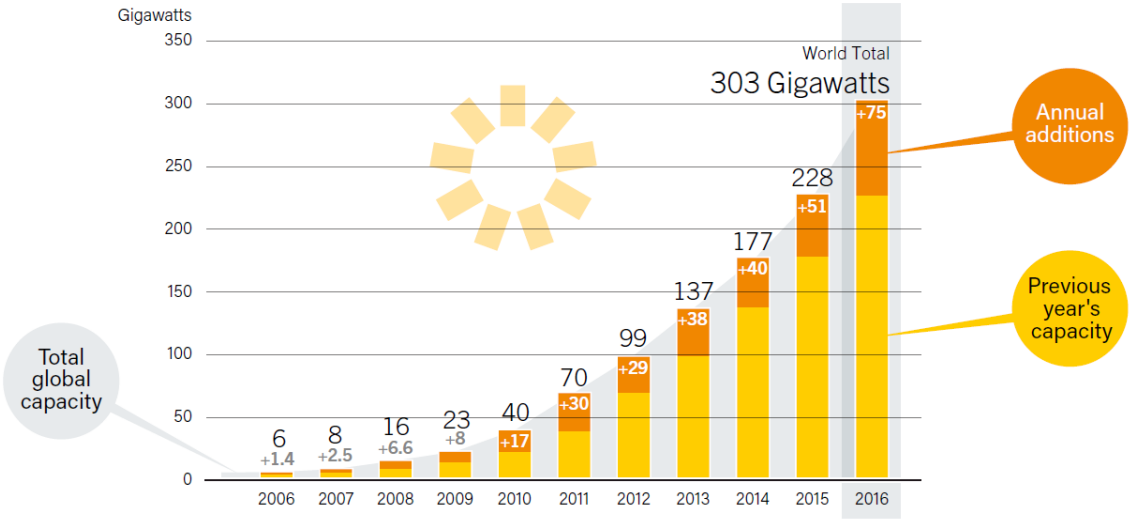

Fig. 2.2: Solar PV global capacity and annual additions, 2006-2016 [1].

cluding large hydro) has increased more than five-fold over the last decade alone to stand at 50 GW in 2016 as shown in Fig. 2.3 [2]. This capacity translates more than 7% of all electric power generation in Japan and the rapid upward trend is expected to continue in the years to come.

2.2.2 Operational challenges with IRE sources

While the advantages of power generation by IRE sources are numerous, their variable and uncertain nature means that a large integration of these sources in electric power networks introduces new operational challenges to power system operators [3, 4]. Fig. 2.4 illustrates the difference between the terms *variability* and *uncertainty* as pertaining to IRE sources. Their effects on system operation are then described as:

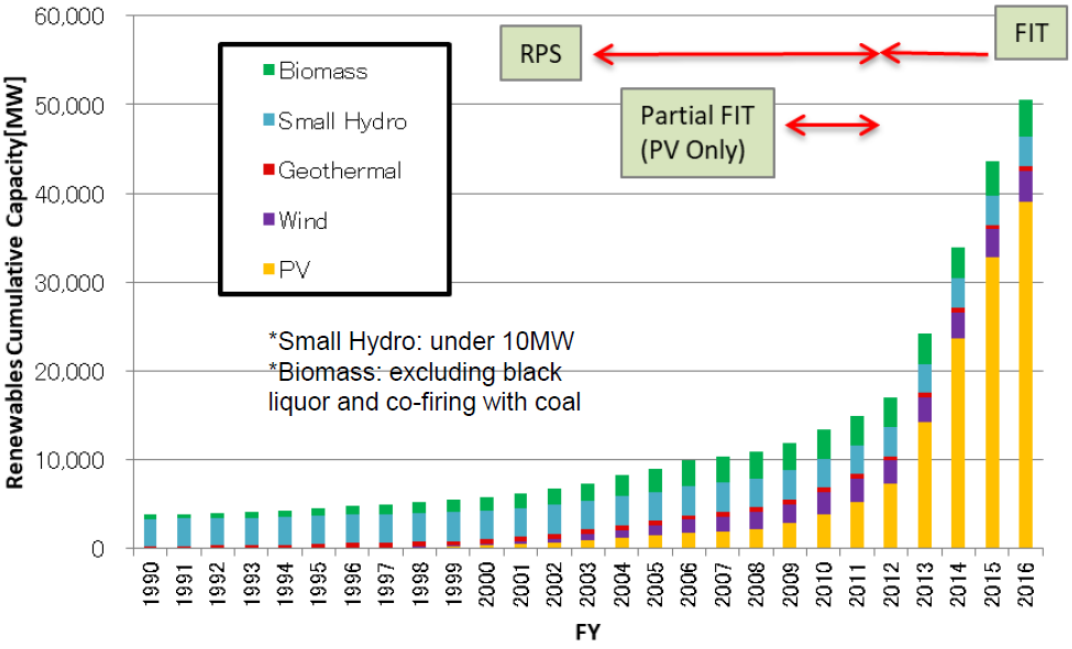

Fig. 2.3: Trends of renewable energy capacity in Japan excluding large hydro [2].

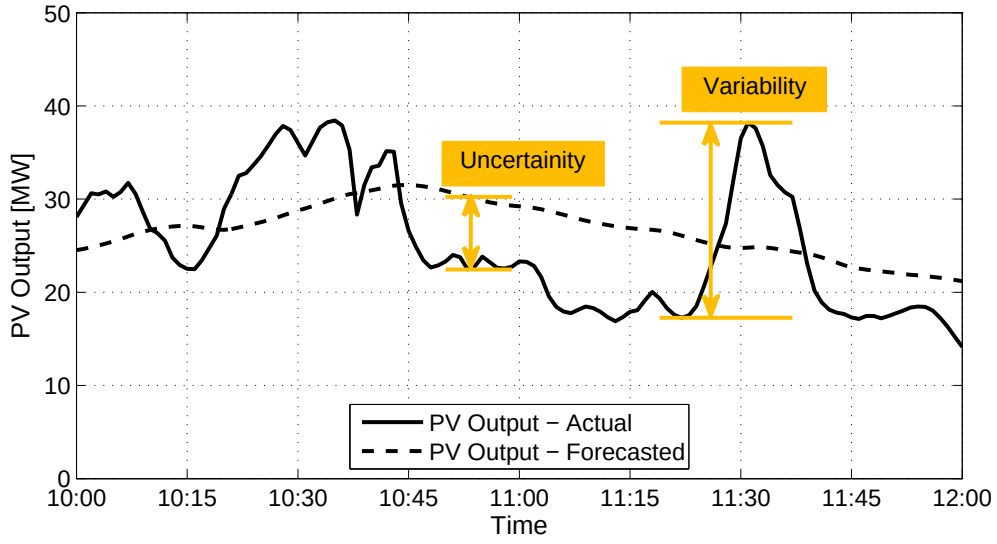

Fig. 2.4: Illustration of IRE source uncertainty and variability.

- *Variability*: The output of IRE sources changes from time-to-time and, unlike traditional sources of power generation, cannot be controlled. The effect is that, in response to the variation of IRE output, other power sources must be varied fast enough to ensure the balance between generation and load. Generally speaking, in terms of system operation, IRE variability affects the reliability and stability of the power system.
- *Uncertainty*: The output of IRE sources cannot be forecasted with 100% accuracy. This means that other fast-responding sources (reserves) must be made available to balance

generation and load in case of a shortage [5]. Such reserves are typically relatively expensive when compared to the cost of conventional generation. Therefore, while IRE sources reduce the net system demand and hence costs of conventional generation, they add costs related to extra reserves necessitated by their uncertain characteristic [6].

2.2.3 Handling increased variability and uncertainty due to IRE generation

Energy management in networks with significant proportions of generation from IRE sources require mechanisms for handling the increased variability and uncertainty due to the intermittency of these sources. Practically, this can be realized in two ways:

- *Stricter reserve settings:* Variability and uncertainty in IRE generation presents the risk of not having enough reserves to cover for shortfalls due to overestimations of the IRE output. The system operator could enforce stricter reserve requirements to ensure generation adequacy in the event of large overestimations of IRE output [7, 8]. Such reserve requirements can be set deterministically for worst-case forecasting conditions or stochastically, considering the statistical distribution of the IRE forecasts [9]. This approach adds extra conservativeness in system operation which translates to relatively more expensive operation.
- *Changes to system operation practices:* An alternative to more conservative approach to system operation is to alter system operation practices e.g. adjusting generation scheduling to shorter periods so as to utilize more accurate IRE forecasts [10]. Such operational changes require extra monitoring of the power system (e.g. in smart grid applications) and typically more actions by the system operator in terms of affecting power utilization. In general, this approach is cheaper at the expense of slightly increased operational risks.

One of the areas which offers potential to handling IRE uncertainty is in the operation of the transmission system. Usually, overly conservative transmission line limits leads to a state termed to as *transmission congestion* where certain generation (including IRE generation) may have to be constrained so as to enforce the loadability limit of particular lines. However, transmission line loadability could be adjusted in real-time depending on the ambient conductor cooling conditions thereby realizing more IRE power utilization.

2.3 Transmission line ratings

The thermal rating of an overhead transmission line is typically a limit on the magnitude of line current aimed at restricting conductor temperature below a manufacturer-specified maximum value [11, 12]. Usually, conductor temperature is restricted in order to limit one or more of the following [13]:

- clearance between conductor and ground,
- clearance to other conductors,
- protection from loss of tensile strength or permanent conductor damage by heat.

Fig. 2.5 illustrates the terms sag and clearance of an overhead transmission line [14].

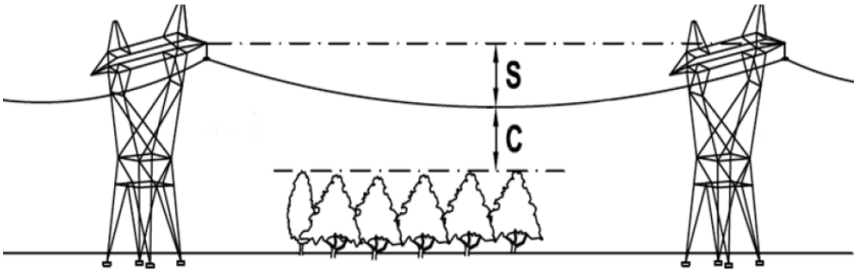

Fig. 2.5: Illustration of sag (S) and clearance (C) of an overhead conductor in a level span [14].

Increased power generation by IRE sources alters the line flows in a power system which in turn increases the probability of violating the set thermal limits of the transmission lines [15]. Technically speaking, the thermal limit of a conductor refers to the maximum temperature that the conductor is allowed to reach as specified by the manufacturer. When this value is exceeded, the conductor experiences excessive sag or suffers a significant loss of strength [14]. However, in practice the temperature value is not used when setting the thermal limit. Rather, an equivalent current value termed *ampacity* is used, which is defined as the conductor current that would result in the maximum allowable conductor temperature for a given set of weather conditions[1] [11, 12]. Two types of thermal ratings can be defined based on the method of calculation: the static line rating (SLR) and dynamic line rating (DLR).

2.3.1 Static line rating

The static line rating (SLR) is defined as the conductor current that would result in the conductor temperature reaching the maximum allowed temperature at steady-state for *worst-case* weather conditions [11, 12, 16]. The SLR is therefore a very conservative setting. The use of worst-case weather conditions in the calculation of the SLR ensures that the probability of conductor temperatures reaching the maximum allowed values are very low even if the conductor continuously carries the SLR current. This, coupled with typical N-1 reliability criteria, means that overhead conductors are typically used well below their actual thermal ratings. However, although the SLR is conservative, it is the most reliable rating system for present power system operators, given the long experience in many countries.

2.3.2 Dynamic line rating

The dynamic line rating (DLR) is defined as the conductor current that would result in the conductor temperature reaching the maximum allowed temperature at steady-state for the prevailing *real-time* weather conditions [12, 17, 18]. DLR can be achieved through

[1]The ampacity value can be easily converted to an active power or apparent power value depending on the voltage level to give a maximum power limit.

direct or indirect monitoring of conductor temperature [13, 19]. Direct monitoring could be achieved through the direct measurement of the temperature, sag [20, 21], or tension [22], while indirect monitoring requires measurements of the conductor current and weather parameters along the line followed by using mathematical models that relate the conductor temperature to the current and weather parameters to estimate the conductor temperature [19]. Fig. 2.6 shows typical overhead transmission line monitoring for DLRs [23].

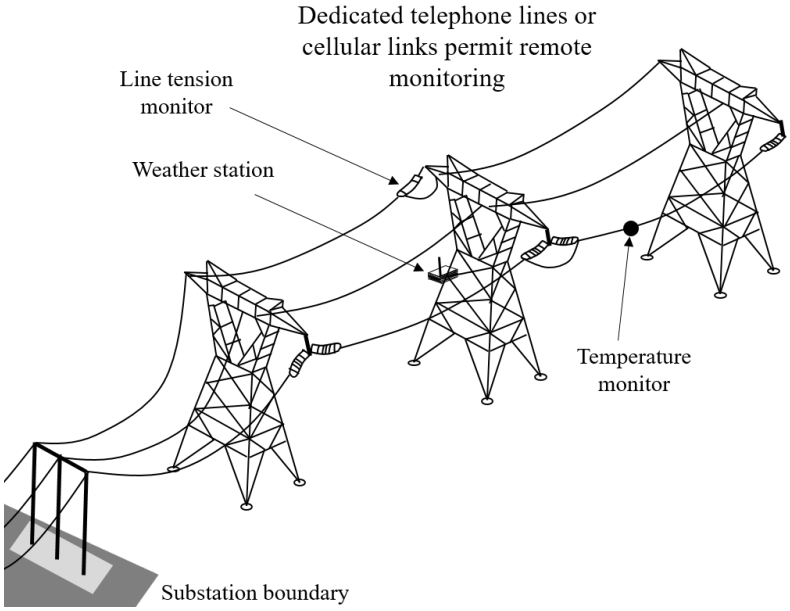

Fig. 2.6: Monitoring of overhead lines for real-time dynamic line ratings [23].

With DLR, the line rating is re-calculated after pre-set time durations, say every 30 minutes, varying the values of the weather parameters along the line as the ambient weather changes. The use of real-time weather conditions relaxes the conservativeness of the thermal constraints set by the SLR since prevailing weather conditions are usually considerably better at cooling the conductor than the worst-case conditions used to calculate the SLR. DLRs therefore usually result in higher transmission line loadability though there is a requirement of constant monitoring of weather conditions and a slight increase in the risk of violating the thermal constraints of the transmission line. DLRs could be particularly useful as current flowing in transmission lines become more variable and uncertain due to increased power generation from IRE sources [24, 25].

2.4 Optimal power system operation

Electric power system operators are responsible for ensuring reliability and security of electric power supply to consumers. However, this has to be done at a reasonable cost and consequently, system operators usually seek the most economical way of meeting the demand at all times while keeping high levels of reliability. This is done through a combination of load forecasting and economic scheduling of available generation based on the forecasted demand. One of the most important tools available to the system operator

in the optimal scheduling of system resources is the optimal power flow (OPF) model.

2.4.1 The optimal power flow problem

Generally, the optimal power flow problem seeks to determine the optimal mix[2] of power generation levels from the various sources available to the system operator. Here, an optimal mix would be the generation schedule that minimizes a given objective function under various technical and physical constraints. The OPF problem is then presented as a mathematical optimization problem with typical objectives being cost minimization [26, 27] and active or reactive power loss minimization [28, 29, 30].

The problem decision variables include the active power outputs of various generators and the voltage set-points of those units with voltage regulation capabilities. System state variables would then be the reactive power outputs of the generators, voltage magnitudes at non-voltage controlled buses, voltage angles at non-reference buses, and current (or power) flow in the various system branches [31]. The OPF problem involves both equality and inequality constraints. Equality constraints are usually the power flow equations – mathematical equations describing the physical flow of both active and reactive power within the transmission network. On the other hand, inequality constraints are usually physical limits on various system variables including bus voltages, real and reactive power generation and the current (or power) flowing through the various branches of the power network. Reference [31] gives a thorough review of the state of the art in the various formulations and solution algorithms of the OPF problem.

2.4.2 Effect of line flow limits on the OPF solution

One of the most important constraints in the OPF model is the branch flow limit i.e. the amount of current (power) allowed to flow in a given branch[3]. The restriction of transmission paths due to the branch flow constraint manifests in the OPF solution as active branch flow constraints and leads to a situation referred to in industry as transmission congestion [32]. The effects of transmission congestion include increased operational costs, unbalanced electricity supply costs and even curtailment of IRE generation. The introduction of large amounts of IRE generation in power systems could further necessitate more stringent branch flow constraints as the uncertainty in line flows increases. However, as explained in Section 2.3, DLR of transmission lines based on real-time monitoring could be used to allow increased transmission line loadability. The result could translate to a more economical system operation i.e. better solution of the OPF problem or even a reduction in necessary IRE power curtailment. However, in contrast to the mentioned benefits, DLR is usually accompanied by an increase in the risk of violating the thermal constraints. The line rating risk-benefit tradeoff is illustrated in Fig. 2.7.

[2] An electricity generation mix refers to the percentage of different energy sources (fossil fuels, nuclear, hydro and other renewable energies) used to generate electricity at a given point in time.

[3] A branch is a connection between two system buses and could be a transmission line, transformer, or even a power converter.

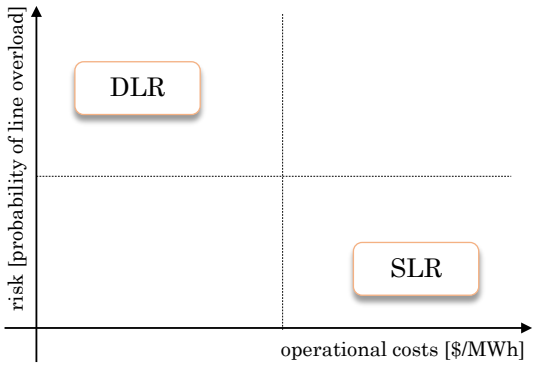

Fig. 2.7: Illustration of risk-benefit trade-off with transmission line ratings.

2.5 References

[1] REN21, "Renewables 2017 Global Status Report," *Paris: REN21 Secretariat*, 2017. Available from: http://www.ren21.net/gsr-2017/.

[2] ISEP, "Renewables 2016 Japan Status Report," *Institute for Sustainable Energy Policies*, 2016. Available from: https://www.isep.or.jp/en/jsr2016.

[3] W. Wei, F. Liu, and S. Mei, "Real-time dispatchability of bulk power systems with volatile renewable generations," *IEEE Transactions on Sustainable Energy*, vol. 6, pp. 738–747, July 2015. doi: https://doi.org/10.1109/TSTE.2015.2413903.

[4] E. Lannoye, D. Flynn, and M. O'Malley, "Transmission, variable generation, and power system flexibility," *IEEE Transactions on Power Systems*, vol. 30, pp. 57–66, Jan 2015. doi: https://doi.org/10.1109/TPWRS.2014.2321793.

[5] Živa Bricman Rejc and M. Čepin, "Estimating the additional operating reserve in power systems with installed renewable energy sources," *International Journal of Electrical Power & Energy Systems*, vol. 62, pp. 654 – 664, 2014. doi: https://doi.org/10.1016/j.ijepes.2014.05.019.

[6] R. Wang, P. Wang, G. Xiao, and S. Gong, "Power demand and supply management in microgrids with uncertainties of renewable energies," *International Journal of Electrical Power & Energy Systems*, vol. 63, pp. 260 – 269, 2014. doi: https://doi.org/10.1016/j.ijepes.2014.05.067.

[7] R. Doherty and M. O'Malley, "A new approach to quantify reserve demand in systems with significant installed wind capacity," *IEEE Transactions on Power Systems*, vol. 20, pp. 587–595, May 2005. doi: https://doi.org/10.1109/TPWRS.2005.846206.

[8] F. Liu, Z. Bie, S. Liu, and T. Ding, "Day-ahead optimal dispatch for wind integrated

power system considering zonal reserve requirements," *Applied Energy*, vol. 188, pp. 399 – 408, 2017. doi: https://doi.org/10.1016/j.apenergy.2016.11.102.

[9] J. Wang, M. Shahidehpour, and Z. Li, "Security-constrained unit commitment with volatile wind power generation," *IEEE Transactions on Power Systems*, vol. 23, pp. 1319–1327, Aug 2008. doi: https://doi.org/10.1109/TPWRS.2008.926719.

[10] J. Cochran, M. Miller, O. Zinaman, M. Milligan, D. Arent, B. Palmintier, M. O'Malley, S. Mueller, E. Lannoye, A. Tuohy, B. Kujala, M. Sommer, H. Holttinen, J. Kiviluoma, and S. K. Soonee, "Flexibility in 21st century power systems," May 2014. NREL, Colorado, United States, May 2014, doi: https://doi.org/10.2172/1130630.

[11] D. A. Douglass, "Weather-dependent versus static thermal line ratings [power overhead lines]," *IEEE Transactions on Power Delivery*, vol. 3, pp. 742–753, Apr 1988. doi: https://doi.org/10.1109/61.4313.

[12] S. D. Foss and R. A. Maraio, "Dynamic line rating in the operating environment," *IEEE Transactions on Power Delivery*, vol. 5, pp. 1095–1105, Apr 1990. doi: https://doi.org/10.1109/61.53127.

[13] CIGRE Working Group B2.36, "Guide for application of direct real-time monitoring systems," June 2012. CIGRE Technical Brochure.

[14] A. Michiorri, H.-M. Nguyen, S. Alessandrini, J. B. Bremnes, S. Dierer, E. Ferrero, B.-E. Nygaard, P. Pinson, N. Thomaidis, and S. Uski, "Forecasting for dynamic line rating," *Renewable and Sustainable Energy Reviews*, vol. 52, pp. 1713 – 1730, 2015. doi: https://doi.org/10.1016/j.rser.2015.07.134.

[15] M. Schlapfer and P. Mancarella, "Probabilistic modeling and simulation of transmission line temperatures under fluctuating power flows," *IEEE Transactions on Power Delivery*, vol. 26, no. 4, pp. 2235–2243, 2011. doi: https://doi.org/10.1109/TPWRD.2011.2145394.

[16] "Current capacity of overhead power transmission lines (in Japanese)," *Technical Report of the Institute of Electrical Engineers of Japan*, Dec 1997.

[17] T. Krontiris, A. Wasserrab, and G. Balzer, "Weather-based loading of overhead lines - consideration of conductor's heat capacity," in *2010 Modern Electric Power Systems*, pp. 1–8, Sept 2010. Available from: https://ieeexplore.ieee.org/iel5/5996359/6007154/06007162.pdf.

[18] S. Talpur, C. J. Wallnerström, P. Hilber, and S. N. Saqib, "Implementation of dynamic line rating technique in a 130 kv regional network," in *Multi-Topic Conference (INMIC), 2014 IEEE 17th International*, pp. 477–482, Dec 2014. doi: https://doi.org/10.1109/INMIC.2014.7097387.

[19] D. J. Morrow, J. Fu, and S. M. Abdelkader, "Experimentally validated partial least squares model for dynamic line rating," *IET Renewable Power Generation*, vol. 8, no. 3, pp. 260–268, 2014. doi: https://doi.org/10.1049/iet-rpg.2013.0097.

[20] K. Adomah, Y. Mizuno, and K. Naito, "Probabilistic assessment of the sag in an overhead transmission line," *IEEJ Transactions on Power and Energy*, vol. 120, no. 10, pp. 1298–1303, 2000. doi: https://doi.org/10.1541/ieejpes1990.120.10_1298.

[21] S. M. Mahajan and U. M. Singareddy, "A real-time conductor sag measurement system using a differential GPS," *Power Delivery, IEEE Transactions on*, vol. 27, no. 2, pp. 475–480, 2012. doi: https://doi.org/10.1109/TPWRD.2011.2181963.

[22] I. Albizu, E. Fernandez, P. Eguia, E. Torres, and A. J. Mazón, "Tension and ampacity monitoring system for overhead lines," *Power Delivery, IEEE Transactions on*, vol. 28, no. 1, pp. 3–10, 2013. doi: https://doi.org/10.1109/TPWRD.2012.2213308.

[23] D. A. Douglass, D. C. Lawry, A. A. Edris, and E. C. Bascom, "Dynamic thermal ratings realize circuit load limits," *IEEE Computer Applications in Power*, vol. 13, pp. 38–44, Jan 2000. doi: https://doi.org/10.1109/67.814665.

[24] B. Xu, A. Ulbig, and G. Andersson, "Impacts of dynamic line rating on power dispatch performance and grid integration of renewable energy sources," in *IEEE PES ISGT Europe 2013*, pp. 1–5, Oct 2013. doi: https://doi.org/10.1109/ISGTEurope.2013.6695410.

[25] J. Heckenbergerová and J. Hošek, "Dynamic thermal rating of power transmission lines related to wind energy integration," in *2012 11th International Conference on Environment and Electrical Engineering*, pp. 798–801, May 2012. doi: https://doi.org/10.1109/EEEIC.2012.6221484.

[26] R. A. Jabr, "Adjustable robust OPF with renewable energy sources," *IEEE Transactions on Power Systems*, vol. 28, pp. 4742–4751, Nov 2013. doi: https://doi.org/10.1109/TPWRS.2013.2275013.

[27] B. Ngoko, H. Sugihara, and T. Funaki, "Optimal power flow considering line-conductor temperature limits under high penetration of intermittent renewable energy sources," *International Journal of Electrical Power & Energy Systems*, vol. 101, pp. 255 – 267, 2018. doi: https://doi.org/10.1016/j.ijepes.2018.03.023.

[28] S. S. Sharif, J. H. Taylor, and E. F. Hill, "On-line optimal reactive power flow by energy loss minimization," in *Proceedings of 35th IEEE Conference on Decision and Control*, vol. 4, pp. 3851–3856 vol.4, Dec 1996. doi: https://doi.org/10.1109/CDC.1996.577262.

[29] M. Ghasemi, S. Ghavidel, M. M. Ghanbarian, and A. Habibi, "A new hybrid algorithm for optimal reactive power dispatch problem with discrete and continu-

ous control variables," *Applied Soft Computing*, vol. 22, pp. 126 – 140, 2014. doi: https://doi.org/10.1016/j.asoc.2014.05.006.

[30] M. Mehdinejad, B. Mohammadi-Ivatloo, R. Dadashzadeh-Bonab, and K. Zare, "Solution of optimal reactive power dispatch of power systems using hybrid particle swarm optimization and imperialist competitive algorithms," *International Journal of Electrical Power & Energy Systems*, vol. 83, pp. 104 – 116, 2016. doi: https://doi.org/10.1016/j.ijepes.2016.03.039.

[31] F. Capitanescu, "Critical review of recent advances and further developments needed in ac optimal power flow," *Electric Power Systems Research*, vol. 136, pp. 57 – 68, 2016. doi: https://doi.org/10.1016/j.epsr.2016.02.008.

[32] A. Singla, K. Singh, and V. K. Yadav, "Transmission congestion management in deregulated environment: A bibliographical survey," in *International Conference on Recent Advances and Innovations in Engineering (ICRAIE-2014)*, pp. 1–10, May 2014. doi: https://doi.org/10.1109/ICRAIE.2014.6909268.

CHAPTER 3

Probabilistic modeling of solar photovoltaic (PV) power generation

3.1 Introduction

This chapter presents a probabilistic model for high temporal resolution (1-minute) solar radiation that can be applied in power system simulations. The model is used to "synthetically" generate scenarios of solar PV power (from solar irradiation data) to simulate fluctuations in power generated by a solar PV source. As introduced in Chapter 2, IRE sources and DLRs introduce the concept of risk in system operation e.g. the risk of violating the thermal constraint of a transmission line is defined as the probability of the conductor temperature exceeding the maximum allowable limit. A risk based operation of the power system necessitates a probabilistic assessment of the occurrence of various eventualities. And, such probabilistic assessments require probabilistic models of the underlying stochastic processes. In fact, one of the proposed changes in power system operations proposed for handling increased IRE generation is to move from the traditional deterministic rules in system operation to probabilistic rules [1, 2].

Probabilistic approaches rely on stochastic models of the various components of the system to simulate the overall system. The correctness of the overall study therefore heavily depends on how well these stochastic models represent the various components. Methodologies used to reproduce the real world data should use models that as best as possible represent the phenomena they model. The probabilistic model presented in this chapter correctly captures very short-term fluctuations in solar PV power (up to 1-minute temporal resolution).

3.1.1 Literature review

A number of probabilistic models for global solar radiation which can be used to simulate solar PV generation have been proposed in literature. However, these studies have concentrated on models for daily [3, 4, 5] and hourly solar radiation values [6, 7, 8]. Models for higher temporal resolution are rare not only because such recorded data are themselves rare but also because the scope of most studies involving solar radiation concentrate on concepts such as the total energy potential of particular locations and hence do not need

high temporal resolution data. However, real-time operation of power systems requires models for higher temporal resolutions – in the order of minutes.

The proposed solar PV models use either Autoregressive Moving Average (ARMA) or Markov Transition Matrix (MTM) methods to model the *clearness index* i.e. the ratio of the solar radiation recorded on the earth's surface to the extraterrestrial solar radiation. However, the statistical properties of the daily or hourly clearness index data are significantly different from the statistical properties of 1-minute or even 5-minute clearness index data [9, 10]. Both [9] and [10] report bimodal probability density functions of 1-minute and 5-minute clearness index data; a feature significantly different from the unimodal nature of the probability density functions of daily or even hourly clearness index data. These differences imply that models for various temporal resolutions would be different.

While most of the studies on probabilistic modeling and synthetic generation of solar radiation data have been focused on daily and hourly data, there have been attempts at modeling higher temporal resolution solar radiation data [11, 12]. Reference [11] models the probability distribution and lag-1 autocorrelation of short term irradiance data (1- to 10-minute) and use these in a first order autoregressive model for the synthetic generation of short term data. While the models achieve satisfactory results in reproducing the modeled data, they utilize complex approximate equations of the probability density functions and the errors introduced by these approximations are not quantified. The model also ignores the dependence of clearness index on solar elevation angle as reported in [13]. Also, by only considering the lag-1 autocorrelation, the model assumes little or no correlation in the time series data to data at lags greater than 1.

Reference [12] uses a single first order Markov transition matrix to synthetically generate 1-min global solar radiation data. The model is a single part of a large integrated model which also includes a household occupancy and power demand model. Though it is quite simple, the use of a single transition matrix ignores the fact that different days have different statistical properties. For example, it is expected that a transition matrix modeling a clear day will be significantly different from one modeling a cloudy day.

The probabilistic model presented in this chapter utilizes a normalized form of the clearness index which eliminates trends existing in measured data. Also, because different days have different statistical characteristics, the days in the data set are first grouped based on the daily clearness index value and parameters for the Markov models are then extracted for each group. The autocorrelation characteristics of measured data is used to arrive at the choice of a second order Markov model. The proposed model is validated by comparing the statistical characteristics of synthetically generated data to those of the observed data.

3.1.2 Probabilistic modeling fundamentals

A stochastic variable is subject to variations of randomness in the process generating it [14]. Unlike deterministic variables, stochastic variables do not take a single value but rather take one of a given set of values each with an associated probability. Generally, the

modeling of a stochastic variable X_t involves the modeling of its expected value $\mathbb{E}[X_t]$ and its random component α_t. There are numerous methods for modeling stochastic variables which mainly differ on the way they model $\mathbb{E}[X_t]$ and α_t. Two of the more popular methods are the Auto-Regressive Moving Average (ARMA) [14] and Markov Transition Matrix (MTM) models [15, 16]. As a simple example, a first-order autoregressive (AR(1)) model is of the form:

$$X_t = \phi X_{t-1} + \alpha_t. \tag{3.1}$$

where ϕ is the lag 1 autocorrelation.

This means that, given X_{t-1} (the value of the random variable at time $t-1$), the expected value at time t will be $\mathbb{E}[X_t] = \phi X_{t-1}$. The random component to be added to $\mathbb{E}[X_t]$ will be defined by the nature of the probability distribution of α_t. In most cases, it is assumed that α_t is normally distributed with mean 0 and variance σ^2.

In ARMA models, the nature of the random component is independent of the value of the stochastic variable X_t. Markov models, on the other hand allow for the modeling of stochastic variables in which the random component is dependent on the value of X_t. For example, during periods of scattered clouds in the sky, the observed solar radiation data exhibits large fluctuations which are not observed during clear or even heavily cloudy periods. Hence, the nature of the random component in the probabilistic model has a dependency on the level of the stochastic variable. Because of this characteristic of solar radiation data, the stochastic variable in this thesis is modeled as a Markov process. A more detailed description of Markov models follows in Section 3.1.3.

3.1.3 A general formulation of Markov models

Markov models provide a simple yet powerful way of modeling the dependence between adjacent observations in a given time series [16]. They have consequently been used extensively in the modeling of various stochastic variables including the modeling of wind time series [17], rainfall patterns [18] and solar radiation data [3, 19].

A process is said to exhibit the Markov property if, given its present state, the future is conditionally independent of the past and Markov models are mathematical representations of such stochastic processes [16]. A Markov process $(X_t, t = 0, 1, 2, \dots)$ with a set of m allowed states $(1, 2, \dots, m)$ is said to be in state j at time t if $X_t = j$. In a first order Markov process, given that the process is in state i at time $t-1$, the probability that it will be in state j at time t is given by a fixed probability P_{ij} written mathematically as:

$$\begin{aligned} P_{ij} &= P\left(X_t = j | X_{t-1} = i, X_{t-2} = i_{t-2}, \dots X_0 = i_0\right) \\ &= P\left(X_t = j | X_{t-1} = i\right). \end{aligned} \tag{3.2}$$

P_{ij}, known as the transition probability from state i to j, is independent of the states of the process at times $t-2, t-3, \dots$. Equation (3.2) describes a first order Markov process - the conditional distribution of X_t given $X_0, X_1, \dots X_{t-1}$ depends only on X_{t-1}.

In an n^{th} order Markov model, the probability that the process will be in a particular state at time t depends not only on its state at time $t-1$ but also on the states at times

$t-2, t-3, \ldots, t-n$. For example, in a second order Markov process, the probability that the process will be in state k at time t given that it was in state j at time $t-1$ and in state i at time $t-2$ is given by:

$$P_{ijk} = P\left(X_t = k | X_{t-1} = j, X_{t-2} = i\right). \tag{3.3}$$

The transition matrix $\mathbf{P^n}$ holds the transition probabilities for the n^{th} order Markov process. The first order transition matrix would typically be represented as:

$$\mathbf{P^1} = \begin{bmatrix} P_{11} & P_{12} & \ldots & P_{1m} \\ P_{21} & P_{22} & \ldots & P_{2m} \\ \vdots & \vdots & \ddots & \vdots \\ P_{m1} & P_{m2} & \ldots & P_{mm} \end{bmatrix}. \tag{3.4}$$

While this is an $m \times m$ square matrix, the second order transition matrix:

$$\mathbf{P^2} = \begin{bmatrix} P_{111} & P_{112} & \ldots & P_{11m} \\ P_{121} & P_{122} & \ldots & P_{12m} \\ \vdots & \vdots & \ddots & \vdots \\ P_{211} & P_{212} & \ldots & P_{21m} \\ P_{221} & P_{222} & \ldots & P_{22m} \\ \vdots & \vdots & \ddots & \vdots \\ P_{mm1} & P_{mm2} & \ldots & P_{mmm} \end{bmatrix} \tag{3.5}$$

is an $m^2 \times m$ matrix. Similarly, an n^{th} order Markov model will have an $m^n \times m$ transition matrix.

From a given set of observations, the transition probability from state i to j can be easily estimated by counting the number of times the states sequence ij is observed and diving by the total number of times state i is observed. For the second order process, the probability of moving to state k immediately after the observations of states i and j can be estimated by counting the number of times the sequence ijk is observed and diving by the total number of times the sequence ij is observed.

With sufficient data, solar radiation data can be discretized into radiation states from which Markov transition matrices can be constructed forming Markov models. These models can then be used to synthetically generate sets of solar radiation data for power system simulations.

3.2 Solar radiation modeling with Markov models

3.2.1 Data used

Two sets of three-year solar radiation data taken at 1-minute intervals from two locations in Japan were used in the development and validation of the probabilistic model presented in this chapter. The coordinates and data collection periods for the two locations are given in Table 3.1.

The 1-minute clearness index k_t is defined as the ratio of the global solar irradiation

Table 3.1: Solar radiation database

Location	Latitude	Longitude	Period
Shinjuku, Tokyo	35.68° N	139.67° E	Jan 2004 - Dec 2006
Suita, Osaka	34.82° N	135.52° E	Sep 2007 - Aug 2010

that reaches the earth's surface H, to the extraterrestrial solar radiation H_e during a 1-minute period. H and H_e are both given in $\mathrm{W/m^2}$. H_e can be calculated using the solar geometry equations given in Appendix C. Using a model of the stochastic variable k_t, values of H can be obtained from:

$$H = k_t H_e \qquad \left[\mathrm{W/m^2}\right]. \tag{3.6}$$

Fig. 3.1 shows a typical plot of measured 1-minute global solar radiation data and calculated extraterrestrial solar radiation for a single day. Fig. 3.2 shows the corresponding plot of k_t. As seen from Fig. 3.2, the plot of k_t exhibits a noticeable trend with durations near noon having higher values of k_t than durations near sunrise and sunset. This suggests the need for de-trending the data before attempting to fit a stochastic model.

3.2.2 Trend removal

Reference [13] highlights the dependence of k_t on the zenith angle and removes this dependence by transforming k_t to a new variable, the normalized clearness index k_t', through:

$$k_t' = \frac{k_t}{1.031 \exp\left[\frac{-1.4}{0.9+9.4/a}\right] + 0.1}. \tag{3.7}$$

The denominator in (3.7) is the Kasten pyheliometric formula [20] whereby a is the relative air mass given approximately as:

$$a = \frac{1}{\cos z} \tag{3.8}$$

where z is the zenith angle (see Appendix C). Fig. 3.3 shows the plot of k_t' corresponding to the plot of k_t given in Fig. 3.2. It shows the de-trending of the data achieved by the transformation of (3.7).

From a stochastic model of k_t', k_t can be obtained from (3.7) with k_t as the subject of the formula. H can consequently be obtained using (3.6).

3.2.3 Model construction

The first consideration in the construction of a stochastic model for global solar radiation is that different days have different statistical properties stemming from different weather conditions. For example, the probability of getting a k_t' value of 0.7 is much higher in a clear day than in a cloudy day. The model construction is therefore started by grouping the days in the data set based on the observed daily clearness index K_d values. Fifteen groups are constructed using K_d bins of width 0.05 i.e. the first group holds all days with K_d values between 0 and 0.05, the second group holds all days with K_d values between 0.05 and 0.10 and so on. The last group has K_d values between 0.70 and 0.75. The

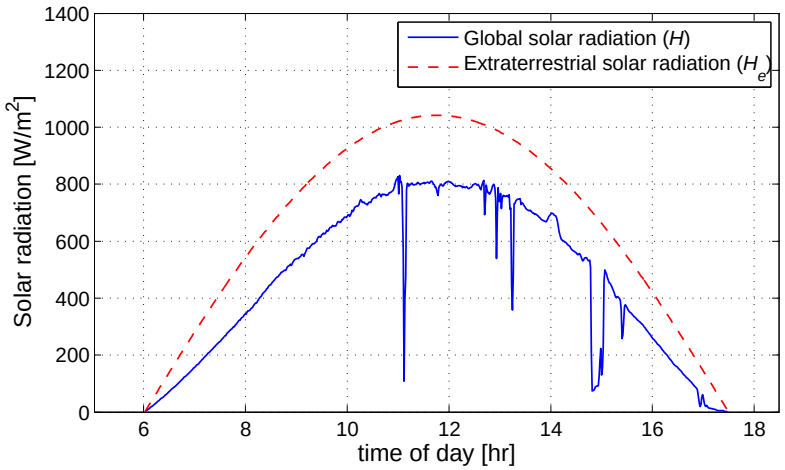

Fig. 3.1: Measured 1-min global and calculated extraterrestrial solar radiation.

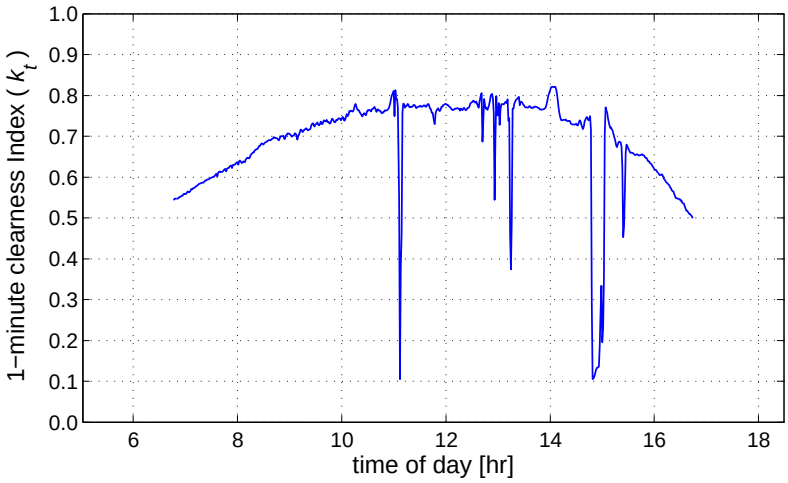

Fig. 3.2: Calculated 1-min clearness index (k_t) from Fig. 3.1.

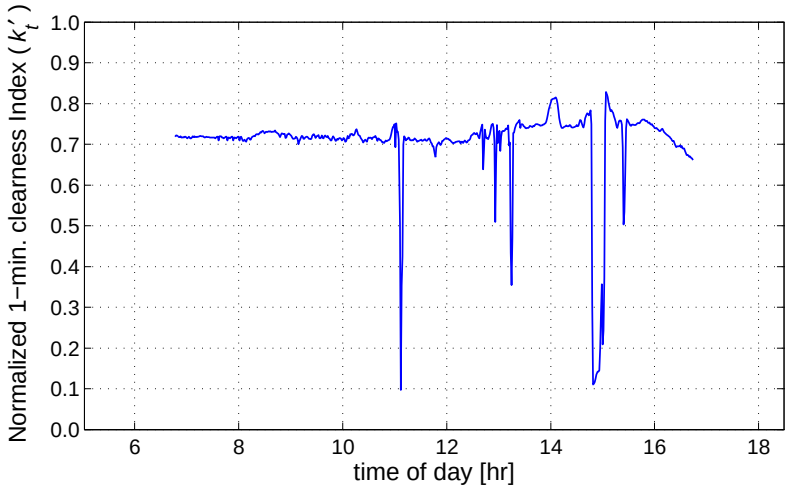

Fig. 3.3: Normalized 1-min clearness index (k'_t) from Fig. 3.2.

highest observed value of K_d in the data set was 0.742. The bin width of 0.05 was chosen empirically as a compromise between having days with as similar statistical characteristics as possible in each group and having enough data in each bin.[1] Markov transition matrices (MTMs) are then constructed for each group as follows.

The first step in the construction of the MTMs is the conversion of observed k_t' values into states. 100 states of k_t' are defined based on the k_t' value with the first state holding k_t' values between 0 and 0.01; state 2 holds k_t' values between 0.01 and 0.02, and so on. The k_t' sequence is therefore converted into a sequence of states X_t with $X_t = 1$ if $0 < k_t' \leq 0.01$; $X_t = 2$ if $0.01 < k_t' \leq 0.02$; and so on. 100 discretization states were empirically chosen so as to as best as possible represent the distribution functions in the transition matrices.[2]

If, in the data set, f_{ij} is the number of times state j is observed immediately after the observation of state i, and if f_i^* is the total number of times state i is observed, then the probability of observing state j one time step after the observation of state i is given by:

$$P_{ij} = f_{ij}/f_i^*. \tag{3.9}$$

The i^{th} row of the first order MTM is therefore simply constructed by dividing the frequency distribution of states observed immediately following the observation of state i by the total number of times state i is observed. In this way, first order MTMs can be constructed for each of the 15 groups of days. Higher order MTMs are constructed in similar ways to the first order MTMs only that each row of the n^{th} order MTMs describes the probability of observations depending on the n previous observations. With 100 possible states, the first order MTMs are 100×100 matrices while the n^{th} order MTMs are $100^n \times 100$ matrices.

Tables 3.2 and 3.3 show some of the entries in the first and second order MTMs for days with K_d values between 0.00 and 0.05. As seen from these tables, the generated MTMs are typically very sparse matrices with most non zero values lying very near the diagonal of the matrices. This shows a strong correlation between successive observations. Also, in some cases, some rows of the MTMs add up to zero. For example, for days with K_d values between 0.00 and 0.05, no values of k_t' between 0.99 and 1.00 are observed. Hence, the last rows of the MTMs shown in Tables 3.2 and 3.3 are made up entirely of zeros. The test data was used to empirically construct transition matrices for each of the fifteen groups of days.

The order of a Markov model determines how many previous observations are used in generating the next state in a Markov process. The order of the model therefore plays a crucial role in capturing the serial correlation characteristics of modeled data. The next section therefore considers the selection of the order of the Markov model.

[1] Having bins of smaller width results in increased similarity in the statistical characteristics of days in each bin. However, fewer days (less data) will be contained in each bin hence the extracted parameters will be less accurate. Various bin widths were considered and the bin width of 0.05 was found to be most suitable.

[2] Discretization essentially linearizes the probability density function (pdf) between certain points. For example, a k_t' value between 0.00 and 0.01 will be obtained by assuming that the pdf is linear between the points $k_t' = 0.00$ and $k_t' = 0.01$. Hence, the more the number of discretization states, the better the representation of the pdf. However, it also results in significantly larger transition matrices.

Table 3.2: First order MTM for days with K_d values between 0.00 and 0.05.

	1	2	3	4	5	6	7	⋯	100
1	0.875	0.125	0.000	0.000	0.000	0.000	0.000	⋯	0.000
2	0.018	0.856	0.126	0.000	0.000	0.000	0.000	⋯	0.000
3	0.000	0.047	0.849	0.104	0.000	0.000	0.000	⋯	0.000
4	0.000	0.001	0.105	0.812	0.079	0.003	0.000	⋯	0.000
5	0.000	0.000	0.000	0.222	0.688	0.086	0.004	⋯	0.000
6	0.000	0.000	0.000	0.010	0.238	0.619	0.124	⋯	0.000
7	0.000	0.000	0.000	0.000	0.000	0.216	0.730	⋯	0.000
8	0.000	0.000	0.000	0.000	0.000	0.006	0.158	⋯	0.000
⋮	⋮	⋮	⋮	⋮	⋮	⋮	⋮		⋮
100	0.000	0.000	0.000	0.000	0.000	0.000	0.000	⋯	0.000

Table 3.3: Second order MTM for days with K_d values between 0.00 and 0.05.

		1	2	3	4	5	6	7	⋯	100
1	1	0.830	0.170	0.000	0.000	0.000	0.000	0.000	⋯	0.000
1	2	0.167	0.417	0.167	0.167	0.083	0.000	0.000	⋯	0.000
1	3	0.000	0.000	0.000	0.000	0.000	0.000	0.000	⋯	0.000
⋮	⋮	⋮	⋮	⋮	⋮	⋮	⋮	⋮		⋮
2	1	0.818	0.182	0.000	0.000	0.000	0.000	0.000	⋯	0.000
2	2	0.017	0.827	0.157	0.000	0.000	0.000	0.000	⋯	0.000
2	3	0.000	0.072	0.783	0.133	0.012	0.000	0.000	⋯	0.000
⋮	⋮	⋮	⋮	⋮	⋮	⋮	⋮	⋮		⋮
3	1	0.000	0.000	0.000	0.000	0.000	0.000	0.000	⋯	0.000
3	2	0.036	0.786	0.179	0.000	0.000	0.000	0.000	⋯	0.000
3	3	0.000	0.064	0.817	0.120	0.000	0.000	0.000	⋯	0.000
⋮	⋮	⋮	⋮	⋮	⋮	⋮	⋮	⋮		⋮
100	100	0.000	0.000	0.000	0.000	0.000	0.000	0.000	⋯	0.000

Order Selection

A stochastic model should be able to replicate the statistical characteristics of the modeled variable as best as possible but at the same time should remain as simple as possible. For example, a second order Markov model would generally be better at modeling a stochastic variable than a first order model. However, with m unique states, the second order MTM will be m times the size of the first order MTM making the second order model more complicated and more difficult to handle. Therefore, unless the second order model represents a certain statistical characteristic of the modeled variable significantly better than the first order model, the first order model should be chosen. The same argument would apply when considering higher order models. The question of choosing the "*best*" order of the Markov model is therefore an important one.

A number of statistical methods for order selection have been proposed in literature [15, 21]. These methods are based on chi-square tests and involve the calculation of the likelihood function [15]. For example, the method proposed in [21] involves the formation of MTMs of various orders and calculation of Akaike information criterion (AIC) value given by:

$$AIC = (-2)\log\mathcal{L} + 2k. \tag{3.10}$$

where $\mathcal{L}$ is the maximum likelihood of the model and k is the number of independently adjusted parameters within the model (degrees of freedom).

Denoting the transition probabilities of an n^{th} order Markov chain by $P_{i-n,\ldots,i-1,j}$ and the frequency of these transitions in the data set by $f_{i-n,\ldots,i-1,j}$, the log-likelihood function would be given by:

$$\log\mathcal{L} = \sum_{i-n,\ldots,i-1,j} f_{i-n,\ldots,i-1,j}\log P_{i-n,\ldots,i-1,j} \tag{3.11}$$

where $P_{i-n,\ldots,i-1,j} = f_{i-n,\ldots,i-1,j}/f_{i-n,\ldots,i-1}$ is the maximum likelihood estimate from the sample data of the unknown transition probabilities of the population. As the order of the Markov model increases, the term $(-2)\log\mathcal{L}$ in (3.10) reduces while $2k$ increases. The appropriate model is then the one that minimizes the AIC. However, if $f_{i-n,\ldots,i-1,j}$ is equal to zero, $f_{i-n,\ldots,i-1,j}\log P_{i-n,\ldots,i-1,j}$ is undefined. And as seen from Tables 3.2 and 3.3, the MTMs are generally very sparse and have numerous zero values making the order selection methods based on a calculation of the likelihood function impracticable.

In an n^{th} order Markov model, the observation at time t is dependent only on the observations at times $t-1, t-2, \ldots, t-n$. It is assumed that the observation at time t is statistically independent of the observations at times $t-n-1, t-n-2, \ldots$. If, however, for the given data set, the observation at time t has significant conditional dependence on the observations at times $t-n-1, t-n-2, \ldots$, then an n^{th} order model wouldn't be able to correctly represent this characteristic. The order of the Markov model can therefore be selected by checking the conditional dependency in the modeled data set between observations at various lags. This characteristic can be evaluated using the partial autocorrelation function (PACF). The partial autocorrelation between k'_t and k'_{t-h} is the conditional cor-

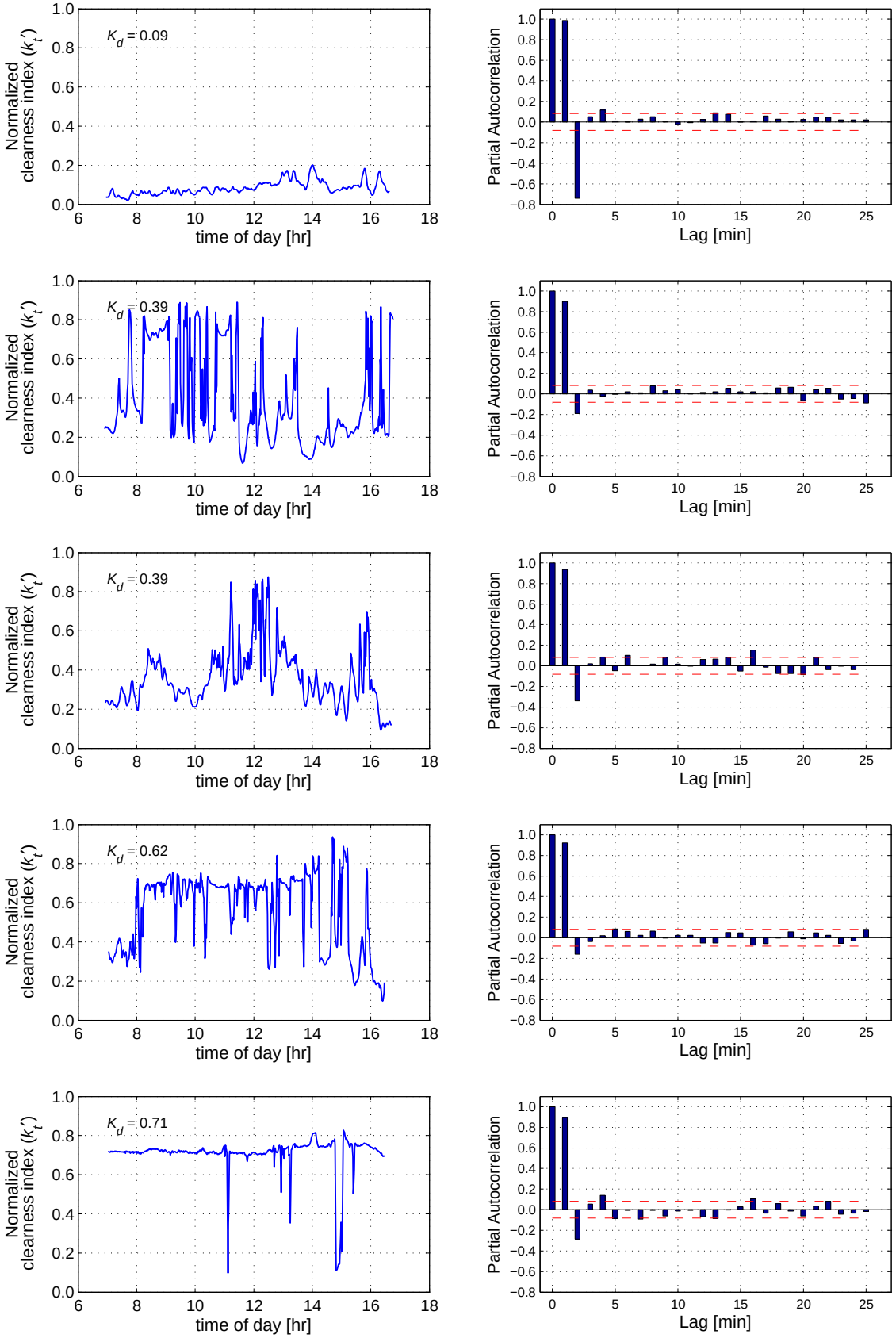

Fig. 3.4: Plots of k_t' and corresponding partial autocorrelation plots.

relation between k'_t and k'_{t-h} under the assumption that $k'_{t-1}, k'_{t-2}, \ldots, k'_{t-h-1}$ are known and taken into account. A significant value in the partial correlation between k'_t and k'_{t-h} suggests that the observation at time t is significantly dependent on the observation at time $t-h$. It is for this reason that the PACF is usually used to select the order of an Auto-Regressive (AR) model [14].

Fig. 3.4 shows typical plots of k'_t for days with different K_d values and the corresponding PACF plots. The PACF plots show significant lag-1 partial autocorrelations in all cases. The lag-2 partial autocorrelation is also seen to be statistically significant though less significant than the lag-1 partial autocorrelation. The partial autocorrelation values for lags larger than 2 are generally very close to zero hence not statistically significant. It should be noted that the five plots of Fig. 3.4 are only typical plots and there are as many PACF plots of k'_t as there are days in the data set. Therefore, the PACFs of k'_t for each day in the data set were calculated and Figs. 3.5(a) and 3.5(b) show the obtained plots of the average lag-1, lag-2 and lag-3 PACFs for the various groups of days using the data from Shinjuku and Suita, respectively. Figs. 3.5(a) and 3.5(b) show that the first two lags are statistically significant especially for days with K_d values less than 0.3.

The statistical significance of lags 1 and 2 shown in Figs. 3.4 and 3.5 lead to the selection of a second order Markov model. This is important so as to capture the correlation characteristics especially in days with low K_d values. Second order MTMs were empirically generated from the recorded solar radiation data and these MTMs are used in the synthetic generation of 1-minute solar radiation data.

3.3 Model validation

The validity of the probabilistic model presented in this chapter is tested by comparing the statistical properties of data synthetically generated using the model to the statistical properties of the observed data. In this section, first, a methodology for synthetically generating solar radiation data using the empirically derived MTMs is described. Then, the synthetically generated data sets is grouped into 15 groups as was done with the test data during the construction of the transition matrices (see Section 3.2.3). The statistical properties of each of these groups were then compared to determine the validity of the proposed Markov model. The statistical properties compared were the statistical parameters (mean, standard deviation, skewness and kurtosis), probability distributions, autocorrelation functions, and the minute-to-minute radiation fluctuations.

3.3.1 Methodology for synthetic generation of solar PV data

The main concept in the use of an n^{th} order Markov model in the synthetic generation of data is that the observation at a time instant t is dependent on the n previous observations. This means that a random variable is chosen from a probability distribution that is dependent on the n previous observations. The probability distribution of k_t (the observation at time t) appears in the row in the MTM corresponding to the n previous observations. This row is the probability distribution vector, $P(t)$, of the observation at

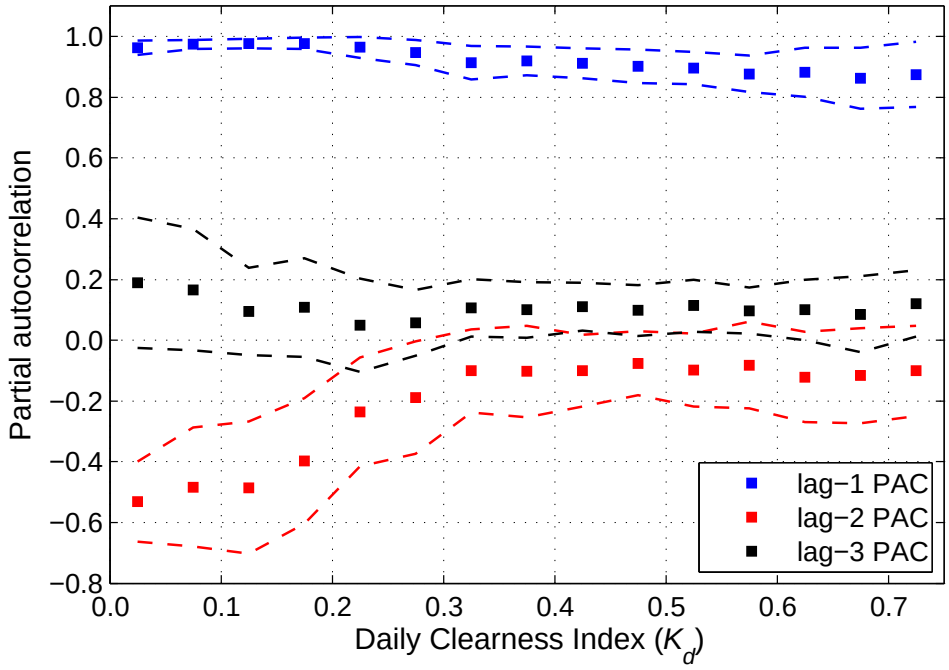

(a)

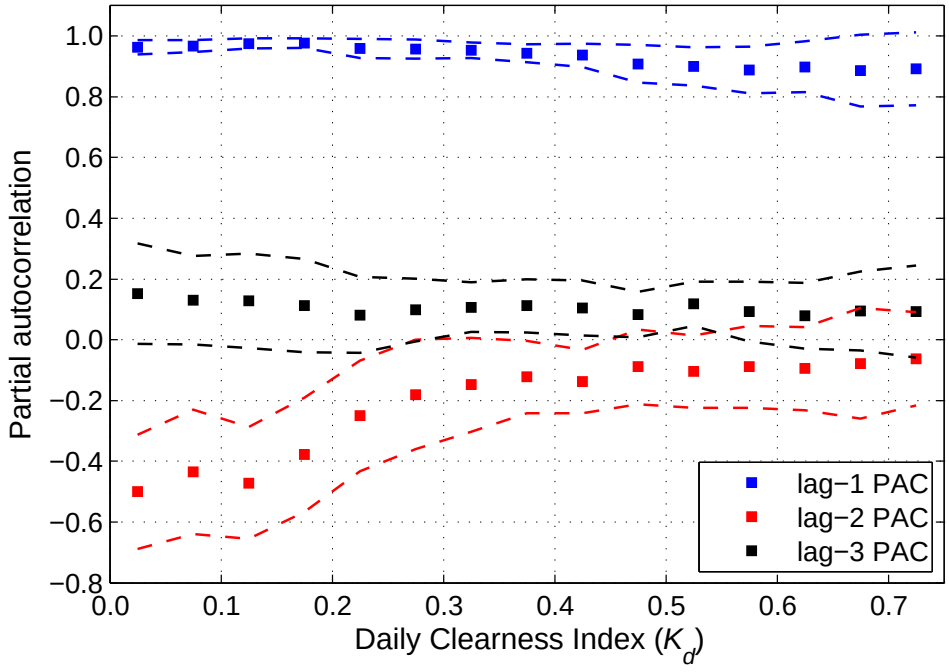

(b)

Fig. 3.5: Average lag-1, lag-2, and lag-3 partial autocorrelation coefficients of k'_t against daily clearness index (K_d) for (a) Shinjuku, Tokyo and (b) Suita, Osaka. Dashed lines indicate the standard deviation of the estimates.

time t. $F(t)$ is the corresponding cumulative distribution vector if:

$$F_h(t) = \sum_{i=1}^{h} P_i(t) \tag{3.12}$$

where $P_i(t)$ is the i^{th} entry in $P(t)$ and $F_h(t)$ is the h^{th} entry in $F(t)$. The subscript h is used instead of n because n has been extensively used in this thesis to denote the order of the Markov model.

The state X_t can therefore be generated by picking a random number r from a uniform distribution [0,1] and mapping it onto $F(t)$ i.e. if $F_{i-1}(t) < r \leq F_i(t)$, then $X_t = i$. By assuming that the cumulative distribution curve is linear between states $i-1$ and i, the synthetically generated normalized 1-min. clearness index is obtained using the transformation:

$$k'_{ts} = \frac{1}{m}\left\{(i-1) + \frac{r - F_{i-1}(t)}{F_i(t) - F_{i-1}(t)}\right\} \tag{3.13}$$

where $m = 100$ is the number of states. The subscript s is used to indicate that this is a synthetically generated variable. For a given value of K_d, the appropriate transition matrix is chosen and then using equations (3.12) and (3.13), sequences of k'_{ts} data are synthetically generated.

Methodology summary

In summary, starting from a set of K_d data, synthetic sets of k'_t are generated for each day through the following steps:

1, Using solar geometry equations (see Appendix C), the extraterrestrial solar radiation H_e for each minute during the day is calculated. H_e is greater than 0 between sunrise and sunset and equal to 0 otherwise.

2, Depending on the value of K_d, the appropriate second order MTM is selected. For example, the MTM shown in part in Table 3.3 will be selected if the K_d value for the day lies between 0.00 and 0.05.

3, The algorithm is initialized by setting k'_{1s} and k'_{2s} equal to K_d. In this way, the row in the MTM selected in step 2 corresponding to the value of $k'_{1s} = k'_{2s} = K_d$ is used as the probability distribution vector for generating k'_{3s}. k'_{1s}, k'_{2s}, ... correspond to the values of the k'_{ts} variable at 12:01am, 12:02am, ... Hence, a number of simulations of k'_{ts} data will be done before sunrise. This ensures a different value of k'_{ts} at sunrise for different simulation runs.

4, Using a random number picked from a uniform distribution $[0, 1]$, k'_{3s} is generated as described by (3.13). The row in the MTM corresponding to the values of k'_{2s} and k'_{3s} is used as the probability distribution vector for generating k'_{4s}. Subsequent values k'_{5s}, k'_{6s}, ..., k'_{1440s} are generated similarly.

5, The synthetically generated k'_{ts} sequence is converted to k_{ts} using (3.7) and finally to 1-minute global solar radiation H data using (3.6).

6, From the H data, the synthetically generated value of the daily clearness index K_{ds}

is calculated. If $|K_d - K_{ds}|/K_d < \delta$, where δ is a previously selected tolerance, the procedure is stopped. Otherwise it is restarted from step 3. It was observed that the model requires an average of 4.2 iterations to generate a k'_t sequence which gives a K_{ds} value that is within 2% of the initial K_d value.

Fig. 3.6 shows plots of observed and synthetically generated global solar radiation data for five days with different K_d values[3]. An initial look at the plots of Fig. 3.6 shows similarities suggesting that the methodology is able to produce synthetic data sets similar to observed data. The two plots for $K_d = 0.09$ (typical cloudy day) show smooth profiles of low solar radiation values. Large fluctuations are generally absent. Clearer days ($K_d = 0.39$ and $K_d = 0.62$) have more pronounced fluctuations due to the presence of numerous scattered clouds in the sky. A very clear day ($K_d = 0.71$) has a generally smooth profile with isolated large fluctuations - a consequence of the appearance of isolated clouds along the sun's path in the sky. The fluctuation characteristics being evident in both the observed and synthetically generated data sets implies that the Markov model is capable of generating data similar to observed data. Mathematically however, the validity of the proposed methodology is tested by comparing the statistical properties of the synthetically generated data with those of the test data. The statistical properties compared were the statistical parameters (mean, standard deviation, skewness and kurtosis), probability distributions, autocorrelation functions, and the minute-to-minute radiation fluctuations.

3.3.2 Statistical parameters

The plots in Fig. 3.7 compare the general statistical parameters (ordinary moments) obtained from the synthetically generated normalized 1-min. clearness index data with those obtained from the two sets of observed data. Equations for calculating the four statistical measures (mean, standard deviation, skewness and kurtosis) are given in appendix B. The plots show a good agreement between the statistical properties of the observed and synthetically generated data sets. The replication of the mean of k'_t is mainly a result of calibration and the use of the step 6 in the methodology (see Section 3.3.1) which ensures that the synthetically generated plot produces a K_d value very close to the input daily clearness index.

However, slight differences are observed in the plots of standard deviation. Generally, for days with K_d greater than 0.3, the values of standard deviation obtained from Shinjuku data are lower than the values obtained from Suita data. This is because the two locations have different climatic characteristics. A lower value of standard deviation suggests that the type of clouds found in an area are more uniform hence do not produce as many large fluctuations in solar radiation. This shows that the nature of clouds has a significant dependence on location. The overall model used in the methodology combined the two sets of data hence the plot of standard deviation from the synthetically generated data sets doesn't deviate significantly from the standard deviation plots for either location. The

[3]Fig. 3.6 shows two plots for days with a K_d value of 0.39. These plots highlight the stochastic nature of the data as it is possible to have two days with similar amounts of total daily irradiation but very different in terms of inter-temporal fluctuations.

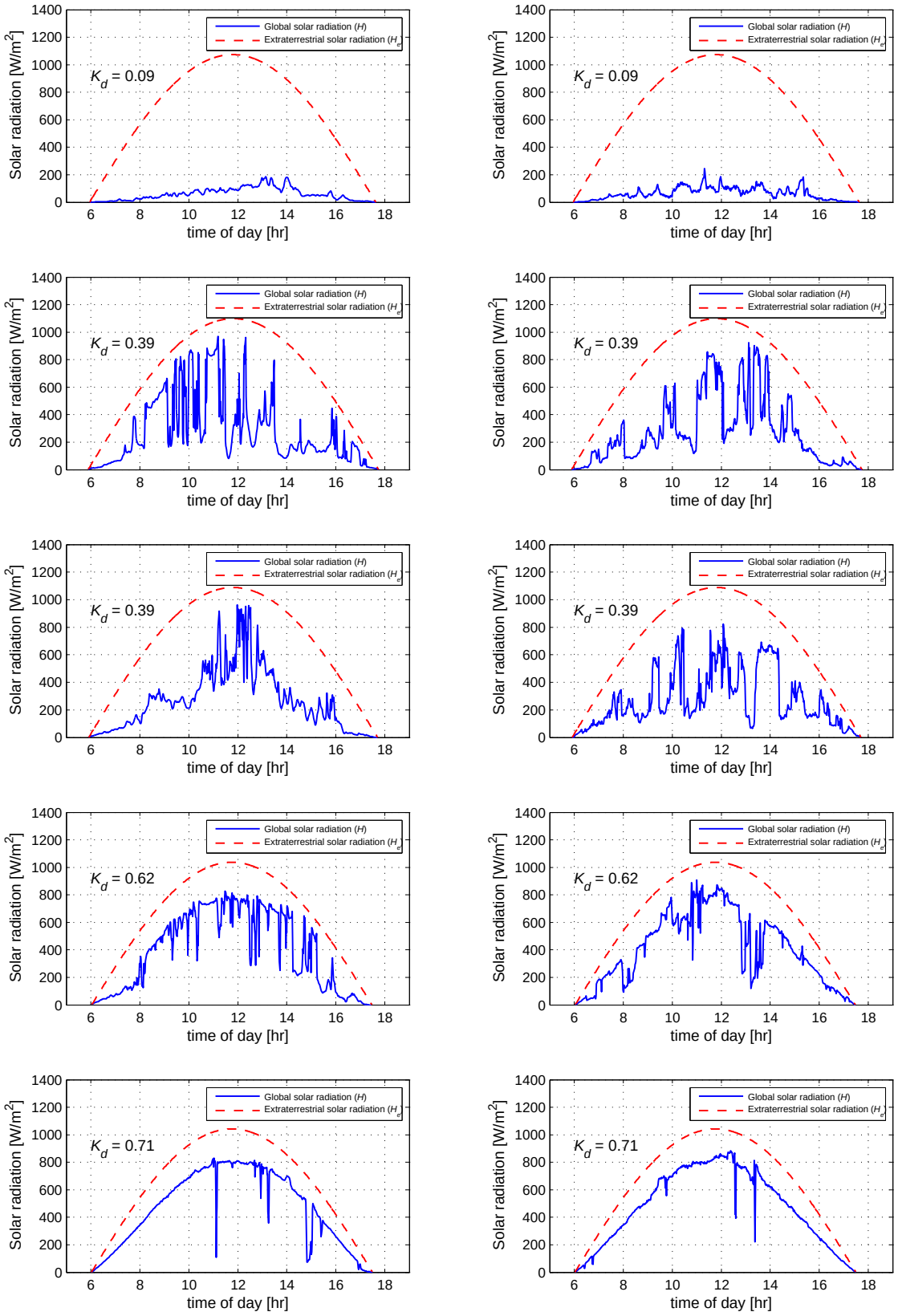

(a) (b)

Fig. 3.6: Solar radiation plots for days with different values of K_d: (a) observed, (b) synthetically generated.

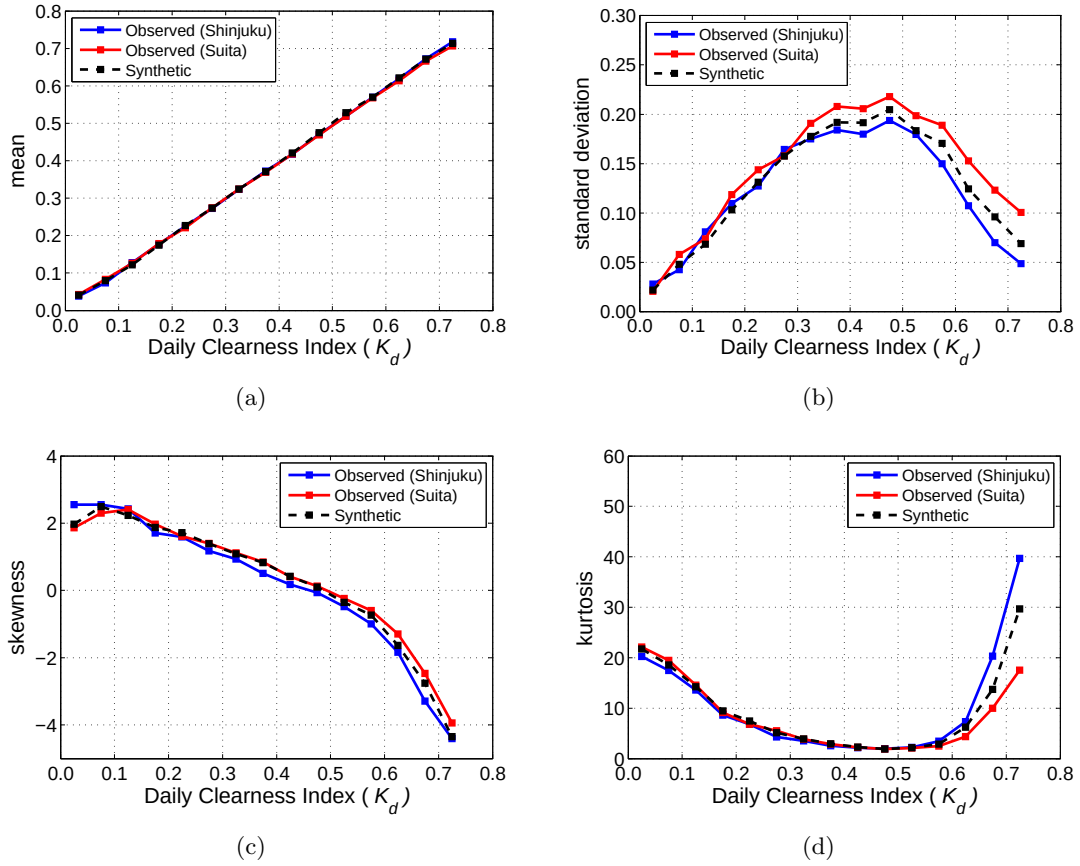

Fig. 3.7: Comparison of general statistical parameters of the observed k_t' and synthetic k_{ts}' data sets: (a) mean, (b) standard deviation, (c) skewness, (d) kurtosis.

slight differences in the skewness and kurtosis measures seen in Figs. 3.7(c) and 3.7(d) can also be explained by the difference in location.

3.3.3 Probability density functions

Fig. 3.8 shows the probability density function (pdf) plots of the normalized 1-min clearness index (k_t') data for each of the fifteen classes of days. The plots show a close agreement between the pdf plots of the observed and synthetic data sets. An important observation is that the synthetic data sets preserve the bimodal[4] characteristic of the observed pdf plots especially for classes of days with K_d values between 0.25 and 0.65. The lower modes of the pdfs of k_t' occur around $k_t' = 0.3$ while the upper modes occur around $k_t' = 0.7$. References [9] and [11] have also highlighted this bimodality characteristic in the pdf plots for high temporal resolution solar radiation data.

While generally a close agreement is observed between the various pdf plots, certain differences are observed. In Fig. 3.8, the pdf plots for Shinjuku data have significantly higher peaks than the pdf plots for Suita data for the groups of days with K_d values ranging between 0.40 and 0.65. This suggests that the nature of the radiation data has

[4] A bimodal distribution is a probability distribution with two different modes which appear as distinct peaks (local maxima) in the probability density function.

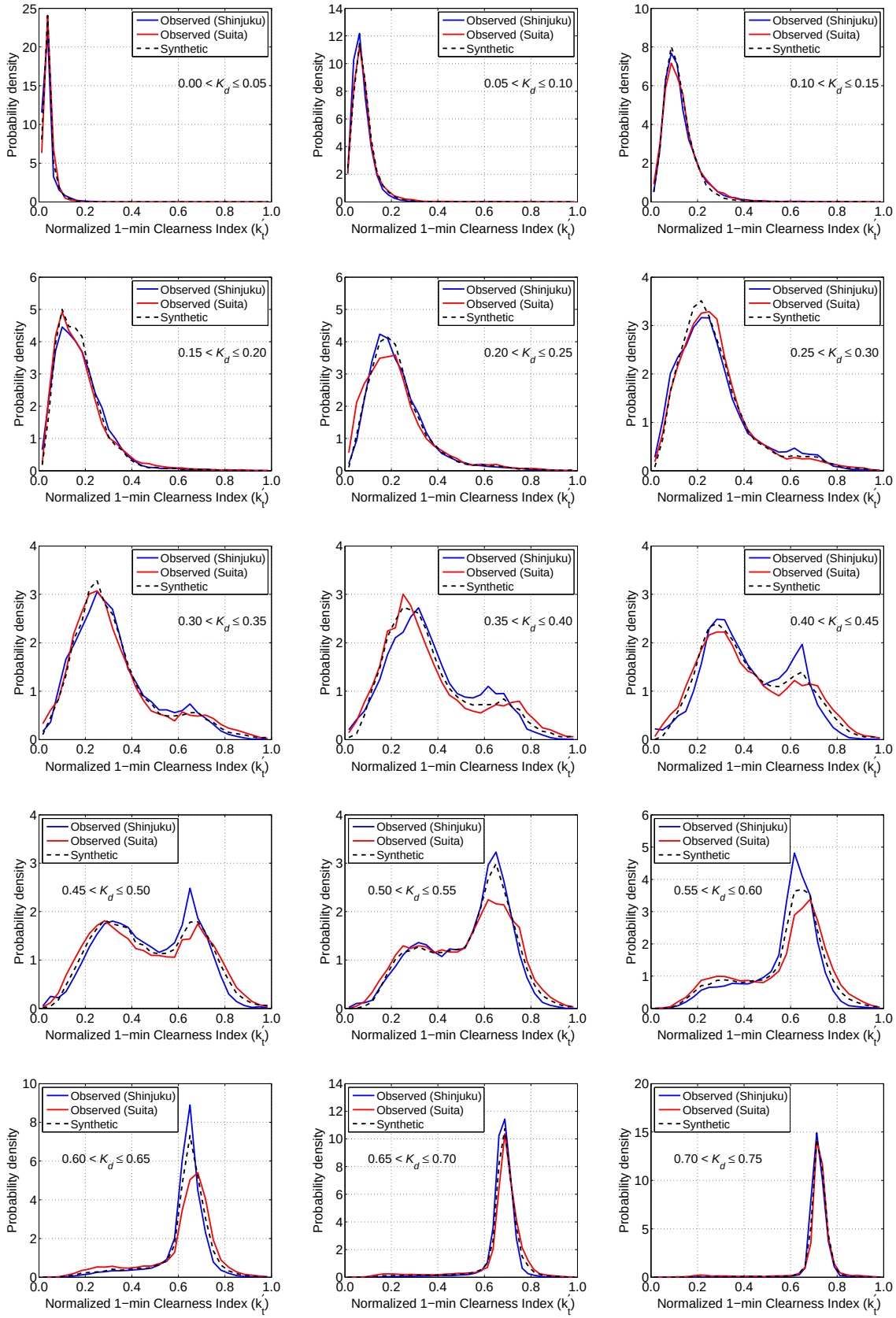

Fig. 3.8: Probability distributions of k_t' for observed and synthetically generated data sets for different classes of days.

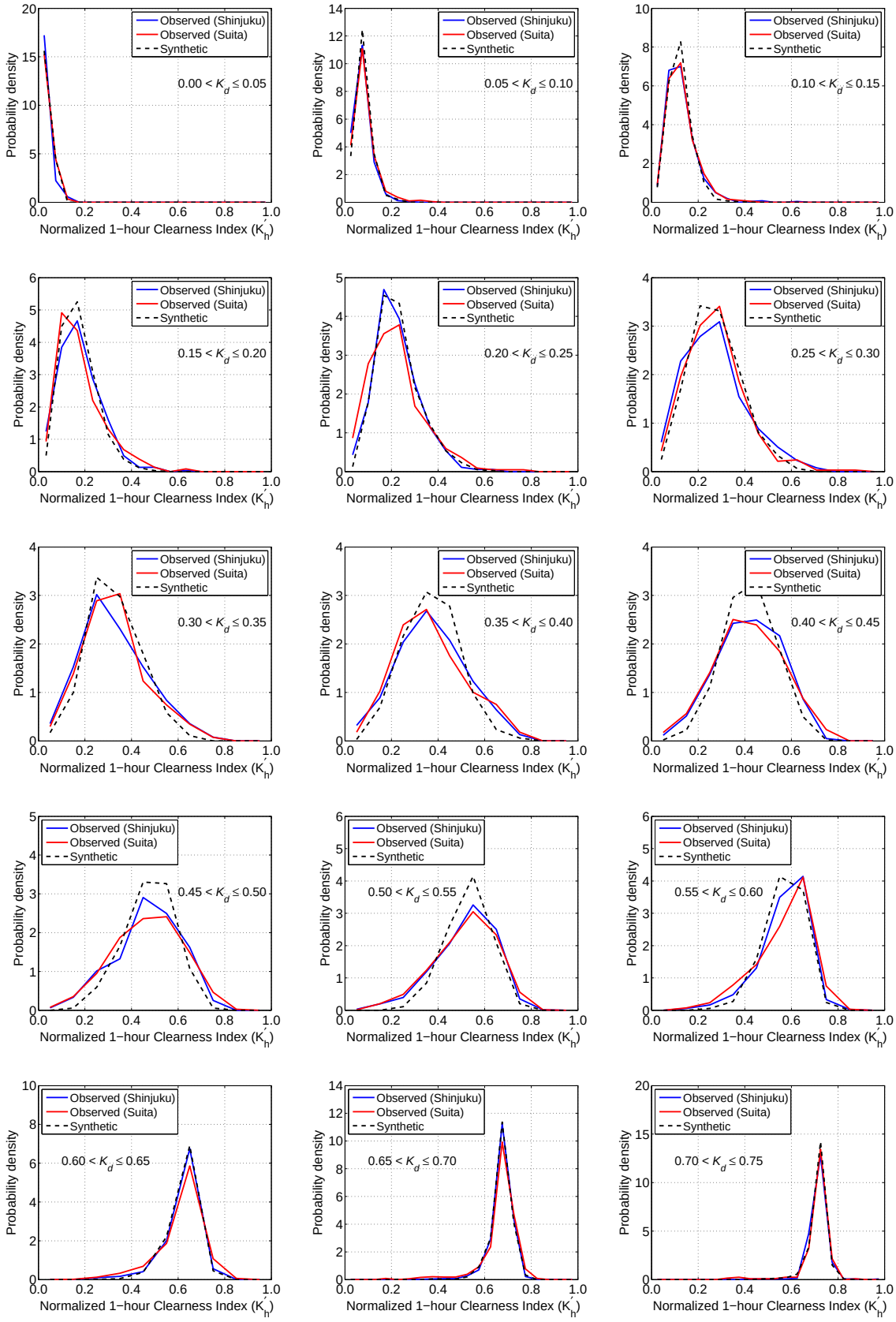

Fig. 3.9: Probability distributions of K_h' for observed and synthetically generated data sets for different classes of days.

a dependence on the location from which it was taken due to differences in the nature of clouds and/or atmospheric effects at the particular locations. This conclusion is a confirmation of the differences in standard deviation plots shown in Fig. 3.7(b). While the nature of the clouds and the atmosphere are quite complex and beyond the scope of this thesis, in simple terms, the nature of clouds and the atmosphere at Suita result in more scattering of incoming radiation compared to the scattering of radiation observed at Shinjuku. Consequently, larger fluctuations are observed at Suita resulting in larger values of standard deviation and consequently lower peaks in the pdf plots.

k_t' is the normalized form of the 1-min clearness index (k_t) which is defined as the ratio of the global solar radiation reaching the earth's surface H to the extraterrestrial solar radiation H_e during a *1 minute* period. The hourly clearness index (K_h) on the other hand, is the ratio of H to H_e measured over a *1 hour* period. Since the model presented in this thesis generates 1-minute data, it is necessary to determine whether the synthetically generated 1-min data reproduces the observed hourly clearness index values.

Fig. 3.9 shows the probability density function (pdf) plots of the normalized 1-hour clearness index (K_h') for each of the fifteen groups of days. These plots too show a close agreement between the observed and synthetically generated pdfs. It is also observed that the bimodal characteristic observed in the pdfs of k_t' shown in Fig. 3.8 are not replicated in the pdf plots of K_h' of Fig. 3.9. This is a significant difference between middle to low temporal resolution solar radiation data such as 1-hour data and higher temporal resolution data such as 1-min data.

3.3.4 Autocorrelation functions

Autocorrelation is a measure of the degree of similarity between a time series and a lagged version of itself and is important in identifying periodicities in the time series. Mathematically, given a time series k_t' with a mean μ and variance σ^2, the autocorrelation at lag τ is given by:

$$\rho_\tau = \frac{\mathbb{E}\left[(k_t' - \mu)\left(k_{t-\tau}' - \mu\right)\right]}{\sigma^2}. \tag{3.14}$$

Fig. 3.6 shows plots of observed and synthetically generated solar radiation data for five representative days. The equivalent plots of k_t' and k_{ts}' obtained from these plots are shown in Fig. 3.10(a) and the corresponding autocorrelation functions (ACFs) are shown in Fig. 3.10(b). The ACF plots for the observed k_t' and synthetically generated k_{ts}' data sets shown in Fig. 3.10(b) are generally similar in that they are gradually reducing with no clear periodicities. The biggest difference is seen in the ACF plots for $K_d = 0.09$ where the plot for the observed data is higher than that of the synthetically generated data. This means that consecutive observations in the observed data have higher correlations producing a radiation plot with fewer fluctuations compared to the synthetically generated data.

The partial autocorrelation function (PACF) was used in Section 3.2.3 to select the appropriate order of the Markov model. The PACF for each of the days in the synthetic data set was calculated and Fig. 3.11 shows the obtained plots of the average lag-1, lag-2,

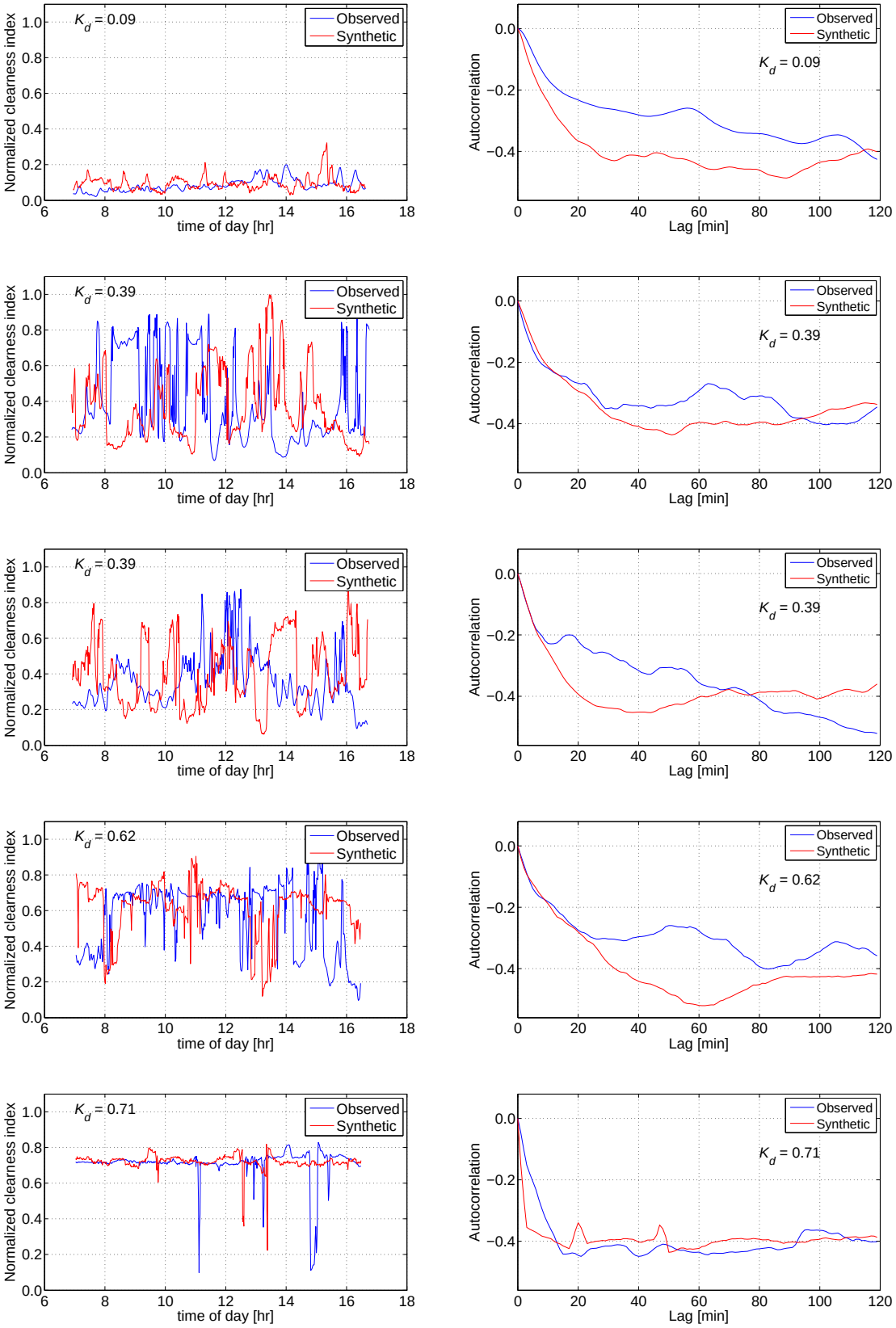

(a) (b)

Fig. 3.10: Plots of (a) observed k'_t and synthetic k'_{ts}, and (b) corresponding autocorrelation plots.

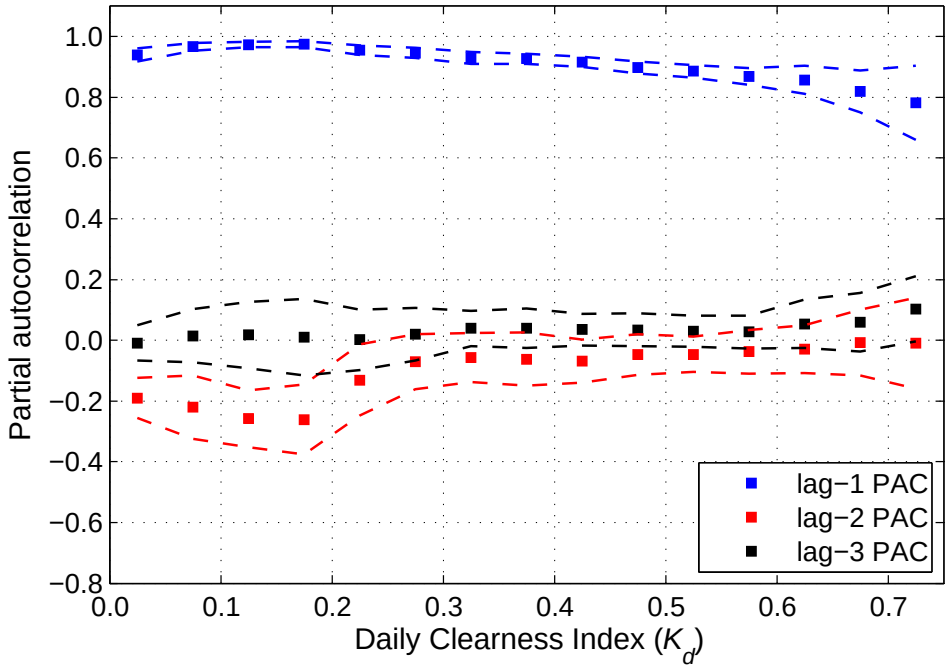

Fig. 3.11: Average lag-1, lag-2, and lag-3 partial autocorrelation coefficients of synthetically generated k'_{ts} data. Dashed lines indicate the standard deviation of the estimates.

and lag-3 PACFs for the various groups of days. When compared to the plots of Fig. 3.10, it is seen that the lag-1 PACF plot is well reproduced in the synthetically generated data set. However, lag-2 and lag-3 PACFs are generally smaller in magnitude than in the observed data sets. This difference can be explained by the fact that the second order Markov model is only an approximation of the process generating the observed data which is actually infinitely complex. The serial correlation is therefore a complex phenomenon that may not be exactly captured by the Markov model.

3.3.5 Minute-to-minute radiation fluctuations

The stochastic model presented in this thesis generates 1-minute solar radiation data. One of the most important differences between such high temporal resolution data and lower temporal resolution data such as hourly data is the presence of significantly large fluctuations in the minute-to-minute transitions. Power system studies such as power quality studies would use data generated from the model to investigate the effects of these short duration fluctuations in solar radiation on the power quality. The model used in generating synthetic data should therefore be able to reproduce these fluctuations and this section compares the minute-to-minute radiation fluctuations in the observed and synthetically generated data sets.

Three categories of minute-to-minute radiation fluctuations ($\Delta H_t = |H_t - H_{t-1}|$) are defined as: small: $\Delta H \leq 50 W/m^2$; medium: $50 W/m^2 < \Delta H \leq 200 W/m^2$; and large: $\Delta H \geq 200 W/m^2$. Fig. 3.12 compares the frequency of occurrence of these fluctuation levels in the two sets of observed data and the synthetically generated data. Fig 3.12(a) shows that; in both the observed and synthetically generated data sets, for all groups

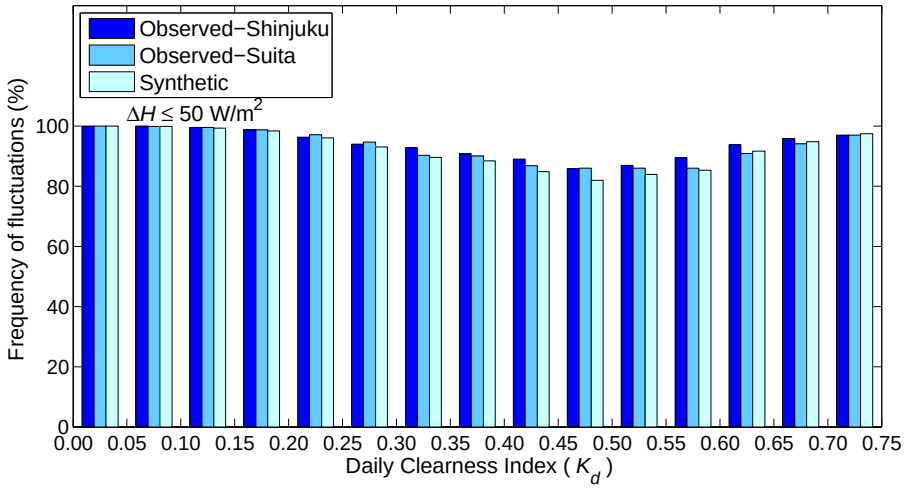

(a)

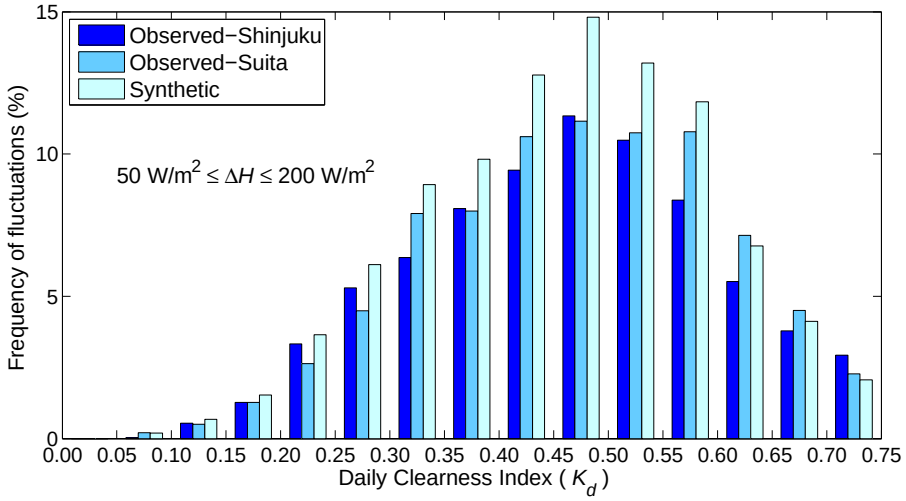

(b)

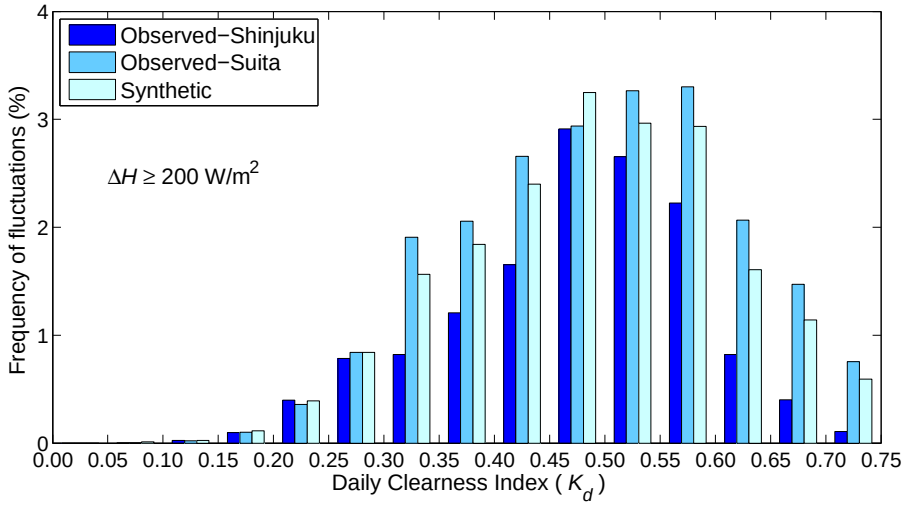

(c)

Fig. 3.12: Comparison of frequency of occurrence of minute-to-minute fluctuations in solar radiation levels: (a) small, (b) medium, and (c) large fluctuations.

of days, more than 85% of the minute-to-minute fluctuations are less than $50W/m^2$. A comparison of the fluctuation levels show that the Markov model does well in reproducing the fluctuations in observed data.

3.4 Summary

A probabilistic model for the synthetic generation of 1-minute solar radiation data has been developed and presented in this chapter. The model is constructed by treating the process generating a normalized form of the 1-minute clearness index (k'_t) as a second order Markov process. The main contributions presented in this work include:

1. A detailed description of the model construction including data trend removal (see Section 3.2.2), model construction (see Section 3.2.3), and model order selection (see Section 3.2.3). A second order Markov model is arrived at based on the autocorrelation characteristics of the observed data.
2. The developed probabilistic model is used in a stochastic methodology described in Section 3.3.1 to generate k'_t data starting from the daily clearness index K_d value.
3. The model was validated by confirming that the statistical characteristics of the synthetic and observed data sets have a good agreement. Specifically, the following points are noted in the validation:
    - the ordinary moments (mean, standard deviation, skewness and kurtosis) and the probability distributions of the stochastic variable are well reproduced in the synthetic data sets.
    - Slight differences are however observed in the autocorrelation characteristics of the observed and synthetic data sets especially for days with low K_d values.
    - The minute-to-minute radiation fluctuations are also well reproduced in the synthetic data sets.

The good agreement in the statistical characteristics of the observed and synthetic data sets confirm the viability of the model in producing data sets similar to observed solar radiation data. This data can be especially useful in probabilistic studies of the effects of increased integration of photovoltaic generators in power systems.

3.5 References

[1] G. Tina, S. Gagliano, and S. Raiti, "Hybrid solar/wind power system probabilistic modelling for long-term performance assessment," *Solar Energy*, vol. 80, no. 5, pp. 578 – 588, 2006. doi: https://doi.org/10.1016/j.solener.2005.03.013.

[2] M. E. Nassar and M. M. A. Salama, "Probabilistic power flow using novel wind and solar probabilistic models," in *2016 IEEE Power and Energy Society General Meeting (PESGM)*, pp. 1–5, July 2016. doi: https://doi.org/10.1109/PESGM.2016.7741568.

[3] R. Aguiar, M. Collares-Pereira, and J. Conde, "Simple procedure for generating sequences of daily radiation values using a library of markov transition matrices," *Solar Energy*, vol. 40, no. 3, pp. 269 – 279, 1988. doi: https://doi.org/10.1016/0038-092X(88)90049-7.

[4] V. Graham, K. Hollands, and T. Unny, "A time series model for K_t with application to global synthetic weather generation," *Solar Energy*, vol. 40, no. 2, pp. 83 – 92, 1988. doi: https://doi.org/10.1016/0038-092X(88)90075-8.

[5] F. O. Hocaoğlu, "Stochastic approach for daily solar radiation modeling," *Solar Energy*, vol. 85, no. 2, pp. 278 – 287, 2011. doi: https://doi.org/10.1016/j.solener.2010.12.003.

[6] V. Graham and K. Hollands, "A method to generate synthetic hourly solar radiation globally," *Solar Energy*, vol. 44, no. 6, pp. 333 – 341, 1990. doi: https://doi.org/10.1016/0038-092X(90)90137-2.

[7] R. Aguiar and M. Collares-Pereira, "TAG: A time-dependent, autoregressive, gaussian model for generating synthetic hourly radiation," *Solar Energy*, vol. 49, no. 3, pp. 167 – 174, 1992. doi: https://doi.org/10.1016/0038-092X(92)90068-L.

[8] D. Laslett, C. Creagh, and P. Jennings, "A method for generating synthetic hourly solar radiation data for any location in the south west of western Australia, in a world wide web page," *Renewable Energy*, vol. 68, pp. 87 – 102, 2014. doi: https://doi.org/10.1016/j.renene.2014.01.015.

[9] M. Jurado, J. Caridad, and V. Ruiz, "Statistical distribution of the clearness index with radiation data integrated over five minute intervals," *Solar Energy*, vol. 55, no. 6, pp. 469 – 473, 1995. doi: https://doi.org/10.1016/0038-092X(95)00067-2.

[10] H. Suehrcke and P. McCormick, "The frequency distribution of instantaneous insolation values," *Solar Energy*, vol. 40, no. 5, pp. 413 – 422, 1988. doi: https://doi.org/10.1016/0038-092X(88)90096-5.

[11] A. Skartveit and J. Olseth, "The probability density and autocorrelation of short-term global and beam irradiance," *Solar Energy*, vol. 49, no. 6, pp. 477 – 487, 1992. doi: https://doi.org/10.1016/0038-092X(92)90155-4.

[12] I. Richardson and M. Thomson, "Integrated simulation of photovoltaic micro-generation and domestic electricity demand: A one-minute resolution open source model," in *Microgen II: 2nd International Conference on Microgeneration and Related Technologies*, (Glasgow, Scotland), 2011. Available from: journals.sagepub.com/doi/10.1177/0957650912454989.

[13] R. Perez, P. Ineichen, R. Seals, and A. Zelenka, "Making full use of the clearness index for parameterizing hourly insolation conditions," *Solar Energy*, vol. 45, no. 2, pp. 111 – 114, 1990. doi: https://doi.org/10.1016/0038-092X(90)90036-C.

[14] P. Brockwell and R. Davis, *Introduction to Time Series and Forecasting*. Springer-Verlag New York, 2002. doi: https://doi.org/10.1007/b97391.

[15] T. W. Anderson and L. A. Goodman, "Statistical inference about markov chains," *Ann. Math. Statist.*, vol. 28, pp. 89–110, 03 1957. doi: https://doi.org/10.1214/aoms/1177707039.

[16] O. Häggström, *Finite Markov Chains and Algorithmic Applications*. Cambridge University Press, 2002. doi: https://doi.org/10.1017/CBO9780511613586.

[17] A. Shamshad, M. Bawadi, W. W. Hussin, T. Majid, and S. Sanusi, "First and second order Markov chain models for synthetic generation of wind speed time series," *Energy*, vol. 30, no. 5, pp. 693 – 708, 2005. doi = https://doi.org/10.1016/j.energy.2004.05.026.

[18] R. Srikanthan and T. McMahon, "Stochastic generation of annual, monthly and daily climate data: A review," *Hydrology and Earth System Sciences Discussions*, vol. 5, no. 4, pp. 653 – 670, 2001. Available from https://hal.archives-ouvertes.fr/hal-00304639.

[19] P. Poggi, G. Notton, M. Muselli, and A. Louche, "Stochastic study of hourly total solar radiation in corsica using a markov model," *International Journal of Climatology*, vol. 20, no. 14, pp. 1843 – 1860, 2000. doi: https://doi.org/10.1002/1097-0088(20001130)20:14%3C1843::AID-JOC561%3E3.0.CO;2-O.

[20] A. Louche, G. Peri, and M. Iqbal, "An analysis of linke turbidity factor," *Solar Energy*, vol. 37, no. 6, pp. 393 – 396, 1986. doi: https://doi.org/10.1016/0038-092X(86)90028-9.

[21] H. Akaike, "A new look at the statistical model identification," *IEEE Transactions on Automatic Control*, vol. 19, pp. 716–723, Dec 1974. doi: https://doi.org/10.1109/TAC.1974.1100705.

CHAPTER 4

Modeling transmission line conductor temperature

4.1 Introduction

This chapter presents a simplified model for estimating the temperature of an overhead transmission line operated under dynamic line ratings. The proposed model is based on numerical approximations of the various components of the more complex International Council on Large Electric Systems (CIGRE) physical model [1]. The resulting simple equations can be used to directly estimate the conductor temperature without the need for iterative calculations which are required in the full CIGRE model. A mathematical validation of the simplified model is carried out by comparing both steady-state and transient-state temperature values obtained using the proposed model to values obtained using the full CIGRE model. The reduction of the computational effort when calculating the conductor temperatures using the simplified model is also illustrated. In addition to the mathematical validation, an experimental validation is also presented. The measured conductor temperature values (for both steady-state and transient-state conditions) are compared with values estimated using the proposed simplified version of the CIGRE model to confirm the validity of the proposed model.

The proposed model has several potential application areas including a fast calculation and adjustment of thermal relay settings, load frequency control, and solutions to real-time optimal power flow problems. In this thesis, the use of the simplified model is illustrated in a transmission line overload risk analysis methodology (see Section 5.6) and in the solution of the optimal power flow problem (see Chapter 6).

4.2 Literature review of overhead conductor temperature estimation

As introduced in Chapter 2, the fluctuating nature of IRE sources leads to a number of new technical challenges in grid operation [2, 3, 4]. One of the concerns is increased variability in line power flows and possibly increased occurrences of violations of the thermal constraints of lines as a result. Now, while the thermal limit of a transmission line is usually given as a maximum current value, strictly speaking, the thermal limit refers to the maximum

temperature that the conductor is allowed to reach. When this value is exceeded, the conductor experiences excessive sag or suffers a significant loss of strength [5, 6]. However, in practice the temperature value is not used when setting the thermal limit. Rather, an equivalent current value termed "ampacity" is used, which is defined as the conductor current that would result in the maximum allowable conductor temperature for a given set of weather conditions [6, 7, 8]. The ampacity value can be easily converted to an active power or apparent power value depending on the voltage level to give a maximum power limit.

As introduced in Section 2.3, there are two types of thermal ratings are in use today: static line rating (SLR) and dynamic line rating (DLR) [6, 7]. A static line rating is employed in cases where the worst case weather assumptions are used to calculate the ampacity, while the more flexible dynamic line rating is employed when real time weather data is used instead [9, 10, 11, 12]. While the DLR relaxes the conservativeness of the power flow constraints set by the SLR, the direct use of the conductor temperature in setting the thermal limits results in a higher transmission line loadability [13, 14].

The direct use of transmission line temperature limits in system operation requires either direct or indirect monitoring of the conductor temperatures [15]. Direct monitoring could be achieved through the direct measurement of the temperature, sag [16, 17], or tension [18], while indirect monitoring requires measurements of the conductor current and weather parameters along the line followed by the use mathematical models that relate the conductor temperature to the current and weather parameters to estimate the conductor temperature [15].

Mathematical models that describe the thermal dynamics overhead conductors have been empirically derived [1, 19] and can be used to estimate the conductor temperature for a given set of current and ambient weather conditions. In Japan and in many other countries, the CIGRE model [1] has been adopted for the calculation of conductor temperatures, and hence the ampacity. However, the model uses complicated implicit functions which require iterative calculations in order to find a solution [1]. The nonlinear nature of these models makes it difficult to explicitly incorporate the thermal characteristics of overhead conductors in determining optimal operation of power systems e.g. in the solution to the real-time optimal power flow (OPF) problem.

In this chapter, approximations for the various components of the CIGRE model are presented. The result is a simplified model which reduces the computational effort when using conductor temperature directly to set the thermal limits of transmission lines. The simplified CIGRE model approximates the conductor temperature in steady-state as a quadratic function of the square of the current in which the constants are determined explicitly by the weather parameters. The equation is easily extended to the transient state as a first-order ordinary differential equation (ODE) from which explicit equations describing the conductor temperature as a function of time can be derived depending on the change in conductor current.

4.3 CIGRE model for determining the temperature of an overhead conductor

The CIGRE conductor temperature model consists of sets of equations describing the electro-thermal processes acting on an overhead conductor. The individual models are then combined to calculate the temperature of the conductor [1]. The various processes result in either conductor heat loss or conductor heat gain. The main thermal processes, which are illustrated in Fig. 4.1, include heat loss due to radiative cooling; heat loss due to convective cooling (mainly due to blowing wind); heat gain due to ohmic losses in the conductor (Joule heat gain); and heat gain due to solar heating. Other processes whose effects are not as significant and therefore ignored in the final model include heat loss due to evaporative cooling; heat gain due to magnetic heating; and heat gain due to corona discharge. The equations used to determine the various heat gain and heat loss terms are described in the following subsections.

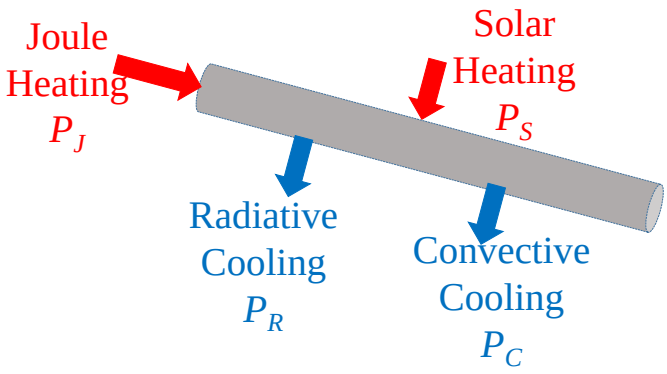

Fig. 4.1: Heating and cooling processes in an overhead conductor.

4.3.1 Modeling conductor heating and cooling processes

Radiative heat loss

The conductor heat gain by radiation P_R [W/m] is calculated using the Stefan-Boltzmann equation:

$$P_R = \pi\sigma_B\epsilon D\left[(T_c+273)^4-(T_a+273)^4\right] \qquad \text{[W/m]} \tag{4.1}$$

where $\sigma_B = 5.67\times10^{-8}$ W $\cdot$ m^{-2} $\cdot^{\circ}$ C^{-4} is the Stefan-Boltzmann constant, ϵ is the radiation emissivity factor, and D [m] is the overall diameter of the conductor.

Convective heat loss

A collection of empirical equations, which have been independently validated by Japanese utilities [20], is used to determine the convective heat loss P_C [W/m] [1]. Generally, P_C is given as:

$$P_C = \pi\lambda_f Nu(T_c-T_a) \qquad \text{[W/m]} \tag{4.2}$$

where λ_f [W/(m $\cdot^\circ$ C)] is the thermal conductivity of air and Nu is the Nusselt number. The term λ_f is determined by:

$$\lambda_f = 0.0242 + 0.000072\,T_f \qquad [\mathrm{W/m}] \tag{4.3}$$

where $T_f = 0.5(T_c + T_a)$ [°C] is the temperature of the air film. Two sets of equations for Nu are provided that are dependent on the wind speed v [m/s]. At very low wind speeds $v \approx 0$ m/s, the natural convection equation is used, while at higher wind speeds, the forced convection equation used.

In the case of natural convection, Nu is given by:

$$Nu = A_1\,(Gr \cdot Pr)^m \tag{4.4}$$

where the Grashof number Gr and the Prandtl number Pr are:

$$Gr = \frac{gD^3T_x}{(T_f + 273)\,\vartheta_f^2} \tag{4.5}$$

and

$$Pr = 0.715 + 0.00025\,T_f \tag{4.6}$$

where $g = 9.81$ m/s^2 is the gravitational acceleration and ϑ_f $\left[\mathrm{m^2/s}\right]$ is the kinematic viscosity of air, and is given as:

$$\vartheta_f = (1.32 + 0.0095\,T_f) \times 10^{-5} \qquad \left[\mathrm{m^2/s}\right] \tag{4.7}$$

In (4.4), A_1 and m are constants that depend on the product $Gr \cdot Pr$, as follows:

$$\begin{aligned} A_1 &= 0.85 \text{ and } m = 0.188 \qquad \text{if } 10^2 \le Gr \cdot Pr \le 10^4 \\ A_1 &= 0.48 \text{ and } m = 0.250 \qquad \text{if } 10^4 \le Gr \cdot Pr \le 10^6 \end{aligned} \tag{4.8}$$

In the case of forced convection:

$$Nu = K_\delta B_1 (Re)^n \tag{4.9}$$

where K_δ is a factor that accounts for the wind direction δ[1] and Re is the Reynolds number. K_δ is given by:

$$K_\delta = \begin{cases} 0.42 + 0.68(\sin\delta)^{1.08}, & \text{for } 0^\circ \le \delta < 24^\circ \\ 0.42 + 0.58(\sin\delta)^{0.90}, & \text{for } 24^\circ \le \delta \le 90^\circ \end{cases} \tag{4.10}$$

A plot of K_δ versus $\sin\delta$ is shown in Fig. 4.2. In the figure, an almost linear relationship between the two variables is seen. For low wind speeds ($v < 0.5$ m/s), there is no preferred wind direction and the value $K_\delta = 0.55$ is used.

The Reynold's number Re is given as:

$$Re = \frac{\rho_r v D}{\vartheta_f} \tag{4.11}$$

where ρ_r is the relative air density and $\rho_r = \rho/\rho_0$, where ρ $\left[\mathrm{g/m^3}\right]$ is the air density at height y [m] above the sea level and ρ_0 is the air density at sea level ($y = 0$). An empirical

[1]The wind angle δ is measured as the acute angle between the wind direction and the conductor axis so that $\delta = 0°$ for the wind direction parallel to the conductor axis and $\delta = 90°$ for the wind direction perpendicular to the conductor axis.

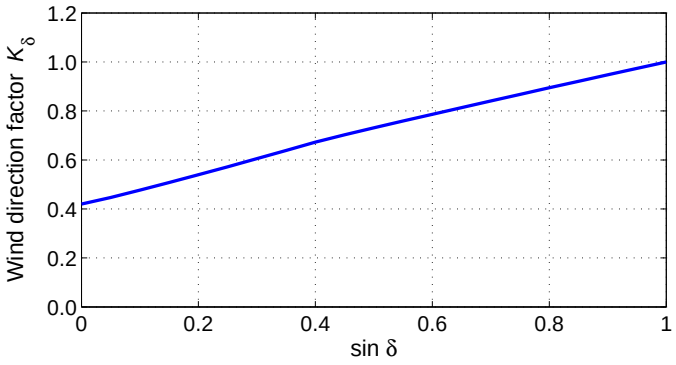

Fig. 4.2: Plot of the wind direction factor versus $\sin\delta$.

equation for ρ_r is given as:

$$\rho_r = exp\left(-1.16 \times 10^{-4} y\right) \tag{4.12}$$

In (4.9), B_1 and n are constants that depend on Re and the conductor roughness R_f, as follows:

$$\begin{aligned} B_1 &= 0.641 \text{ and } n = 0.471, && \text{if } Re \leq 2650 \\ B_1 &= 0.178 \text{ and } n = 0.633, && \text{if } Re > 2650 \text{ and } R_f \leq 0.05 \\ B_1 &= 0.048 \text{ and } n = 0.800, && \text{if } Re > 2650 \text{ and } R_f > 0.05 \end{aligned} \tag{4.13}$$

and $R_f = 0.5\, d/\left(D - d\right)$, where d is the diameter of the outer layer wires for stranded conductors.

For wind speeds less than 0.5 m/s, the larger value of Nu between the forced and natural convection values is chosen, while for higher wind speeds, the forced convection value is used.

Solar heating

The solar heat gain is calculated as:

$$P_S = \alpha_s D S \qquad [\text{W/m}] \tag{4.14}$$

where α_s is the solar radiation absorptivity factor of the conductor and S [W/m] is the global solar radiation. Typically, α_s varies from 0.23 for bright conductors to 0.95 for weathered conductors with a value of 0.5 proposed for general estimation purposes[1].

Joule heating

The equation for the Joule heat gain is given as:

$$P_J = I_c^2 R_{ac} \qquad [\text{W/m}] \tag{4.15}$$

where I_c [A] is the ac current flowing through the conductor and R_{ac} [Ω/m] is the ac resistance. R_{ac} is calculated as:

$$R_{ac} = R_{ac}^0 \left[1 + \alpha(T_c - T_{ref})\right] \qquad [\Omega/\text{m}] \tag{4.16}$$

where α [/°C] is the temperature coefficient of resistance and R^0_{ac} is the ac resistance at the reference temperature T_{ref} [°C]. The term R^0_{ac} is given by:

$$R^0_{ac} = k_s R^0_{dc} \qquad [\Omega/\text{m}] \tag{4.17}$$

where R^0_{dc} is the per unit dc resistance at T_{ref}, and k_s is a factor that accounts for the skin effect [1].

The CIGRE model uses a constant value $k_s = 1.0123$ for non-ferrous conductors, and a set of empirical equations to calculate k_s that depend on the conductor size, current, and construction for steel-cored conductors[2]. Typical k_s curves are shown in Fig. 4.3, which illustrate the non-linear relationship between k_s and I_c, especially for small 1- or 2-layer steel-cored conductors[3].

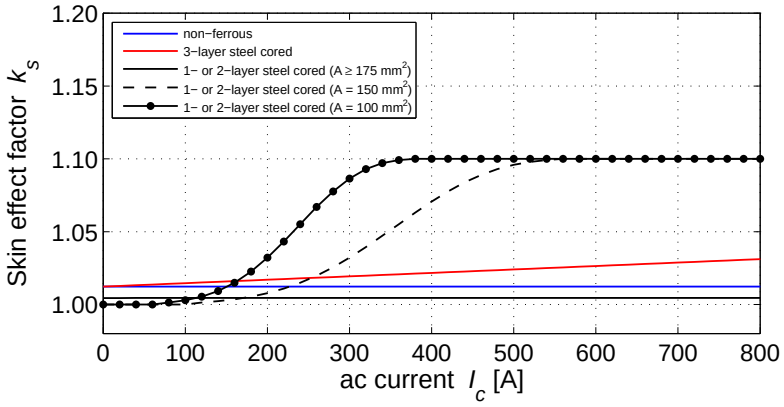

Fig. 4.3: Relationship between skin effect factor k_s and conductor current I_c.

4.3.2 Steady-state and transient-state equations

Steady-state equation

Under steady-state conditions, the conductor is in thermal equilibrium and the conductor heat gain equals the heat loss. The heat balance equation is thus written as:

$$P_J + P_S = P_C + P_R \qquad [\text{W/m}] \tag{4.18}$$

where P_J, P_S, P_C, and P_R are as given in the preceding sections.

Since P_R, P_C, and P_J are implicit functions of T_c as seen in (4.1), (4.2), and (4.15), respectively, it is not possible to write an explicit equation that can be used to solve for T_c given the weather and loading conditions. Therefore, an iterative algorithm that searches for the value of T_c that balances the heat gain and heat loss terms is required. An implementation of such a scheme is illustrated in Algorithm 1. Starting from an initial guess T_c^{init}, the value of the conductor temperature is iteratively updated using the Newton formula until the change in conductor temperature is less than a pre-set tolerance T_{err}^{max}.

[2]Various models in the literature use varying empirical equations to calculate k_s, depending on the power frequency, conductor current, conductor size, and construction [1, 19, 21, 22].

[3]The equations relating k_s to I_c for different conductor types and sizes can be found in [1].

Algorithm 1 Calculate Conductor Temperature (CIGRE Model)

procedure CONDUCTORTEMPCALCCIGRE
    $T_l \leftarrow T_l^{init}$
    while $|T_{err}| > T_{err}^{max}$ **do**
        $\Delta P = P_J + P_S - P_C - P_R$
        $T_{err} \leftarrow \frac{\Delta P}{\frac{d\Delta P}{dT_l}}$
        $T_l \leftarrow T_l + T_{err}$
    end while
    return T_l
end procedure

Transient-state equation

Under non-steady-state conditions, the heat stored in the conductor equals the difference between the heat gain and heat loss, i.e.:

$$mc\frac{dT_x}{dt} = (P_J + P_S) - (P_C + P_R) \qquad [\text{W/m}] \tag{4.19}$$

where m [kg/m] is the conductor mass per unit length, c [$\text{W} \cdot \text{s}/\left(\text{kg} \cdot^{\circ} \text{C}\right)$] is the specific heat capacity of the conductor, and $T_x = T_c - T_a$ [°C] is the difference between the conductor temperature T_c and the ambient temperature T_a. Again, similar to the steady-state model, an explicit transient-state equation cannot be derived. Therefore, the value of conductor temperature as either the current or weather parameters change can only be computed using a discrete form of the transient state equation (4.19), given as:

$$T_c(t + \Delta t) = T_c(t) + \Delta T_c(t) \tag{4.20}$$

where

$$\Delta T_c(t) = \frac{\Delta t}{mc}\Big(P_J(t) + P_S(t) - P_C(t) - P_R(t)\Big). \tag{4.21}$$

4.4 Simplified conductor temperature model

As described in Section 4.3, the nonlinear nature of the CIGRE model increases the computational burden when incorporating conductor temperature dynamics in determining optimal system operation. In order to address this challenge, a simplified form of the CIGRE model was derived and is described in the following subsections.

4.4.1 CIGRE model simplification

By defining $T_x = T_c - T_a$ as the temperature difference between the conductor and surrounding air, the various components of the conductor thermal equation described in Section 4.3 are re-written as:

$$P_R = h_r T_x \qquad [\text{W/m}] \tag{4.22}$$

$$P_C = h_c T_x \qquad [\text{W/m}] \tag{4.23}$$

$$P_J = I_c^2 R_{ac} \qquad [\text{W/m}] \tag{4.24}$$

$$P_S = \alpha_s D S \qquad [\text{W/m}] \tag{4.25}$$

where h_r [W/ (m ·° C)] and h_c [W/ (m ·° C)] are the radiative and convective heat loss coefficients, respectively. As can be deduced from the various models described in Section 4.3, h_r, h_c, and R_{ac} are dependent on the conductor temperature, which results in the need for an iterative method to solve for T_c. This section presents approximate equations of h_r, h_c and R_{ac} that are independent of T_c, and therefore result in explicit equations for determining T_c in both the steady and transient states.

Radiative cooling

The radiative cooling equation (4.1) is re-written as:

$$P_R = \pi\sigma_B\epsilon D\left(T_x^3 + 4T_x^2T_A + 6T_xT_A^2 + 4T_A^3\right)T_x \qquad [\text{W/m}] \tag{4.26}$$

where $T_A = T_a + 273$. The radiative cooling coefficient h_r can then be given by:

$$h_r = \pi\sigma_B\epsilon D\gamma_r \qquad [\text{W/ (m} \cdot^\circ \text{ C)}] \tag{4.27}$$

where

$$\gamma_r = T_x^3 + 4T_x^2T_A + 6T_xT_A^2 + 4T_A^3 \qquad \left[(^\circ\text{C})^3\right]. \tag{4.28}$$

γ_r is a cubic function of T_x with a minimum value of $4T_A^3$ at $T_x = 0$. As an approximation, since $T_A >> T_x$, the terms $4T_x^2T_A$ and T_x^3 in (4.28) can be ignored. An approximate equation for the radiative cooling coefficient can thus be written as:

$$h_r' = h_{r0} + pT_x \qquad [\text{W/ (m} \cdot^\circ \text{ C)}] \tag{4.29}$$

where $h_{r0} = 4\pi\sigma_B\epsilon D(T_a + 273)^3$ and $p = 6\pi\sigma_B\epsilon D(T_a + 273)^2$.

Finally, the radiative cooling equation can be approximated by:

$$P_R' = h_{r0}T_x + pT_x^2 \qquad [\text{W/m}] \tag{4.30}$$

Convective Cooling

A general equation for the convective cooling coefficient h_c is given as:

$$h_c = K_1K_\delta w^n \qquad [\text{W/ (m} \cdot^\circ \text{ C)}] \tag{4.31}$$

where $w = \rho Dv$ is the air flow rate across the conductor, K_δ is the wind direction factor, and K_1 and n depend on T_a and v.

In the case of forced convection, K_δ is given by (4.10) and plotted in Fig. 4.2, while the factor K_1 is given by:

$$K_1 = \frac{B_1\pi\lambda_f}{(\rho_0\vartheta_f)^n} \tag{4.32}$$

where the constants B_1 and n vary according to (4.13). K_1 is clearly a function of T_f only since λ_f and ϑ_f are functions of T_f. The variation of K_1 with T_f for different values of Re and R_f are as plotted in Fig. 4.4, which shows that K_1 is almost constant over the operational range of T_f. This observation means that the convective cooling coefficient for forced convection is essentially independent of either T_c or T_a. Therefore, K_1 is approximated by a constant in each of the three cases.

As an approximation, the values of K_1 corresponding to a T_f value of 100 °C are used in each case. This means that, at an ambient temperature of 40 °C, the conductor tem-

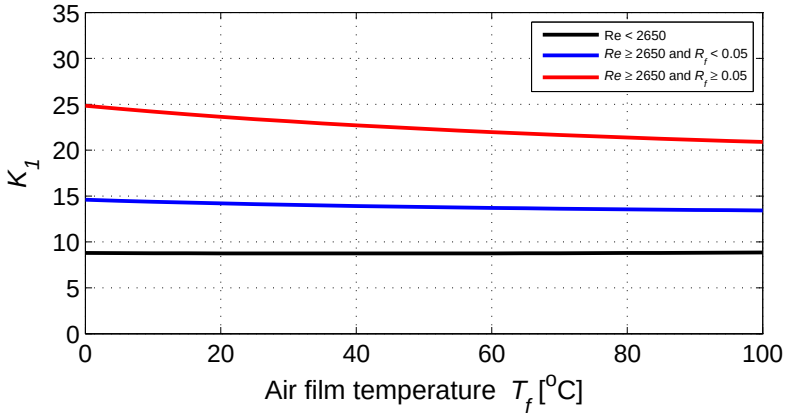

Fig. 4.4: Plot of K_1 against the film temperature T_f.

perature would be 160 °C, which is well above the maximum allowable temperature limits of most conductors [23, 24, 25]. The result here is a slightly conservative approximation of the convective cooling effect on the conductor under normal operating conditions. The equations for approximating h_c in the case of forced convection can then be given as:

For low wind speeds:

$$h'_{cfl} = 8.74\, K_\delta w^{0.471} \tag{4.33}$$

and for high wind speeds:

$$h'_{cfh} = \begin{cases} 13.44\, K_\delta w^{0.633} & \text{if } R_f \leq 0.05 \\ 20.89\, K_\delta w^{0.800} & \text{if } R_f > 0.05 \end{cases} \tag{4.34}$$

In the case of natural convection, $n = 0$, $K_\delta = 1$, and K_1 is given by:

$$K_1 = \pi \lambda_f A_1 \left(Gr \cdot Pr\right)^m \tag{4.35}$$

where A_1 and m are dependent on the product $Gr \cdot Pr$, as given by (4.8). The region $10^2 \leq Gr \cdot Pr \leq 10^4$ corresponds to low values of T_c. Considering the more significant region $10^4 \leq Gr \cdot Pr \leq 10^6$, (4.35) is re-written as:

$$K_1 = K_2 D^{0.75} \tag{4.36}$$

where

$$K_2 = \pi g \lambda_f A_1 \left(\frac{g T_x Pr}{\left(T_f + 273\right) \vartheta_f^2} \right)^{0.25}. \tag{4.37}$$

Clearly, K_2 is a function of T_x and T_a and the relationship is plotted in Fig. 4.5.

As seen in Fig. 4.5, the factor K_2 increases as T_x increases, which shows that the natural convection cooling effect increases as the difference between the conductor temperature and ambient temperature increases. Then, as an approximation, the value of K_2 that corresponds to a T_x value of 20 °C ($T_c = 60$ °C for $T_a = 40$ °C) is used. This value is conservative for high values of T_c, which correspond to large currents and are the more significant region in network operation. The approximate equation for the convection cooling

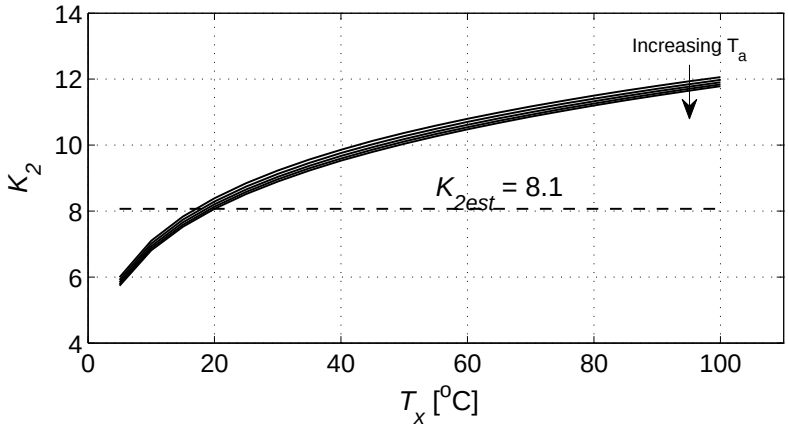

Fig. 4.5: Plot of K_2 against T_x over the ambient temperature range $0\,^{\circ}\mathrm{C} \leq T_a \leq 40\,^{\circ}\mathrm{C}$.

coefficient under natural convection is thus:

$$h'_{cn} = 8.1\, D^{0.75} \qquad [\mathrm{W}/(\mathrm{m} \cdot^{\circ} \mathrm{C})] \tag{4.38}$$

Finally, similar to the CIGRE model procedure [1], the approximated coefficient of convection cooling is taken as the largest between h'_{cfl}, h'_{cfh}, and h'_{cn}:

$$h'_c = \max(h'_{cfl}, h'_{cfh}, h'_{cn}) \qquad [\mathrm{W}/(\mathrm{m} \cdot^{\circ} \mathrm{C})] \tag{4.39}$$

and the convective cooling equation can thus be approximated by:

$$P'_C = h'_c T_x \qquad [\mathrm{W/m}]\,. \tag{4.40}$$

Solar Heating

As can be seen in (4.14), P_S is independent of T_c and hence, because it is straightforward, the solar heating equation needs no modification.

Joule Heating

The ac resistance R_{ac} and hence the Joule heat gain is dependent on T_c. Furthermore, the skin effect factor in (4.17) is dependent on I_c, which results in a highly non-linear relationship between P_J and I_c. As an approximation, the skin effect factor in (4.17) is approximated by a constant (k_{s0}), which is its value at the static line rating of the conductor. The ac resistance at the reference temperature R^{ref}_{ac} can then be given by:

$$R^{ref}_{ac} = k_{s0} R^0_{dc} \qquad [\Omega/\mathrm{m}]\,. \tag{4.41}$$

The ac resistance at the conductor temperature T_c can then be approximated by:

$$R'_{ac} = R^{ref}_{ac}\,[1 + \alpha(T_c - T_{ref})]\,. \tag{4.42}$$

Now:

$$\begin{aligned} R'_{ac} &= R^{ref}_{ac}\,[1 + \alpha(T_c - T_a + T_a - T_{ref})] \\ &= R^{ref}_{ac}\,[1 + \alpha(T_a - T_{ref})] + \alpha(T_c - T_a) R^{ref}_{ac} \\ &= R'_{ac}(T_a) + \alpha T_x R^{ref}_{ac} \end{aligned} \tag{4.43}$$

In (4.43) $R'_{ac}(T_a)$ represents the ac resistance at $T_c = T_a$ (minimum conductor temperature) while $\alpha T_x R^{ref}_{ac}$ represents the increase in resistance as the conductor temperature increases above T_a.

4.4.2 Steady-state and transient-state equations

On the basis of the simplified forms of the various components of the conductor thermal equation given in the preceding subsections, a simplified version of the CIGRE model can be derived for both the steady- and transient-state cases.

Steady-state equation

In steady-state, the heat gain and heat loss terms are equated, i.e.

$$h_{r0}T_x + pT_x^2 + h'_c T_x = \alpha_s DS + R'_{ac}(T_a)I_c^2 + \alpha T_x R^{ref}_{ac} I_c^2 \tag{4.44}$$

which on re-arrangement gives:

$$h'_0 T_x = \alpha_s DS + R'_{ac}(T_a)I_c^2 + \alpha R^{ref}_{ac} T_x I_c^2 - pT_x^2 \tag{4.45}$$

where $h'_0 = h_{r0} + h'_c$. The T_x variable on the right hand side of (4.45) can be eliminated using an approximate relationship between T_x and I_c^2 as follows.

At high values of current, the $R'_{ac}(T_a)I_c^2$ term is much larger than the other terms on the right hand side of (4.45) and an approximate steady-state equation is written as:

$$h'_0 T_x \approx R'_{ac}(T_a)I_c^2. \tag{4.46}$$

or:

$$T_x \approx \frac{R'_{ac}(T_a)}{h'_0} I_c^2 \tag{4.47}$$

By substituting (4.47) into the right hand side of (4.45) and re-arranging, the following equation for T'_c is arrived at:

$$T'_c = \beta_0 + \beta_1 I_c^2 + \beta_2 I_c^4 \qquad [^{\circ}\mathrm{C}]\,, \tag{4.48}$$

where:

$$\beta_0 = T_a + \frac{\alpha_s DS}{h'_0} \qquad [^{\circ}\mathrm{C}]\,, \tag{4.49}$$

$$\beta_1 = \frac{R'_{ac}(T_a)}{h'_0} \qquad [^{\circ}\mathrm{C/A^2}]\,, \tag{4.50}$$

$$\beta_2 = \frac{\beta_1}{h'_0}\left(\alpha R^{ref}_{ac} - p\beta_1\right) \qquad [^{\circ}\mathrm{C/A^4}]\,. \tag{4.51}$$

Equation (4.48) is an approximate equation for determining the conductor temperature in steady-state. It gives T'_c as a quadratic function of the square of the current using the coefficients β_0, β_1, and β_2, which can be explicitly determined using (4.49)-(4.51) for a given set of weather parameters. Fig. 4.6 compares the procedures for calculating the steady-state conductor temperature using the CIGRE and simplified models.

Transient-state equation

An imbalance between the heat gain and heat loss terms results in a change in conductor temperature, as described by the transient-state equation (4.19). From (4.45), the

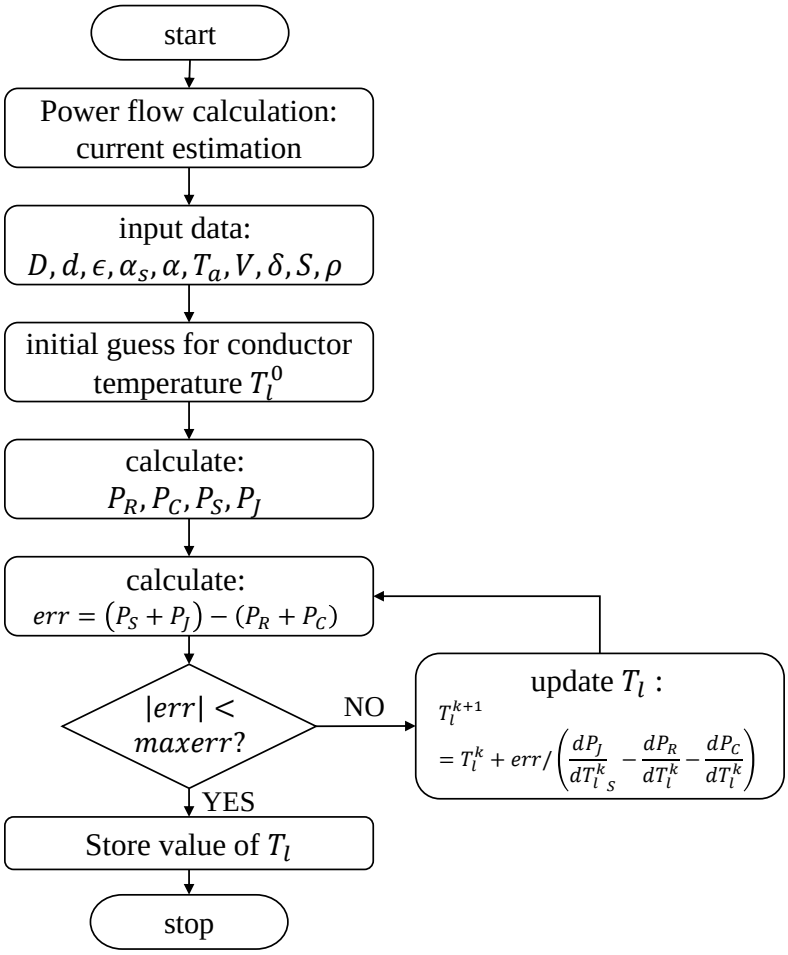

(a)

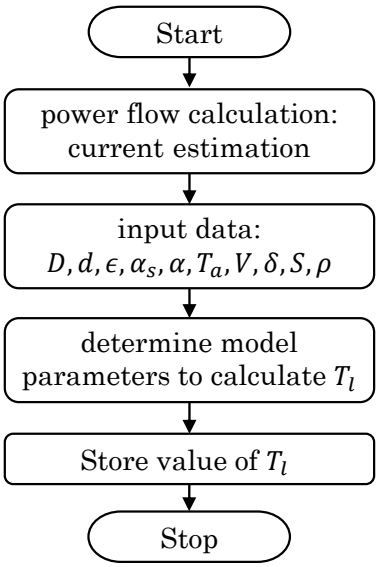

(b)

Fig. 4.6: Algorithm flowcharts for calculating the steady-state conductor temperature (a) using the CIGRE model and (b) using the simplified model.

transient-state heat balance equation is written as:

$$mc\frac{dT_x}{dt} = \alpha_s DS + R'_{ac}(T_a)I_c^2 + \alpha T_x R_{ac}^{ref} I_c^2 - h'_0 T_x - pT_x^2 \tag{4.52}$$

which leads to:

$$\frac{dT'_c}{dt} = \frac{h'_0}{mc}\Big(\beta_0 + \beta_1 I_c^2 + \beta_2 I_c^4 - T'_c\Big). \tag{4.53}$$

Equation (4.53) is a first-order ODE from which explicit equations of T'_c can be derived, depending on the nature of the change in the current or weather parameters.

4.5 Mathematical validation

In this section, in an effort to validate the approximations introduced in Section 4.4, the values of the conductor temperature obtained using the approximate equations (T'_c) are compared to those obtained using the CIGRE model (T_c). For comparison purposes, two conductors typically used in the Japanese transmission network [22] are studied: the 160 mm^2, 30/7 aluminum conductor steel-reinforced (ACSR) conductor and the 810 mm^2, 45/7 thermal resistant aluminum-alloy conductor steel-reinforced (TACSR) conductor. The conductor parameters are listed in Table 4.1. The ACSR conductor has two aluminum layers made from hard-drawn aluminum while the TACSR conductor has three aluminum layers made from aluminum alloy. The difference in the number of layers provides different resistance characteristics, as illustrated in Fig. 4.3, while the ability of the TACSR to operate at higher temperatures [24] allows for observation of the model characteristics in higher temperature ranges. The base values for the ambient weather parameters used in the calculations, which are also the values used to determine the static line rating, are listed in Table 4.2. All calculations were performed on a laptop computer with a 2.40-GHz Intel Core i7 processor running MATLAB 2010a.

Table 4.1: Conductor data [24]

Property [Units]	160 mm^2 ACSR	810 mm^2 TACSR
number of aluminum layers	2	3
overall conductor diameter D [mm]	18.2	38.4
diameter of outer layer conductor d [mm]	2.6	4.8
ac resistance at ref. temp. R_{ac}^{ref} [Ω/km]	0.1824	0.0373
Temp. coefficient of resistance α [per °C]	0.0040	0.0036
absorptivity factor α_s	0.5	0.5
emissivity factor ϵ	0.5	0.5
maximum conductor temperature[a] T_{max} [°C]	90	150
heat capacity mc [J/m-K]	525	2185
Static Line Rating[b] [A]	471	1942

[a] These values of T_{max} are typical for conductors in the Japanese network[22, 24].

[b] Ratings calculated using the base weather parameter values are shown in Table 4.2.

Table 4.2: Base values for weather parameters

Parameter [Units]	Value
Ambient temperature T_a [°C]	40
Wind speed V [m/s]	0.5
Wind angle δ [°]	45
Global solar radiation S [W/m^2]	1000
Relative air density ρ_r	1.0

4.5.1 Steady-state temperature

Figure 4.7 compares the steady-state conductor temperature T_c' evaluated using (4.48) to the values of T_c obtained using the CIGRE model for the 160 mm^2 ACSR conductor. The plots on the left show the closeness of fit between the two models while the plots on the right show the corresponding magnitudes of approximation error (calculated as $error = T_c - T_c'$). Algorithm 1 was used to calculate T_c (CIGRE model) with the simulation parameters: $T_c^{init} = T_a$ and $T_{err}^{max} = 0.1\,°\text{C}$. In Figs. 4.7(a), 4.7(b), 4.7(c), and 4.7(d), the values of the wind speed, ambient temperature, wind direction, and solar radiation were varied, respectively. In all four cases, the values of the other weather parameters were as given in Table 4.2. Similar plots for the 810 mm^2 TACSR conductor are provided in Fig. 4.8. Generally, the plots show that the approximate equation yields values of T_c' that are almost identical to the values of T_c obtained using the CIGRE model.

The error plots show that the difference in the magnitudes of conductor temperature obtained using the two models is in the range of −10°C to +3°C over the normal operation ranges of the conductors. Points corresponding to the maximum allowed conductor temperatures under the normal and emergency operating conditions are also indicated on the error plots. In the case of the smaller 160mm^2 conductor, the error is slightly greater than zero for large currents. This is the result of an underestimation of the line resistance from (4.43) which is illustrated in Fig. 4.9. In the case of the larger 810mm^2 TACSR conductor, the approximation errors are mainly negative implying a conservative approximation. The magnitude of the error is less than 10°C for conductor temperatures less than the maximum allowed value of 150°C. The error is larger (an even more conservative approximation) for larger conductor temperatures. For both conductors, the case of zero wind direction displays the largest errors. This is however an extremely special case representing weather conditions worse than the worst-case scenario weather conditions used in determining the static line rating.

The plots in Figs. 4.7 and 4.8 confirm that the steady-state conductor temperature has an approximate quadratic relationship with the square of the conductor current, as in (4.48). With zero heating (zero current and zero solar radiation), the conductor steady-state temperature equals the ambient temperature. This is raised by approximately P_s/h_0' for some value of solar radiation, and the constant term β_0 in the quadratic equation is given by (4.49). As the current increases, T_c' increases almost linearly with I_c^2 with the

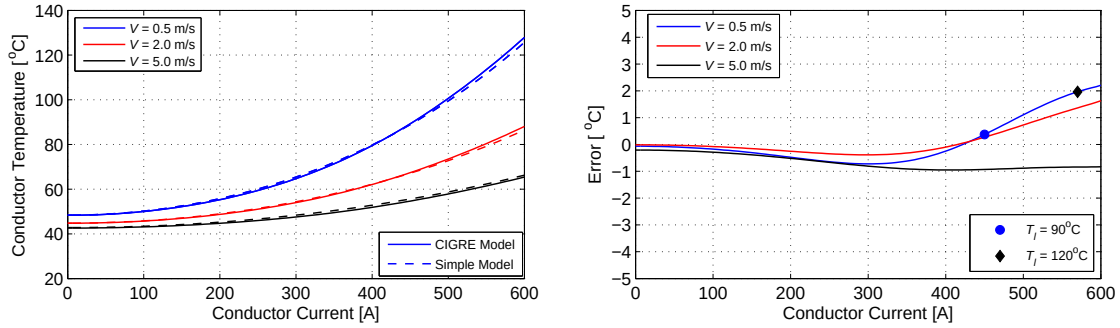

(a)

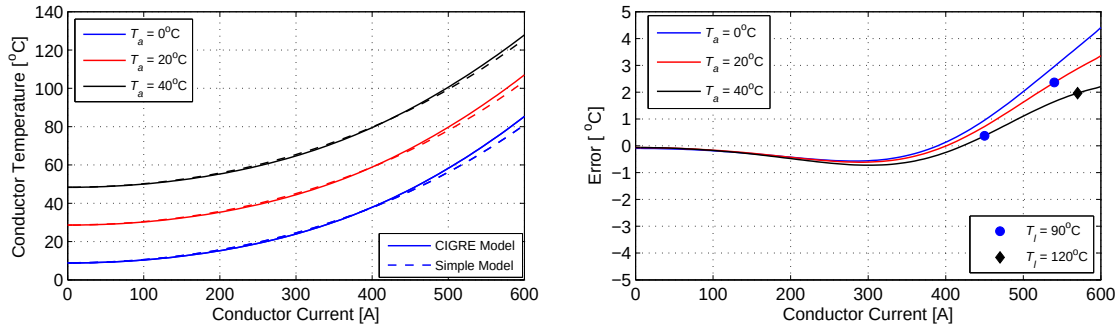

(b)

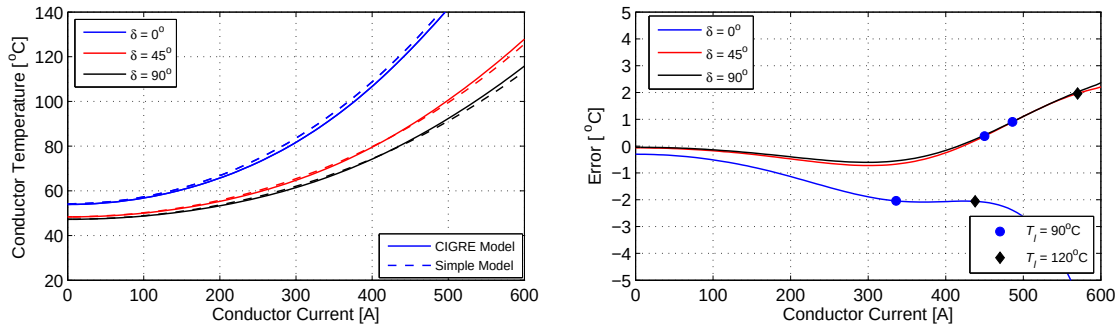

(c)

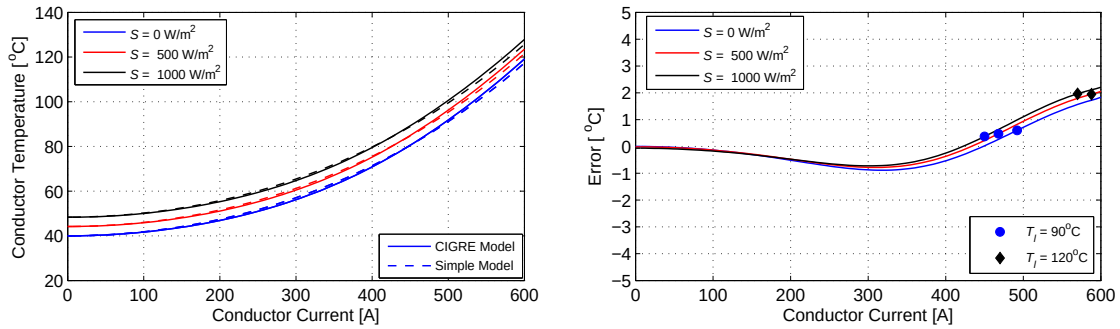

(d)

Fig. 4.7: Comparison of the conductor steady-state temperatures and corresponding errors as calculated using the CIGRE model and as estimated using (4.48) for the 160 mm^2 ACSR conductor while varying: (a) the wind speed; (b) ambient temperature; (c) wind direction; and (d) solar radiation.

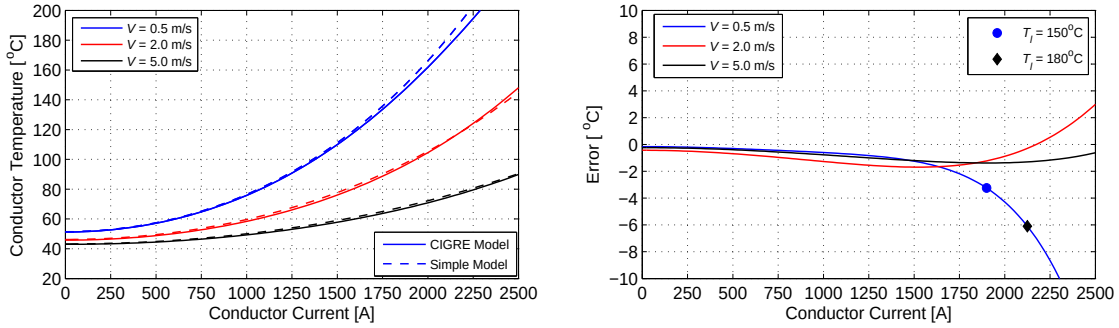

(a)

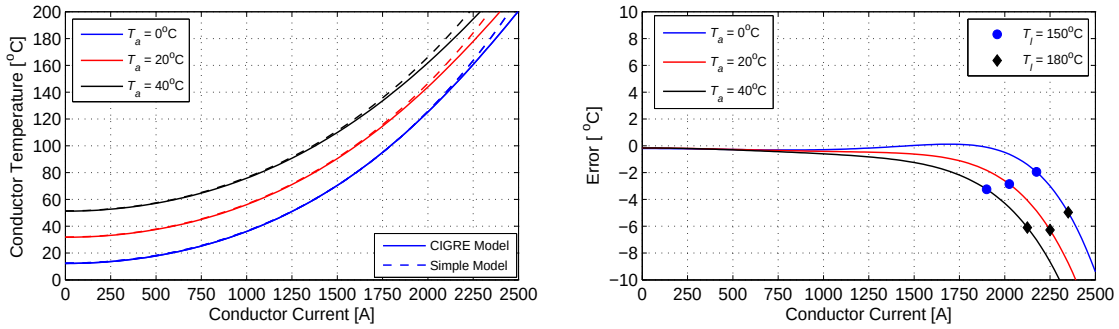

(b)

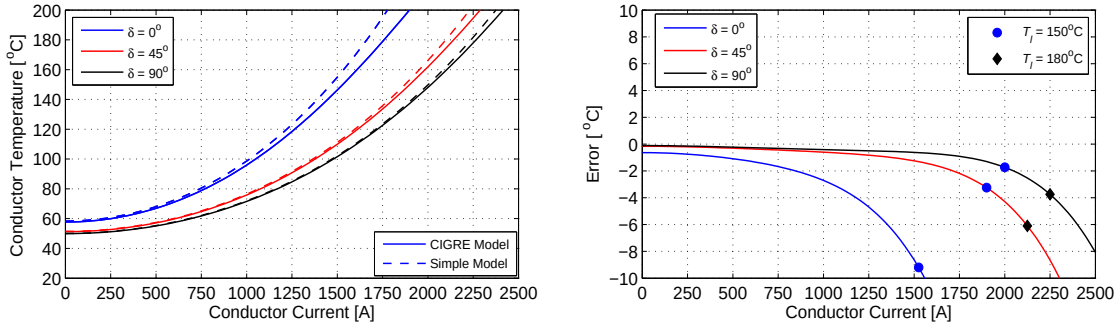

(c)

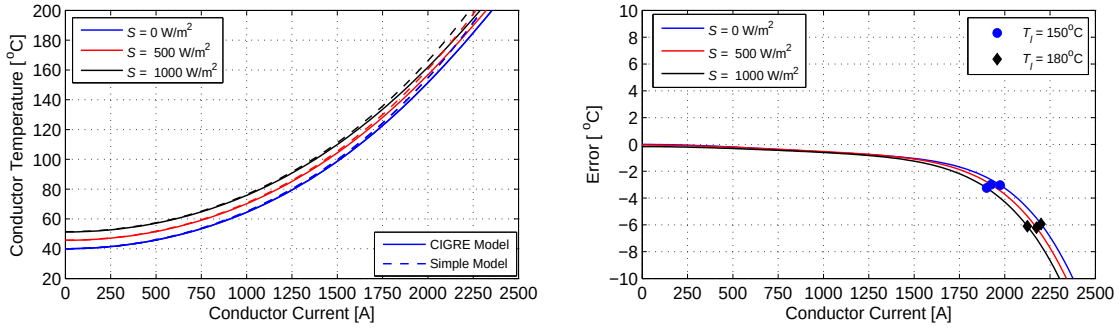

(d)

Fig. 4.8: Comparison of the conductor steady-state temperatures and corresponding errors as calculated using the CIGRE model and as estimated using (4.48) for the 810 mm^2 TACSR conductor while varying: (a) the wind speed; (b) ambient temperature; (c) wind direction; and (d) solar radiation.

constant of proportionality approximated by β_1, as given by (4.50). However, the increase in the conductor temperature results in an increase in the resistance and also an increase in the radiative cooling effect. These two effects are modeled by the two parts of (4.51), i.e. the increased resistance increases T_c' while the increased radiative cooling effect reduces T_c' somewhat. As seen in Figs. 4.7 and 4.8, these equations are valid for the typical normal operational temperature range of the conductors.

The approximations result in the slight differences exhibited in the plots of Figs. 4.7 and 4.8. In order to clearly illustrate the source of the slight differences exhibited in Figs. 4.7 and 4.8, a comparison of the values of ac resistance from the two models is presented. Fig. 4.9 compares the ac resistance as calculated using the CIGRE model and as estimated using (4.42) for both conductors. The plots show that (4.42) produces larger values of resistance for current values less than the line rating (temperatures less than maximum allowable temperature). The difference is significantly larger for the 160 mm^2 ACSR conductor because the approximation of the reference temperature calculated

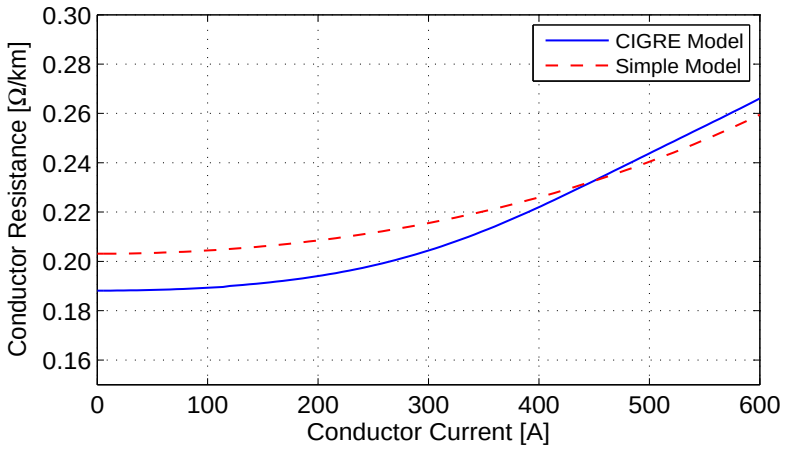

(a)

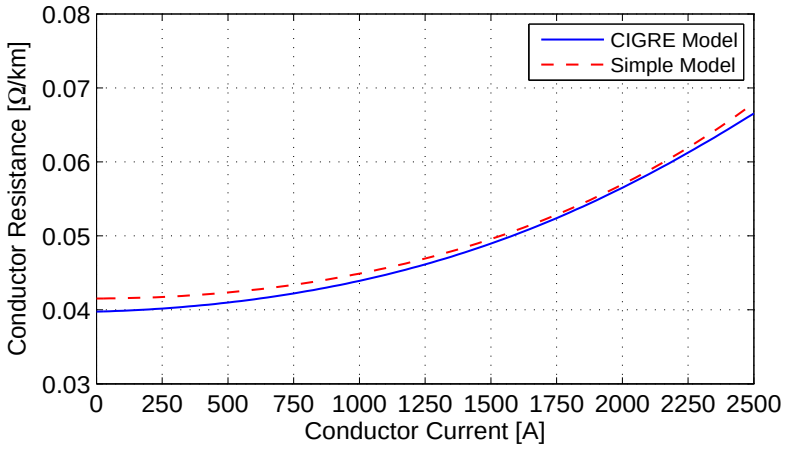

(b)

Fig. 4.9: Comparison of the conductor resistance as calculated using the CIGRE model and as estimated using (4.42) for (a) 160 mm^2 ACSR and (b) 810 mm^2 TACSR conductors.

using (4.41) is rather conservative because the maximum value of the skin effect factor is used. The variation in the skin effect factor is much larger for the two-layered steel-cored conductor, as seen in Fig. 4.3. The results are shown in Fig. 4.9(a).

Typically, when using weather-based line ratings, a number of weather sensors will be placed at various locations on a long transmission line and the collected weather data together with the conductor current data would be fed back to a central energy management system. These data would then be used to estimate conductor temperature and determine the line ratings at the various locations [10]. The most restrictive of these line ratings would then determine the rating of the entire line. A system that utilizes dynamic line ratings will therefore have a large number of monitoring points in the system and the process of computation of conductor temperature and line ratings would be time consuming.

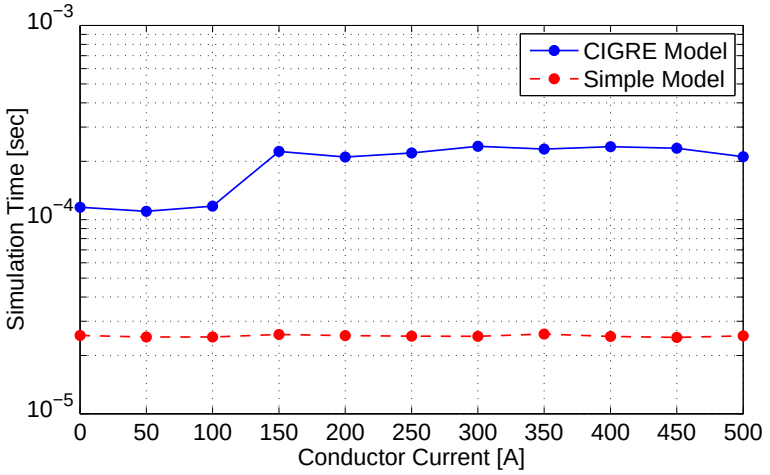

(a)

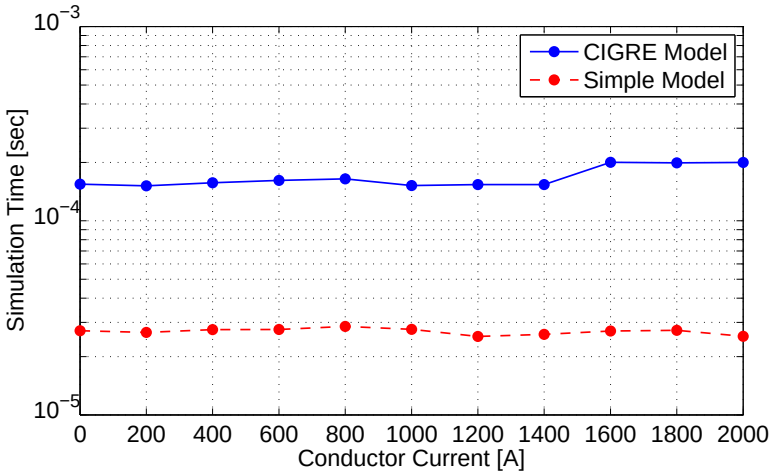

(b)

Fig. 4.10: Comparison of the time required to calculate the conductor temperature using the two models for (a) the 160 mm^2 ACSR conductor, and (b) the 810 mm^2 TACSR conductor.

The main motivation for the model simplification presented in this chapter is thus to reduce the computational effort in determining the temperatures of overhead conductors in large networks so as make it easier to incorporate the thermal dynamics of the conductors into the system operation. This would be especially useful in systems that apply dynamic line ratings, which allow for higher conductor loadability and hence more efficient and economic utilization of transmission networks [10, 11]. The time durations required to run the simulations using the two models are compared in Fig. 4.10. As shown in the figure, there is a significant reduction in the computation time when using the simplified model. Note that a log-axis is used for the simulation time axis in Fig. 4.10, and thus, the CIGRE model takes at least 4.5 times longer than that required by the simplified model to compute conductor temperature.

4.5.2 Transient-state temperature

Based on (4.53), explicit equations for T_c' as a function of time can be written, depending on the nature of the current and weather conditions. Assuming that the weather parameters are constant in the duration $t_0 \leq t \leq t_1$, and that the conductor temperature at t_0 is T_c^0, then for a step input current:

$$T_c'(t) = T_{l1}' - (T_{l1}' - T_c^0)e^{-t/\tau} \tag{4.54}$$

where T_{l1}' is the line temperature at steady-state calculated using (4.48) for the weather conditions during $t_0 \leq t \leq t_1$, and τ is the time constant given by:

$$\tau = \frac{mc}{h_0'} \tag{4.55}$$

Fig. 4.11(a) compares the 160 mm^2 ACSR conductor temperature time response to a step change in current from 300 A to 500 A as predicted by the CIGRE model given by (4.20) and as obtained by (4.54). Fig. 4.11(b) shows a similar result for the 810 mm^2 TACSR with current increasing from 1,600 A to 2,000 A. In both cases, it is assumed that the conductor is in steady-state at $t < 0$ and that the weather conditions are constant during the simulation period, as given in Table 4.2. The results show that (4.54) provides a similar time response to that of the CIGRE model, and the approximation error is less than 1 °C and 3 °C for the ACSR and TACSR conductors, respectively.

The time constants for the two conductors as calculated by (4.55) are 8.5 min and 20.8 min for the 160 mm^2 ACSR and 810 mm^2 TACSR conductors, respectively. The time taken for the temperature increase to reach 63.2% of the maximum temperature rise for the CIGRE model curves in Fig. 4.11 were 8.3 min and 21.5 min, respectively, which confirms that the step response equation (4.54) effectively captures the transient response (rate of temperature change) characteristics of the conductors.

It is noted that discretization of the CIGRE model is required to obtain the CIGRE plots of Fig. 4.11 as seen from (4.20). Starting from an initial value for the conductor temperature, T_c is iteratively re-evaluated after every time step to determine the temperature. The chosen time step must be small (1 s was used in the plots of Fig. 4.11) to obtain accurate results. However, in the case of the simple model, (4.54) is an explicit equation

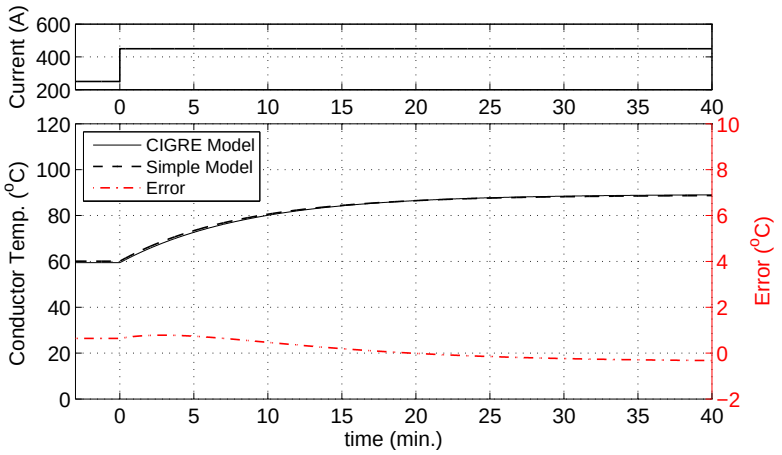

(a)

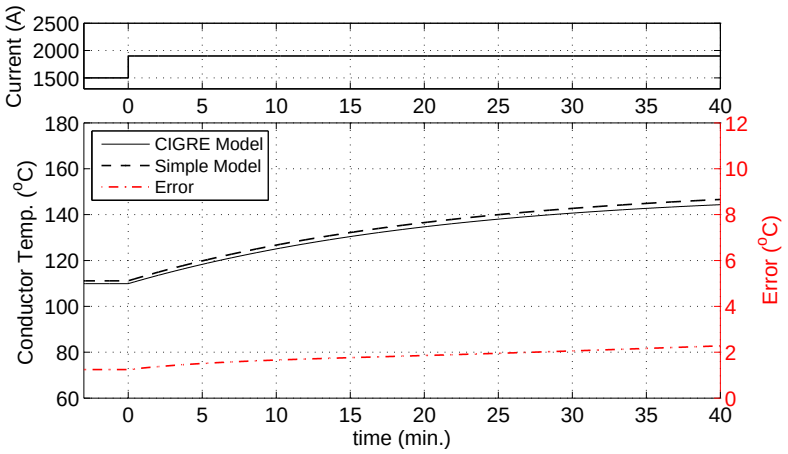

(b)

Fig. 4.11: Conductor temperature time response to a step change in the current (a) from 250 A to 450 A for the 160 mm^2 ACSR conductor, and (b) from 1,500 A to 1,900 A for the 810 mm^2 TACSR conductor.

of time, which requires only the determination of the constants to directly determine the temporal evolution of T_c'.

4.6 Experimental validation

In addition to the mathematical validation of the proposed simplified conductor temperature model detailed in Section 4.5, a laboratory based experimental validation was also carried out and the details are discussed in this section. The temperature of an overhead conductor typically used in the Japanese network (e.g. at the 66 kV level) was measured in a wind tunnel environment under different magnitudes of conductor current and ambient wind speeds. As discussed here, a comparison of measured conductor temperature values (for both steady-state and transient-state conditions) with values estimated using the proposed simplified version of the CIGRE model confirms the validity of the proposed simplified model.

4.6.1 Experimental set up

The experiment was carried out in a wind tunnel experiment equipment at a Sumitomo Electric Industries Limited laboratory in Hitachi City, Ibaraki, Japan. A 160 mm^2 ACSR conductor (about 2.5 meters in length) was placed in the wind tunnel as shown in Figs. 4.12 and 4.13. The conductor temperature was recorded under different magnitudes of current and wind speeds.

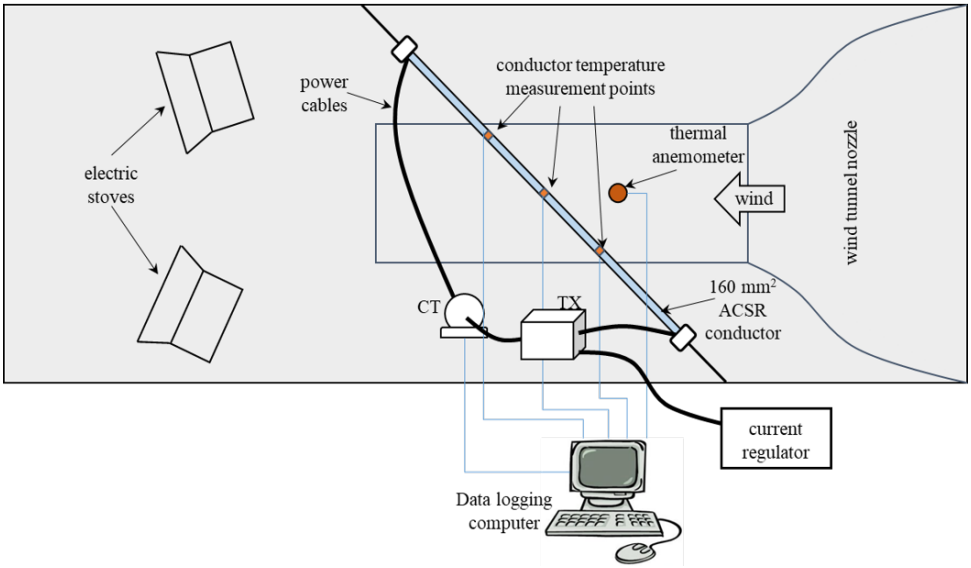

Fig. 4.12: Experimental set-up in wind tunnel

The current was supplied through a 50 Hz transformer and measured with a 500:1 current transformer. A photo of the voltage transformer and the current transformer is shown in Fig. 4.14(a). The current regulator equipment is shown in Fig. 4.14(b). The wind speeds applied to the conductor were 0.5 m/s, 2 m/s, and 5 m/s. Wind speed and ambient air temperature was monitored using a portable thermal anemometer and logged every 5 seconds. The CT and conductor current was also logged at 5 second intervals. The conductor temperature was monitored by attaching thermocouples at three points along the conductor surface. Conductor temperature and room temperature was logged at 10 second intervals. The conductor was placed at an angle of 45° to the wind direction throughout the experiment as shown in Fig. 4.12. The conductor placement in the wind tunnel outlet is shown in Fig. 4.15.

4.6.2 Experimental results

Conductor temperature (both steady-state and transient-state) was monitored for various current and weather conditions. The measured conductor thermal responses were then compared to calculated values using both the CIGRE and simplified models. The results, plotted in Fig. 4.16, show that the measured transient response of conductor temperature is well matched to the response calculated from both the CIGRE model and the simplified model.

Fig. 4.17 shows the measured *steady-state* conductor temperature against current and

Fig. 4.13: Photograph of experimental set-up inside wind tunnel

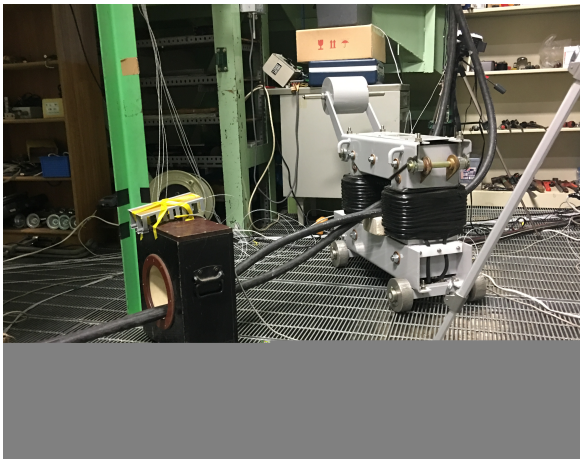

(a)

(b)

Fig. 4.14: Experimental equipment: (a) voltage transformer and current transformer and (b) current regulator

Fig. 4.15: Conductor placement in wind tunnel outlet

the values calculated from the full CIGRE model and the simplified model. Fig. 4.17 shows a good correlation between measured and calculated values though the measured values are slightly higher for low wind speeds (0.5 m/s and 2.0 m/s) which is also noted in Fig. 4.16. This difference could be explained by both model and experimental errors. Reference [15] reports errors between measured and calculated values of similar magnitudes. Though the experimental errors could be due to errors in the original CIGRE model from which the simplified model is derived, they may also be due to the radiative heating effect of the electric stove that is not captured by the mathematical models. The heat balance equation (4.18) implies that, at low wind speeds, radiative cooling has a significant effect on the steady-state temperature since it is comparable in magnitude to the convective cooling effect. Heating by the electric stove introduces an opposite radiative heating which has the effect of raising the conductor temperature thereby explaining why the measured steady-state conductor temperature values shown in Fig. 4.17 are higher than the model calculated values. At higher wind speeds (e.g. 5 m/s in Fig. 4.17), the convective cooling effect is much larger than the radiative cooling effect hence the effect of conductor heating by the electric stove is negligible. The measured and calculated values of steady-state temperature are therefore very well matched.

Table 4.3 compares the average values of thermal time constants for the transient response measured during transition from one set of experimental settings to the next. For the measurements and the full CIGRE model, the thermal time constant is estimated as the duration taken for the conductor temperature to change 63.1% from one steady-state value to the next. Table. 4.3 shows that the proposed simplified model gives lower

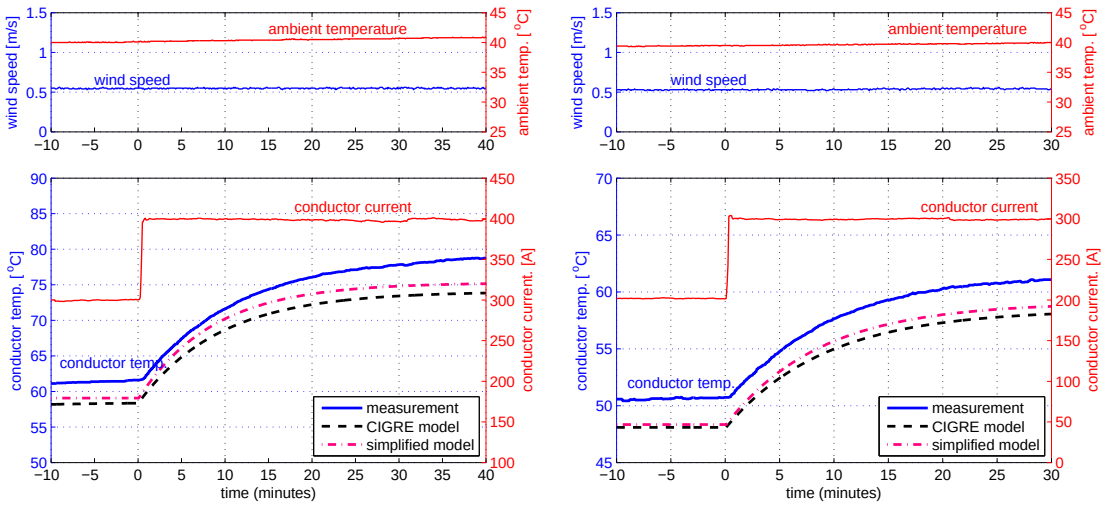

(a)

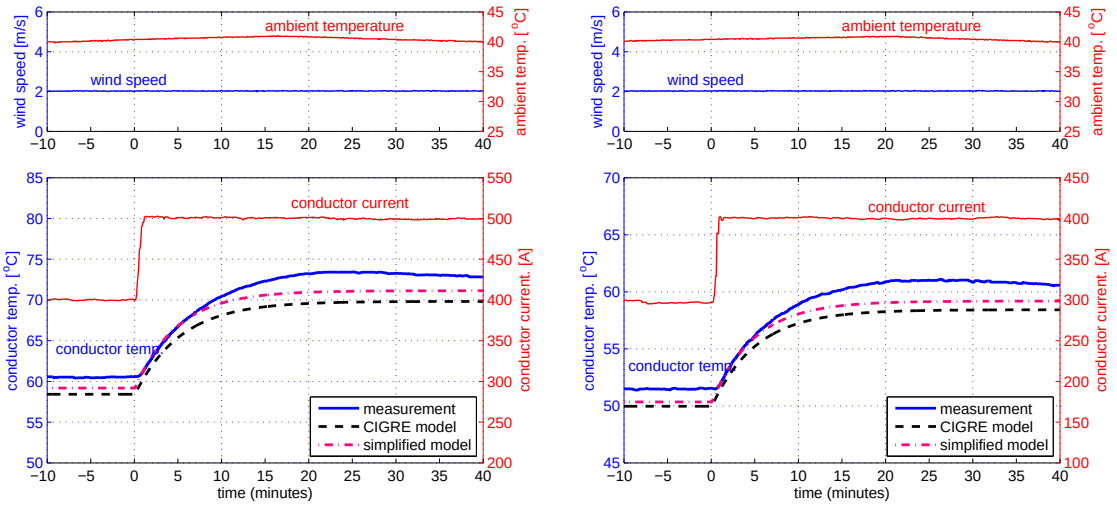

(b)

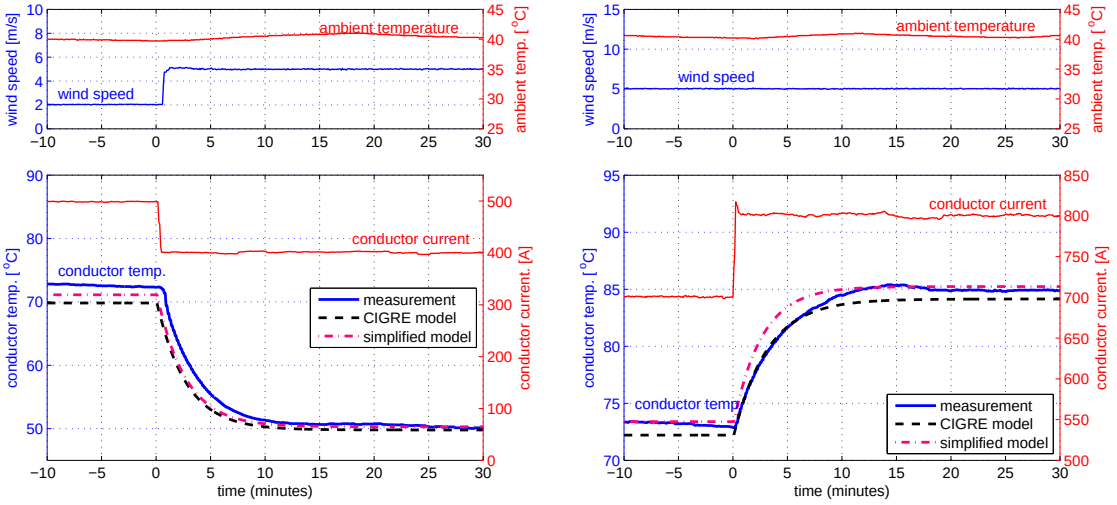

(c)

Fig. 4.16: Conductor temperature thermal transient response curves for various current and weather conditions: (a) 0.5 m/s wind speed, (b) 2.0 m/s wind speed, and (c) 5.0 m/s wind speed.

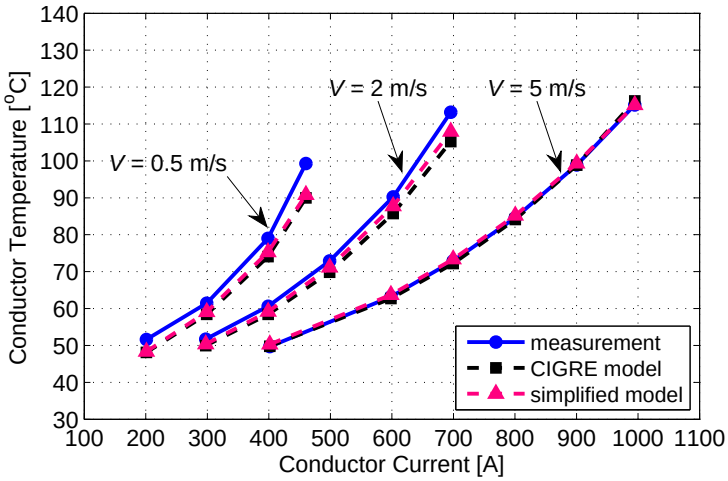

Fig. 4.17: Comparison of measured and calculated steady-state conductor temperature

Table 4.3: Comparison of thermal response time constants

Wind Speed	Time constant (minutes)		
m/s	Measurement	CIGRE model	Simplified model
0.5	12.4	9.4	8.7
2.0	7.2	5.3	4.9
5.0	4.3	3.1	2.6

thermal time constants. This is because the simplified model was developed from a slightly conservative point of view resulting in faster conductor temperature rise values during current transients [26].

4.7 Model application areas

Dynamic line ratings are premised on the idea that, by monitoring ambient weather conditions around a conductor, it is possible to relax the conservative approach taken when a static line rating is applied. The information on the degree of conductor heating and cooling obtained from the monitored ambient weather conditions can be used to increase the loadability of the line thus effectively extending the usage capability. This is especially so during favorable weather conditions such as periods of high prevailing wind speeds.

The mathematical model presented in this chapter provides a simple way of integrating conductor thermal dynamics in networks that apply DLR systems. The model simplifies the conductor thermal equation hence providing a method of estimating overhead conductor temperature without the need of iterative calculations. It gives a fast and relatively accurate way of estimating the thermal status of overhead conductors using monitored ambient weather conditions as inputs. Two specific possible application areas described next:

Extension of the optimal power flow (OPF) formulation with explicit conductor temperature limits

The OPF problem is typically formulated with maximum line current or power limits which are typically SLR values. In a network that applies DLRs, the conductor thermal equation could replace the traditional flow limits in the OPF formulation – using a maximum conductor temperature limit rather than maximum current/power. Instead of using the full CIGRE model, the proposed model which gives a simple equation relating conductor current to conductor temperature can be applied. The result is that the complexity of the OPF problem is not significantly altered.

The proposed steady-state equation is easily differentiable meaning that an extension of traditional OPF formulation is simple. The convex quadratic equations also alleviate any convergence issues that may result from the nonlinear CIGRE model equations. The proposed model therefore allows for computation time savings in the OPF solution during the determination of conductor temperature using monitored ambient weather data as inputs.

Application in system security analysis

With DLRs, an overload during a contingency is defined as a conductor having its temperature exceed the maximum allowable temperature after the occurrence of the contingency. However, because of the conductor thermal inertia effect illustrated by the transient response characteristics shown in Fig. 4.16, it takes a few minutes for the conductor temperature to rise from its initial value after an increase in conductor current. The system operator therefore has a few minutes to alter the system operating points so as to address the effects of the contingency giving a form of post-contingency corrective control.

The time available for the application of corrective measures could be defined using a *time-to-overload* index [27] that would correlate with the severity of the contingency and form a basis for contingency ranking. In a system with hundreds or thousands of lines, the proposed model provides a very fast method of carrying out such security analysis and subsequently developing algorithms for contingency response plans.

4.8 Summary

A simple mathematical model that can be used to estimate the temperature of an overhead conductor from the current flowing through the conductor and the ambient weather conditions has been presented in this chapter. The simplified model is derived from approximations of the various components of the CIGRE model for calculating the temperature [1]. The main contributions of this chapter can be summarized as follows:

1. A step-by-step description of the derivation of the simplified model is given. The result is an explicit equation that gives the steady-state conductor temperature as a quadratic function of the square of the current with the polynomial constants dependent on ambient weather conditions and conductor resistance. In the transient-state, a first-order ODE was derived from which equations describing the conductor tem-

perature as functions of time can be derived depending on changes in the conductor current and/or weather parameters.

2. The validity of the simplified model was tested mathematically using two conductors typically used in the Japanese transmission network. Simulations for the two conductors show that the approximation errors in the simplified model are within 3 °C of the values obtained from the full CIGRE model in both the steady and transient states. The approximated values of the conductor resistance and transient response time constant are also very close to those obtained by the full CIGRE model.
3. An experimental validation of the proposed model is also carried out. Results of the experiments carried out in a wind tunnel environment show a good agreement between measured and calculated values of conductor temperature in both steady-state and transient-state.
4. The simplified model is shown to significantly reduce computational effort and computation time in the estimation of conductor temperature. The time required to arrive at a solution for a single calculation using the CIGRE model is found to be at least 4.5 times longer than the time required by the simplified model.

The model presented in this chapter is intended to simplify the explicit use of the thermal characteristics of the overhead conductors in network management systems, such as in the solutions to real-time optimal power flow problems, system security analysis, and development of post contingency corrective control algorithms.

4.9 References

[1] CIGRE Working Group 22.12, "Thermal behaviour of overhead conductors," August 2002. CIGRE Technical Brochure, Available from: https://e-cigre.org/publication/207-thermal-behaviour-of-overhead-conductors.

[2] Y. Ueda, K. Kurokawa, T. Tanabe, K. Kitamura, and H. Sugihara, "Analysis results of output power loss due to the grid voltage rise in grid-connected photovoltaic power generation systems," *Industrial Electronics, IEEE Transactions on*, vol. 55, no. 7, pp. 2744–2751, 2008. doi: https://doi.org/10.1109/TIE.2008.924447.

[3] P. Denholm and M. Hand, "Grid flexibility and storage required to achieve very high penetration of variable renewable electricity," *Energy Policy*, vol. 39, no. 3, pp. 1817 – 1830, 2011. doi: https://doi.org/10.1016/j.enpol.2011.01.019.

[4] D. Cheng, B. A. Mather, R. Seguin, J. Hambrick, and R. P. Broadwater, "Photovoltaic (PV) impact assessment for very high penetration levels," *IEEE Journal of Photovoltaics*, vol. 6, pp. 295–300, Jan 2016. doi: https://doi.org/10.1109/JPHOTOV.2015.2481605.

[5] B. Xu, A. Ulbig, and G. Andersson, "Impacts of dynamic line rating on power dispatch performance and grid integration of renewable energy sources," in *IEEE PES ISGT*

Europe 2013, pp. 1–5, Oct 2013. doi: https://doi.org/10.1109/ISGTEurope.2013.6695410.

[6] S. D. Foss and R. A. Maraio, "Dynamic line rating in the operating environment," *IEEE Transactions on Power Delivery*, vol. 5, pp. 1095–1105, Apr 1990. doi: https://doi.org/10.1109/61.53127.

[7] D. A. Douglass, "Weather-dependent versus static thermal line ratings [power overhead lines]," *IEEE Transactions on Power Delivery*, vol. 3, pp. 742–753, Apr 1988. doi: https://doi.org/10.1109/61.4313.

[8] J. R. Santos, A. G. Exposito, and F. P. Sanchez, "Assessment of conductor thermal models for grid studies," *IET Generation, Transmission Distribution*, vol. 1, no. 1, pp. 155–161, 2007. doi: https://doi.org/10.1049/iet-gtd:20050472.

[9] T. Krontiris, A. Wasserrab, and G. Balzer, "Weather-based loading of overhead lines - consideration of conductor's heat capacity," in *2010 Modern Electric Power Systems*, pp. 1–8, Sept 2010. Available from: https://ieeexplore.ieee.org/iel5/5996359/6007154/06007162.pdf.

[10] K. W. Cheung and J. Wu, "Enhancement of real-time operational efficiency by applying dynamic line ratings," in *Proceedings of the 2016 IEEE PES Asia-Pacific Power and Energy Conference, Xi'an, China*, pp. 103–107, Nov 2016. doi: https://doi.org/10.1109/APPEEC.2016.7779477.

[11] J. Heckenbergerová and J. Hošek, "Dynamic thermal rating of power transmission lines related to wind energy integration," in *2012 11th International Conference on Environment and Electrical Engineering*, pp. 798–801, May 2012. doi: https://doi.org/10.1109/EEEIC.2012.6221484.

[12] S. Talpur, C. J. Wallnerström, P. Hilber, and S. N. Saqib, "Implementation of dynamic line rating technique in a 130 kv regional network," in *Multi-Topic Conference (INMIC), 2014 IEEE 17th International*, pp. 477–482, Dec 2014. doi: https://doi.org/10.1109/INMIC.2014.7097387.

[13] H. Banakar, N. Alguacil, and F. D. Galiana, "Electrothermal coordination part I: theory and implementation schemes," *IEEE Transactions on Power Systems*, vol. 20, pp. 798–805, May 2005. doi: https://doi.org/10.1109/TPWRS.2005.846196.

[14] N. Alguacil, M. H. Banakar, and F. D. Galiana, "Electrothermal coordination part II: case studies," *IEEE Transactions on Power Systems*, vol. 20, pp. 1738–1745, Nov 2005. doi: https://doi.org/10.1109/TPWRS.2005.857836.

[15] D. J. Morrow, J. Fu, and S. M. Abdelkader, "Experimentally validated partial least squares model for dynamic line rating," *IET Renewable Power Generation*, vol. 8, no. 3, pp. 260–268, 2014. doi: https://doi.org/10.1049/iet-rpg.2013.0097.

[16] K. Adomah, Y. Mizuno, and K. Naito, "Probabilistic assessment of the sag in an overhead transmission line," *IEEJ Transactions on Power and Energy*, vol. 120, no. 10, pp. 1298–1303, 2000. doi: https://doi.org/10.1541/ieejpes1990.120.10_1298.

[17] S. M. Mahajan and U. M. Singareddy, "A real-time conductor sag measurement system using a differential GPS," *Power Delivery, IEEE Transactions on*, vol. 27, no. 2, pp. 475–480, 2012. doi: https://doi.org/10.1109/TPWRD.2011.2181963.

[18] I. Albizu, E. Fernandez, P. Eguia, E. Torres, and A. J. Mazón, "Tension and ampacity monitoring system for overhead lines," *Power Delivery, IEEE Transactions on*, vol. 28, no. 1, pp. 3–10, 2013. doi: https://doi.org/10.1109/TPWRD.2012.2213308.

[19] "IEEE standard for calculating the current-temperature relationship of bare overhead conductors," *IEEE Std 738-2012 (Revision of IEEE Std 738-2006 - Incorporates IEEE Std 738-2012 Cor 1-2013)*, pp. 1–72, Dec 2013. doi: https://doi.org/10.1109/IEEESTD.2013.6692858.

[20] M. Akihiko, N. Masahiro, U. Katsuyuki, S. Akihide, O. Osamu, T. Naoto, W. Toshio, K. Toshinori, M. Hiroshi, I. Yoshito, U. Hidetosi, and M. Yuichi, "Experiment about property of heat loss from conductor," in *Proceedings of the 2001 Convention of the Institute of Electrical Engineers of Japan, Nagoya, Japan*, pp. 2837–2838, March 2001.

[21] V. T. Morgan, "The current distribution, resistance and internal inductance of linear power system conductors—a review of explicit equations," *IEEE Transactions on Power Delivery*, vol. 28, pp. 1252–1262, July 2013. doi: https://doi.org/10.1109/TPWRD.2012.2213617.

[22] "Current capacity of overhead power transmission lines (in Japanese)," *Technical Report of the Institute of Electrical Engineers of Japan*, Dec 1997.

[23] The Aluminum Association, *Aluminum Electrical Conductor Handbook*, 3rd ed., 1989. Available from: http://www.aluminum.org/sites/default/files/AECD%20part1%20compressed.pdf.

[24] Midal Cables, "Overhead Conductor Data Sheets," 2016. Available from: https://www.midalcable.com/sites/default/files/ACSR-metric.PDF.

[25] Southwire Ltd, "Product Catalog," 2016. Available from: https://www.southwire.com/ProductCatalog/XTEInterfaceServlet?contentKey=prodcatsheet21.

[26] B. Ngoko, H. Sugihara, and T. Funaki, "Validation of a simplified model for estimating overhead conductor temperatures under dynamic line ratings," *IEEJ Transactions on Power and Energy*, vol. 138, no. 4, pp. 284–296, 2018. doi: https://doi.org/10.1541/ieejpes.138.284.

[27] P. Patowary and N. K. Goyal, "Dynamic thermal rating and allowable operating time under transient conditions," in *2014 Eighteenth National Power Systems Conference (NPSC)*, pp. 1–6, Dec 2014. doi: https://doi.org/10.1109/NPSC.2014.7103881.

CHAPTER 5

Thermal rating of overhead transmission lines

5.1 Introduction

This chapter discusses various concepts concerning the thermal rating of overhead transmission lines. The rating of a transmission line (current or power carrying capacity) can have a considerable effect on power flow within a transmission network. And, with increased uncertainty and variability in line flows due to IRE sources, a more flexible operation of the transmission line with respect to the line rating can have a positive impact on IRE power utilization. Conversely, a conservative approach towards line rating can have negative impacts including excessive IRE output curtailment or increased operational costs to cover for the increased uncertainty [1, 2].

In this chapter, first, the concept of a steady-state thermal rating is discussed. These are the traditional and conservative static line rating (SLR) and the more flexible dynamic line rating (DLR) [3]. Then, two extensions to the two ratings are proposed. The first extension, presented in [4], is a short-term transient rating termed the *dynamic electro-thermal rating (DETR)* which incorporates both the conductor thermal dynamics and changes in ambient weather conditions in its calculation. In this way, DETR is able to include the conductor's thermal inertia characteristics in the determination of maximum allowable current and consequently result in loadability limits that are less conservative than both the DLR and SLR. Simulation results are presented which show that the DETR would allow for higher fluctuations in conductor current as compared to the DLR and can therefore be especially useful for conductors that experience large power fluctuations due to increased IRE sources in the network.

In the second extension, a methodology for the determination of safety factors to be applied in the calculation of DLR in order to ensure safe operation of transmission lines is proposed [5]. While DLR results in increased loadability of transmission lines during weather conditions that are favorable for conductor cooling, there are concerns over perceived increased risk of violating thermal limits if prevailing ambient weather conditions are worse than the forecasted values used to calculate the DLR in real-time. Therefore, it may be necessary to add extra caution on the DLR value in the form of a

safety factor so that the security of the system is guaranteed. Analyses done using real-time weather data show significant increases in line loadability even with the application of the safety factors.

Finally, an assessment of line overload risk in a system with significant IRE generation is illustrated. The risk assessment methodology uses probabilistic models of ambient weather conditions around the transmission lines to determine the probability of violating the maximum conductor temperature limit rather than the traditional maximum conductor current limit. The simplified conductor temperature model detailed in Chapter 4 is used in the risk assessment procedure which results in significant computation time savings.

5.2 Literature review of transmission line thermal ratings

The thermal rating of an overhead conductor refers to the maximum current that the conductor can carry without its temperature exceeding a maximum allowable limit. Here, the maximum allowable limit refers to the conductor temperature that would result either in excessive sag or in significant loss of the conductor's tensile strength [6, 7]. For a given maximum allowable temperature, a conductor's thermal rating is calculated using equations that model the electro-thermal processes of the conductor [8, 9] as described in Chapter 4.

As introduced in Chapter 2, two types of thermal ratings are usually employed for normal operating conditions i.e. the static line rating (SLR) and the dynamic line rating (DLR). The DLR is usually re-calculated after pre-set time durations, say every 30 minutes, varying the values of the weather parameters along the line as the weather changes. DLR usually results in significantly higher line loadability and potentially more economical utilization of transmission networks [7, 10]. This is because prevailing weather conditions are usually considerably better at cooling the conductor than the weather conditions used to calculate the SLR. DLR could be particularly useful as networks become more stressed with increased generation from IRE sources, which increase uncertainties in power network line flows [2, 7, 11].

An aspect of the conductor thermal dynamics that is not captured in the calculation of either the SLR or the DLR is the conductor thermal inertia [12, 13, 14]. This is the characteristic that conductor temperature transients are slower than variations in current. Because changes in conductor temperature are relatively slower than changes in current, large fluctuations in conductor current may not necessarily result in conductor temperatures exceeding maximum temperature limits if the fluctuations last for a short duration of time as could be the case in networks with large amounts of IRE sources, especially where the IRE sources are concentrated over small geographical areas.

The conservativeness in conductor cooling with which SLRs are calculated ensures that the risk of violating thermal limits is reduced to values below certain risk standards set by the system operator. This, coupled with typical N-1 reliability criteria, means that overhead conductors are typically used well below their actual thermal ratings. However,

although the SLR is conservative, it is the most reliable rating system for present power system operators, given its long use in many countries.

The main counterargument against DLRs is that there is a perceived increased risk of violating thermal limits, which is particularly worrisome where line loadability limits are set by minimum ground clearances [15]. The increased risk from DLRs is because meteorological parameters have significant levels of uncertainty, which, if not properly accounted for in determination of the DLR, could result in calculated ampacity values higher than the actual line limits [7]. The use of probabilistic methods to forecast DLRs has been explored by several researchers [16, 17, 18] with such studies focusing mainly on the forecasting of ambient weather conditions across the transmission lines in weather based DLR systems.

5.3 Steady-state transmission line ratings

5.3.1 Static and dynamic line ratings

Referring to the steady-state heat balance equation (4.18), by making current I_c the subject of the formula, the steady-state current rating of a transmission line I^{ss}_{max} is obtained from:

$$I^{ss}_{max} = \sqrt{\frac{P_C(T_{l,max}) + P_R(T_{l,max}) - P_S}{R_{ac}(T_{l,max})}} \qquad \text{[A]} \tag{5.1}$$

where $T_{l,max}$ is the maximum allowable conductor temperature.

I^{ss}_{max} will be referred to as the *static line rating* (SLR) if a set of conservative, worst-case weather conditions are used to calculate the line rating. The conservative approach ensures that the probability of conductor temperatures reaching the maximum allowed values are very low even if the conductor continuously carries the SLR current. The standard values of weather parameters used to calculate the SLR in Japan were given in Table 4.2.

If, on the other hand, the prevailing real-time weather conditions are used to calculate the line rating, then I^{ss}_{max} will be the *dynamic line rating* (DLR). The DLR is re-calculated after pre-set time durations, say every 30 minutes, varying the values of the weather parameters along the line as the weather changes. The DLR is therefore more flexible and usually less conservative than the SLR though it requires constant monitoring of weather conditions at regular time intervals.

5.3.2 Influence of weather parameters on line rating

Since the components on the RHS of (5.1) are heavily dependent on prevailing weather conditions, the steady-state line rating varies widely depending on the values of the weather parameters. To illustrate the dependence of ampacity on weather parameters, a 160mm^2, 30/7 ACSR conductor whose parameters were given in Table 4.1 is used. Fig. 5.1 shows how the value of ampacity varies with the various weather parameters. For each plot, other than the parameter whose sensitivity is being illustrated, the other parameters are kept constant at their reference values of Table 4.2. Ampacity increases from the static

rating of 471 A for a wind speed of 0.5 m/s to 932 A for a wind speed of 6 m/s (a 98% increase). Ambient temperature and wind angle of attack also have significant effects on ampacity while the effect of global solar radiation is comparatively lower. The influence of each weather parameter on line loadability is summarized in Table 5.1.

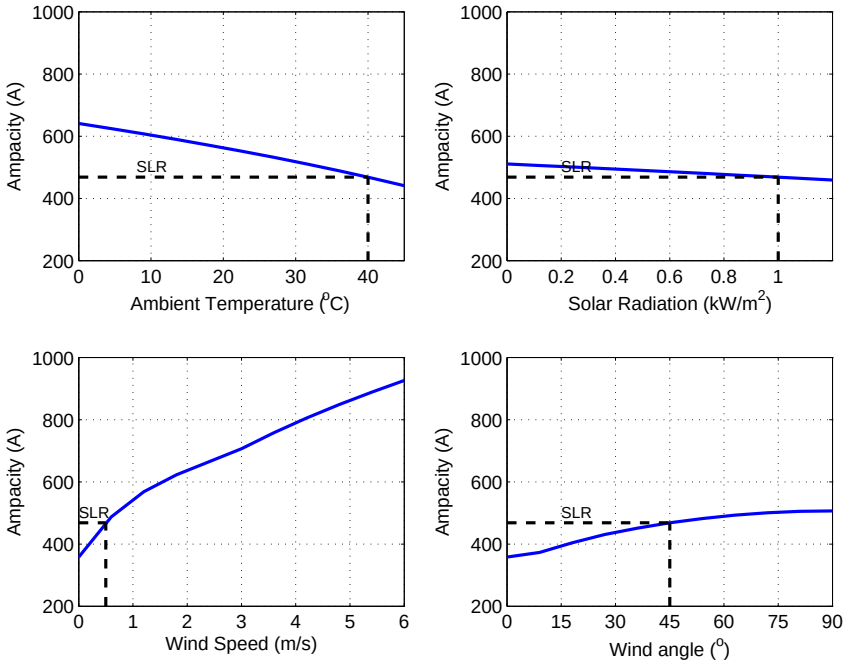

Fig. 5.1: Variation of conductor ampacity with different weather parameters

Table 5.1: Line rating sensitivity to changes in ambient weather conditions

Parameter	Range	Line rating sensitivity	
		per unit	maximum effect
ambient temperature	+40°C to −20°C	+0.8% per −1°C	48%
solar radiation	1 kW/m^2 to 0 kW/m^2	+0.8% per −0.1 kW/m^2	8%
wind speed	0 m/s to 15 m/s	+14% per +1m/s	210%
wind direction	0° to 90°	+0.5% per +1°	45%

5.4 Dynamic electrothermal rating

One way of incorporating conductor thermal inertia in determining loadability is to use temperature explicitly to set line flow limits as proposed in [12, 13]. Alternatively, the thermal inertia effect could be directly included in the determination of ampacity. In this section, the latter approach is illustrated by introducing a short-term dynamic thermal rating, referred to as the dynamic electro-thermal rating (DETR), that would incorporate the conductor thermal inertia characteristic in its calculation.

5.4.1 Concept of transient-state rating

Both the SLR and DLR are calculated for steady-state conditions. However, in conductors which experience large fluctuations in current, conductor temperature may not necessarily reach the steady-state values predicted by the current for short-duration fluctuations because of the thermal inertia effect. Fig. 5.2 shows the conductor temperature time response to a step change in current from 400 A to 600 A as determined by the CIGRE model for the weather conditions: $T_a = 25°C$, $V = 0.5$ m/s, $\delta = 45°$, $S = 1$ kW/m^2, and $\rho_r = 1$. The value of 25°C for ambient temperature is more realistic than the 40°C used to calculate the SLR. This is also the value that is typically used to set the SLR during winter in Japan.

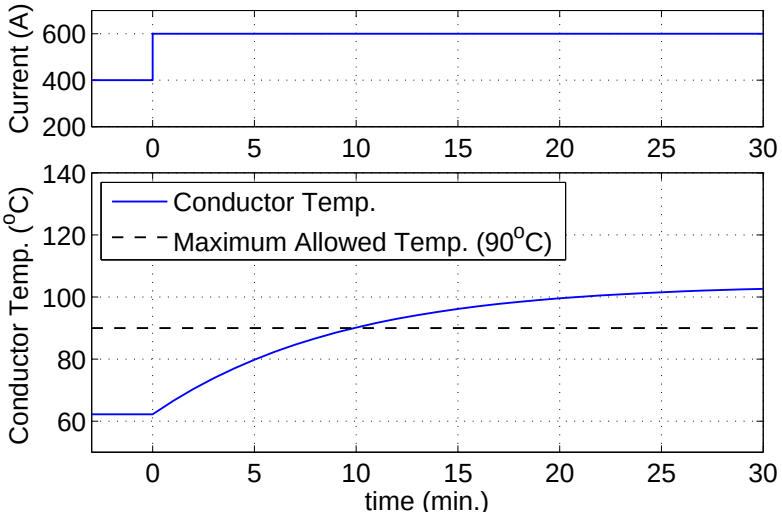

Fig. 5.2: Conductor temperature thermal response to a step change in current from 400 A to 600 A

The DLR corresponding to the simulation conditions in Fig. 5.2 is 544 A. The final conductor temperature of 600 A in Fig. 5.2 is therefore higher than the DLR. However, it takes 10 minutes for conductor temperature to rise and surpass the maximum set value of 90°C. Therefore, if the 600 A current was sustained for less than 10 minutes, there would be no danger of the conductor temperature exceeding the set thermal rating – an illustration of the conductor thermal inertia effect. The overhead conductor thermal inertia effect can be used to allow for loading levels higher than those set by traditional ampacity settings – whether static or dynamic.

Therefore, a short-term ampacity setting, hereinafter referred to as the dynamic electrothermal rating (DETR), is proposed. DETR is defined as the current that, if sustained for a given duration t_d on a conductor initially carrying a current I_0 at steady-state, results in the conductor temperature rising to the maximum allowable value at the end of the specified duration. A step increase in current due to fluctuation in the output of IRE sources represents the worst case scenario in terms of the effect on increase in conductor temperature. Thus, if the DETR is defined based on a step-change in current, then it would in effect be able to cater for any other less severe types of variation in conductor current.

Once again, consider the conductor whose characteristics are specified in Table 4.1 initially carrying 300 A at steady-state with the weather conditions given as: $T_a = 25°C$, $V = 0.5$ m/s, $\delta = 45°$, $S = 1$ kW/m^2, and $\rho_r = 1$. The initial conductor temperature is then calculated as 49°C. A step change in current would result in the time responses shown in Fig. 5.3 depending on the magnitude of the final current. From this result it is seen that a step current of 746 A results in the temperature increasing to the maximum setting (90°C) after 5 minutes. The 5-min DETR for this conductor would then be 746 A. For these weather conditions, the DLR is calculated as 544 A. The 5-min DETR is thus 37% higher than the DLR. Both values are obviously significantly higher than the SLR of 453 A.

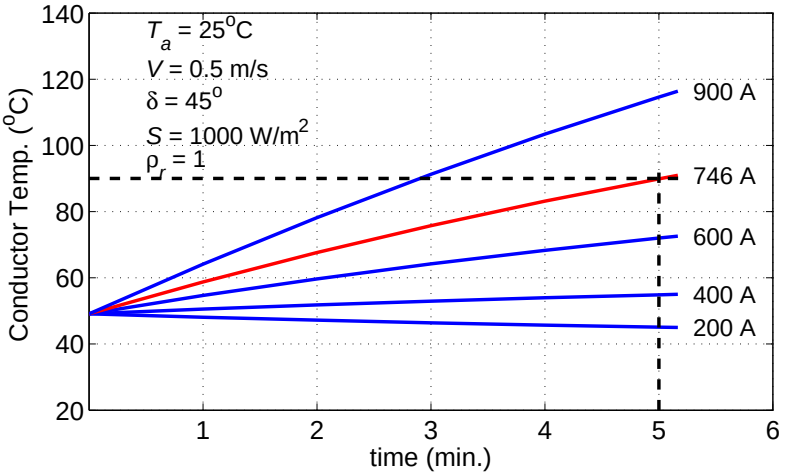

Fig. 5.3: Conductor temperature step-response to different values of current over a 5-min period.

Using the CIGRE model for conductor temperature [8], an iterative algorithm is used to determine the DETR (I_{max}^{detr}). The algorithm, which takes the weather conditions, initial current I_0, and DETR time-step t_d as inputs, is technically a line search on the magnitude of step current that results in conductor temperature reaching the maximum allowed temperature in a given duration t_d. The value of the DETR obviously depends on the duration considered. Fig. 5.4 shows the 5-min DETR, 10-min DETR, and 15-min DETR as a function of I_0 for different wind speeds (the most important factor in determining ampacity). As seen from the figure, DETR approaches the DLR as the DETR duration increases i.e. approaching steady-state.

Increase of IRE sources in power networks has led to increased fluctuations in current flowing in the network conductors. The magnitude and frequency of fluctuations increase with increase in the share of IRE sources. Because of these fluctuations, short-duration increases in current could be picked up by power system protection equipment as overloads and could cause unnecessary tripping of lines. While these short-lived increases in current could result in current increasing above set ampacity limits, because they might last for a short duration (up to a few minutes), they may not necessarily result in conductor temperature increasing above the thermal limits. The DETR would allow for a better accommodation of such fluctuations.

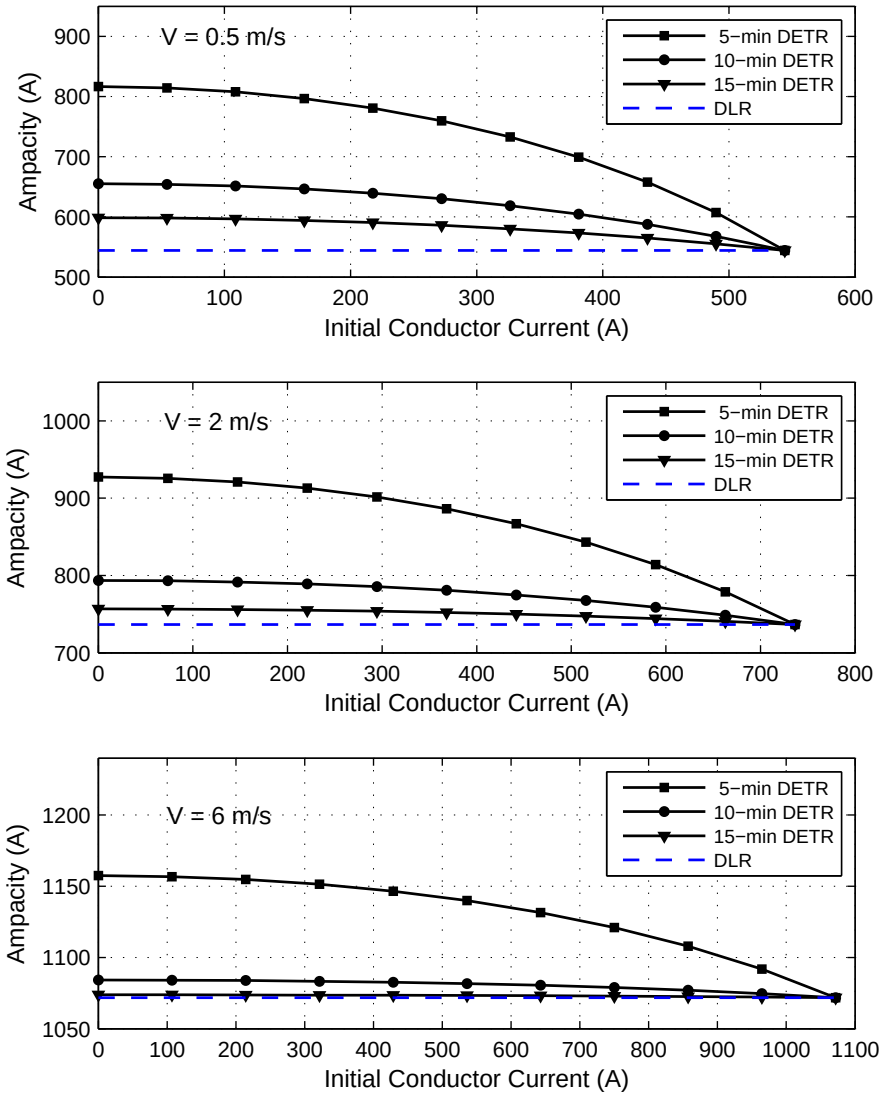

Fig. 5.4: DETRs for different values of wind speed.

5.4.2 Simulation with fluctuating PV generation

The application of DETR in allowing for higher current fluctuations in power lines is illustrated using the simple two-bus system shown in Fig. 5.5.

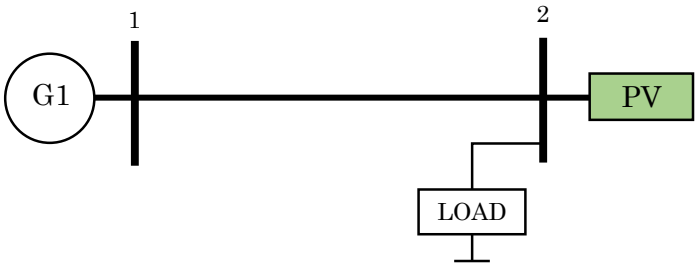

Fig. 5.5: Two bus system with a PV generator at the load bus.

The load at bus 2 is fed by a locally connected large-scale PV system with the deficit supplied from the sending end bus. For simplicity, the load is assumed constant while actual monitored 1-minute global solar irradiation data is used to simulate the power output of the PV system. As the PV system output fluctuates with input irradiation, conductor current also fluctuates. The conductor characteristics are given in Table 4.1 and the weather conditions for the simulation period are assumed constant as: $T_a = 25°\text{C}$, $V = 0.5$ m/s, $\delta = 45°$, $S = 1$ kW/m^2, and $\rho_r = 1$.

The conductor current profile, shown in Fig. 5.6, shows gradually increasing conductor current with three major fluctuations around 14:12, 14:30, and 14:50. Other than the traditional SLR and DLR limits, Fig. 5.6 also shows three DETR limits (5-min DETR, 10-min DETR, and 15-min DETR). The simulation results show that during all three spikes, conductor current exceeds the DLR and in practice would require partial load curtailment to keep the line current within the thermal limits. However, the DETR limits totally or partially allow the current spikes. In the case of the the 5-min DETR, current curtailment would only be required for the third current spike. Generally it is concluded that DETR allows for more fluctuations in current.

The explanation on why DETR allows for the fluctuations is reinforced by the cor-

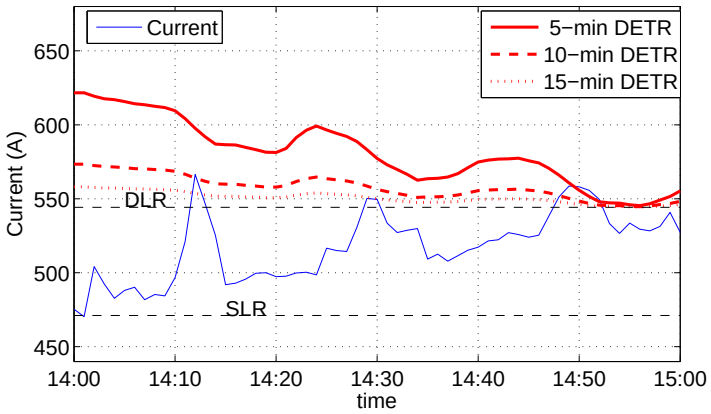

Fig. 5.6: Fluctuating conductor current with various thermal limits.

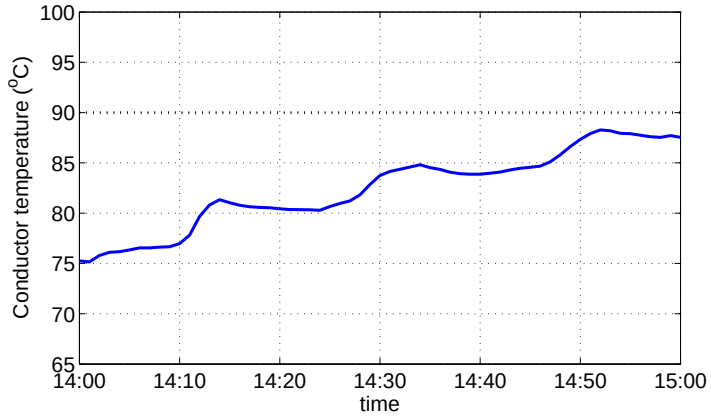

Fig. 5.7: Evolution of conductor temperature for the current fluctuations in Fig. 5.6.

responding plot of conductor temperature shown in Fig. 5.7. The plot shows that, for the first two spikes in current, despite the current magnitude momentarily surpassing the DLR, conductor temperature remains safely below the 90°C limit because of the thermal inertia effect. However, during the third spike, conductor temperature is very close to the limit and hence the DETRs will be essentially equal to the DLR. The necessary current curtailment for the different thermal limits is shown in Fig. 5.8.

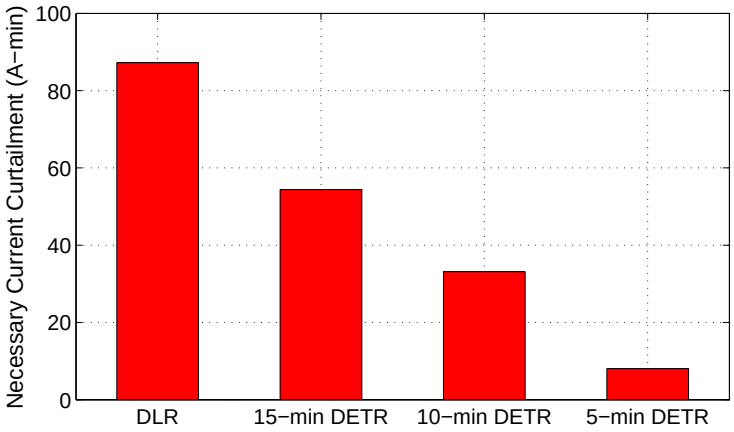

Fig. 5.8: Necessary current curtailment with different thermal limits.

In conclusion, the dynamic electro-thermal rating (DETR) is a short-term thermal rating that incorporates the overhead conductor thermal inertia characteristic in its calculation. Simulation results show that DETR gives higher ratings than the traditional DLR especially when applied for short durations such as 5 or 10 minutes. For this reason, DETR could be especially useful in allowing short duration fluctuations in current as a result of increased integration of IRE sources in power networks.

5.5 Secure transmission line operation with dynamic line ratings

An approach that incorporates DLR-type uncertainties into the conventional SLR criteria can take advantage of the economic benefits of DLRs without increasing the risk of violating thermal limits. Uncertainties can be handled by applying safety factors to forecasted values of real-time DLRs to ensure levels of rating violation risk similar to those achieved by the application of SLR.

In this section, a methodology for the determination of such safety factors based on an analysis of line rating forecasting errors for both steady-state and transient-state ratings is presented. The value of the safety factor applied depends on the certainty with which ambient weather conditions can be forecasted. Simulation results show that a quantitative determination of safety factors based on allowed risk levels can guarantee safe operation of overhead lines while achieving the significant increases in conductor loadability associated with DLRs.

5.5.1 Illustration of operational risk with line ratings

The nature of the operational risks introduced by dynamic line ratings is illustrated here using conductor rating calculations for a typical transmission level conductor and using actual monitored weather data. The characteristics of the 160mm^2 ACSR conductor are given in Table 4.1. The weather data obtained from the Japanese Meteorological Agency (JMA) consists of ambient temperature, wind speed, and solar irradiation data at a temporal resolution of 1 minute for the year 2010. The measurement site is in Osaka, Japan (latitude 34°40.9′N; longitude 135°31.1′E). Fig 5.9 shows one-year profiles of ambient temperature, solar radiation, and wind speed, at a temporal resolution of 5 minutes, averaged from the 1-minute data. In the calculations, a constant wind direction[1] of 45° is assumed. This is because wind direction is a highly variable parameter that is also rather difficult to measure accurately. Also, wind direction meters give only the horizontal direction component, yet wind direction is a three-dimensional vector. In Fig. 5.9, values of the weather parameters used to calculate the SLR are also shown as dotted lines. The SLR is usually a very conservative value intended to ensure a very low probability of violating thermal ratings even if the conductor continuously carries the rated current.

Fig. 5.10 shows the evolution of conductor temperature while continuously carrying the SLR current. It is deduced that, even when continuously carrying the SLR current, the probability of conductor temperature reaching the maximum allowable value (in this case 90°C) is very low. For this data set, there are only 3 instances out of 105,120 (0.0029%) in which the conductor temperature is greater than maximum allowed value, and all of them occur during summer when ambient air temperature and global solar radiation are relatively high.

The less conservative DLR is calculated using prevailing (real-time) weather parameters, which results in higher line loadability during favorable weather conditions and thus a more economical use of the transmission system, especially if implemented on lines operating very near their thermal limits [6].

Using the values of weather parameters and conductor temperature shown in Figs. 5.9 and 5.10, the conductor's DLR is calculated for the entire year and is shown in Fig. 5.11. The SLR current is also shown in Fig. 5.11, which demonstrates that the real-time rating could be up to 3.5 times the SLR. The higher ratings as a result of DLR mean that the conductor could be more heavily loaded during the periods of higher ratings. This could present economic benefits in system operation, including better contingency management and increased utilization of renewable energy sources [7].

5.5.2 Determining safety factors to minimize overload risk

Forecasting of weather conditions

The real-time line rating is calculated ahead of time and the values so obtained are used to determine the operation schedule of the transmission system. However, it is impossible to know the weather conditions ahead of time. The line rating is therefore calculated

[1] Wind direction refers to the acute angle between the direction of the wind and the conductor axis.

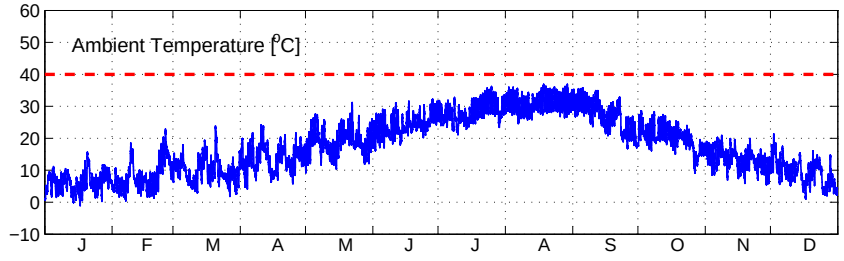

(a)

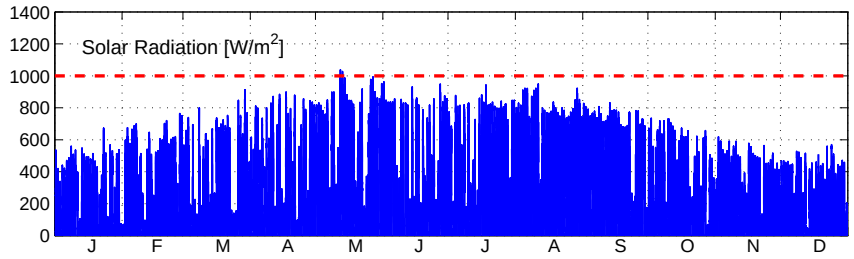

(b)

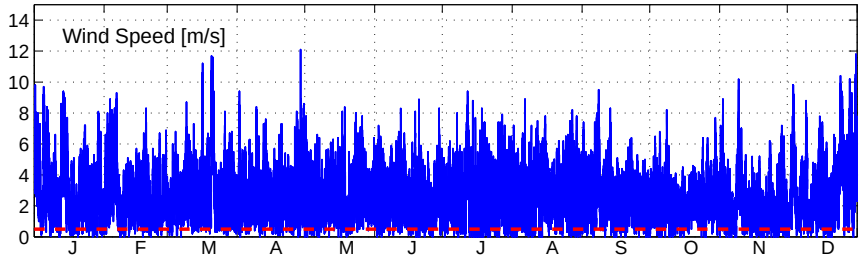

(c)

Fig. 5.9: Year-long profiles of: (a) ambient temperature; (b) solar radiation; and (c) wind speed (5-minute temporal resolution).

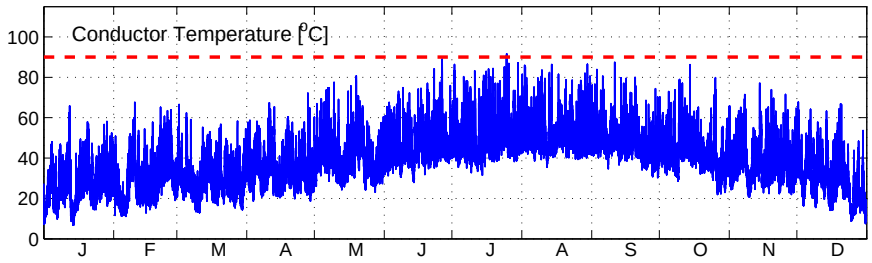

Fig. 5.10: Year-long profile of conductor temperature when continuously carrying the SLR current.

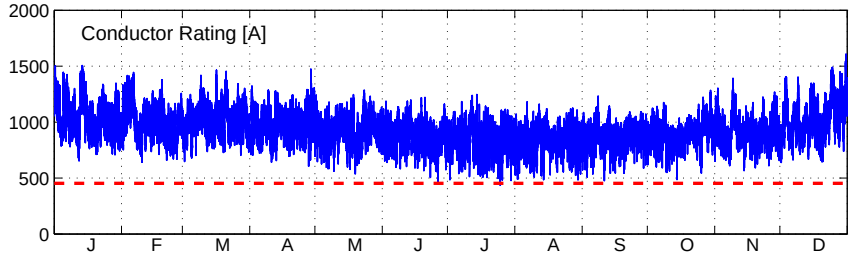

Fig. 5.11: Year-long profile of conductor thermal ratings when continuously carrying the SLR current.

using forecasted values of weather parameters [7]. If it were possible to perfectly forecast ambient weather conditions, the actual line rating as depicted in Fig. 5.11 could be used. However, even very short-term forecasts have a degree of uncertainty.

A very simple model [19] for forecasting the value of a given weather parameter X is adopted here as:

$$E\left[X(t)\right] = \frac{1}{\Delta t} \sum_{t_x=t_0-\Delta t}^{t_0} X(t_x), \qquad t_0 < t < t_0 + \Delta t \tag{5.2}$$

Equation (5.2) means that the expected value of weather parameter X during the forecasting horizon (set as Δt minutes from the last observation) is the average value of X measured over the last Δt minutes. For example, if the average wind speed over the past 5 minutes was 2 m/s, this value is used to calculate the line rating over the next 5 minutes. Similarly, if the average wind speed over the past 30 minutes was 2 m/s, this value is used to calculate the line rating over the next 30 minutes. The rating obtained using forecasted values of weather parameters is termed the forecasted conductor rating, I^f_{max}, and will be different from the actual conductor rating, I_{max}, if the actual values of the weather parameters are different from the forecasted values.

Note that more complicated forecasting models [16, 17, 18, 19] can be used here to achieve better forecasts especially for longer-term forecasting horizons. Such models would include not only temporal fluctuations but also spatial extrapolations when the weather station is located far from the transmission line.

Safety factors for real-time ratings

If the prevailing weather conditions are worse (in terms of conductor cooling) than the forecasted weather conditions, then the forecasted rating will be higher than the actual line rating, and vice versa. A case in which I_{max} is higher than I^f_{max} represents a safe operation of the line, while the case in which I_{max} is lower than I^f_{max} represents a risky operation of the line since it would mean that the actual weather conditions are worse than the forecasted conditions. Hence, if the line current is equal to I^f_{max} during the forecasted period, the conductor temperature will be higher than the maximum allowed temperature.

Figs. 5.12 (a) and (b) show plots of forecasted line ratings against actual line ratings for 5-minute and 30-minute ratings, respectively[2]. The plots also show the line $I^f_{max} = I_{max}$. Points below the line $I^f_{max} = I_{max}$ represent safe operation of the line while points above represent risky operation of the line.

A normalized thermal rating forecasting error κ is defined as:

$$\kappa = \frac{I_{max} - I^f_{max}}{I_{max}} \tag{5.3}$$

A negative value of κ indicates a risky operation of the line, as the actual line rating is lower than the forecasted line rating, while a positive value of κ suggests a safe operation

[2]The thermal time constant of the study conductor ranges from about 2 minutes at high wind speeds to 14 minutes at lower wind speeds so that the 5-minute rating is essentially a transient rating while the 30-minute rating is a steady-state rating. The thermal response characteristics will vary depending on the size and type of conductor.

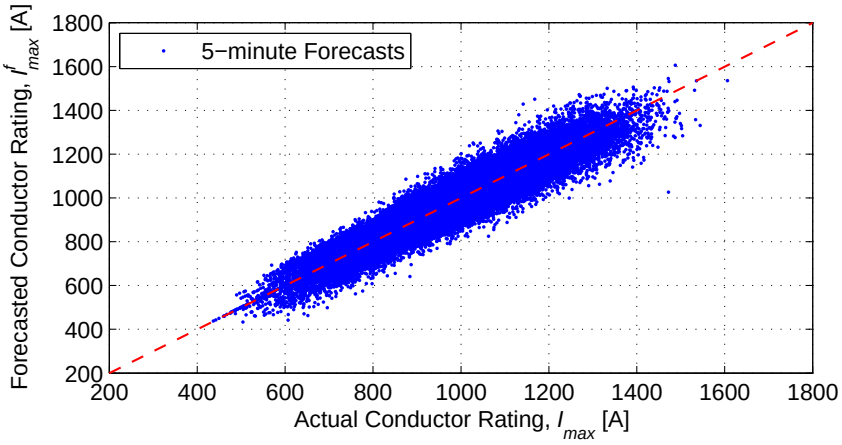

(a)

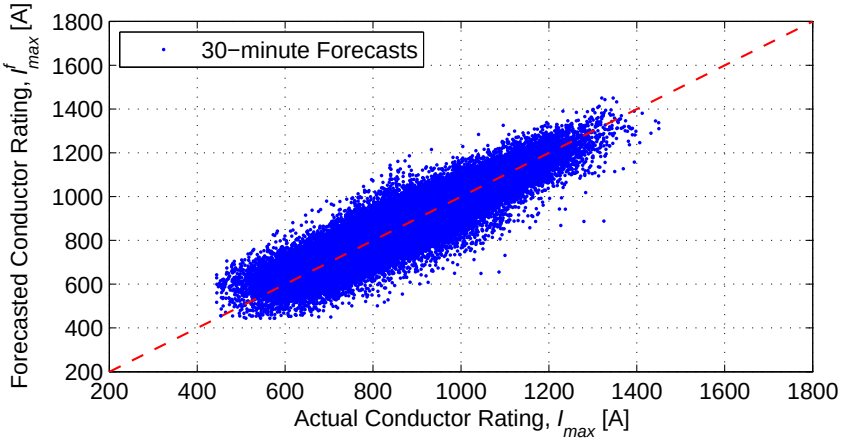

(b)

Fig. 5.12: Forecasted line rating against actual line rating for: (a) 5-minute DLR; and (b) 30-minute DLR.

of the line. The normalized thermal rating forecasting error was calculated for the entire year (for both 5-minute and 30-minute forecasts), and Figs. 5.13(a) and (b) show the probability distributions of κ for the two cases. In Fig. 5.13(a), the 0.1 percentile[3] value of κ for the 5-minute DLR is indicated as $\kappa_{.1\%} = -0.164$. This implies that, for the data set, 99.9% of the time, the normalized rating error is greater than -0.164. This value can be used to determine a safety factor that would ensure that the applied real-time rating is lower than the actual rating 99.9% of the time. The 0.1 percentile value of κ for the 30-minute DLR is indicated in Fig. 5.13(b) as $\kappa_{.1\%} = -0.325$.

For safe operation of the line, the following formula is used to calculate the real-time line rating I^{RT}_{max}:

$$I^{RT}_{max} \quad = \quad \max\left(I_{SLR}\ ,\ \gamma I^{f}_{max}\right) \tag{5.4}$$

where γ is the real-time rating safety factor. From (5.4), if I^f_{max} is lower than I_{SLR}/γ,

[3]The 0.1 percentile value is used here to illustrate a very conservative approach to setting the line rating. Applicable risk levels will depend on the standards adopted by the system operator.

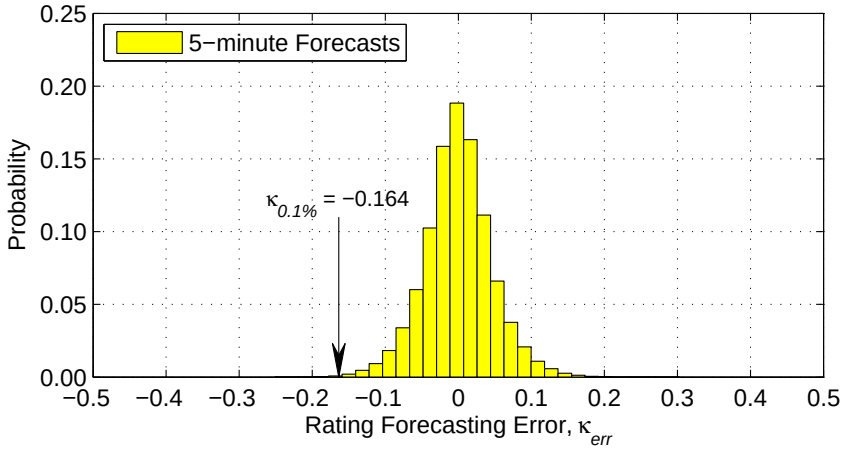

(a)

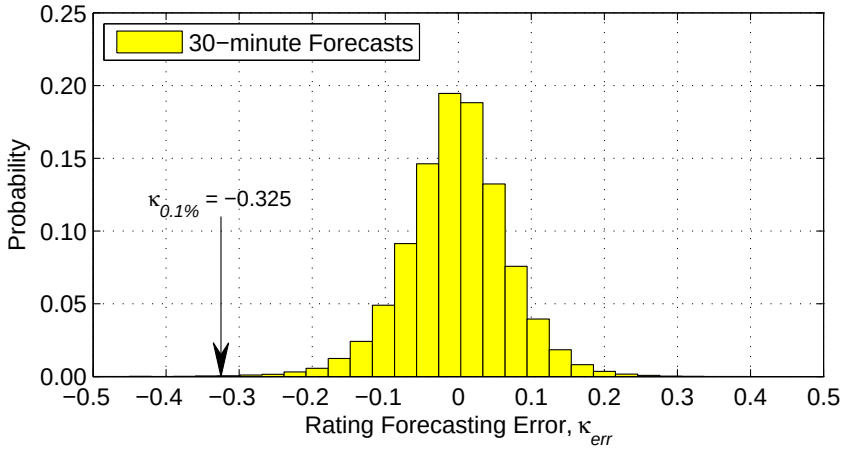

(b)

Fig. 5.13: Probability distribution of normalized rating forecasting error for: (a) 5-minute DLR; and (b) 30-minute DLR.

then the static line rating should be used as the real-time rating; otherwise, the forecasted rating should be multiplied byγ to give I_{max}^{RT}.

In the case where the forecasting errors have been analyzed as depicted in Figs. 5.12 and 5.13, an applicable safety factor is determined by:

$$\gamma = \frac{1}{1 - \kappa_{\beta\%}} \tag{5.5}$$

where $\kappa_{\beta\%}$ is the β percentile value of the normalized rating forecasting error. As an example, using the $\kappa_{.1\%}$ value indicated in Fig. 5.13(a), $\gamma = 1/1.164 = 0.86$. For the 30-minute DLR, $\gamma = 1/1.325 = 0.75$.

5.5.3 Illustrative example

Fig. 5.14 illustrates the application of real-time dynamic line ratings using safety factors. Fig. 5.14(a) shows the evolution of the ambient weather conditions for a 24-hour period (at 5-minute temporal resolution). 5-minute and 30-minute DLRs are calculated using (5.4) and (5.5) updated every 5 minutes. Fig. 5.14(b) shows the two DLRs calculated

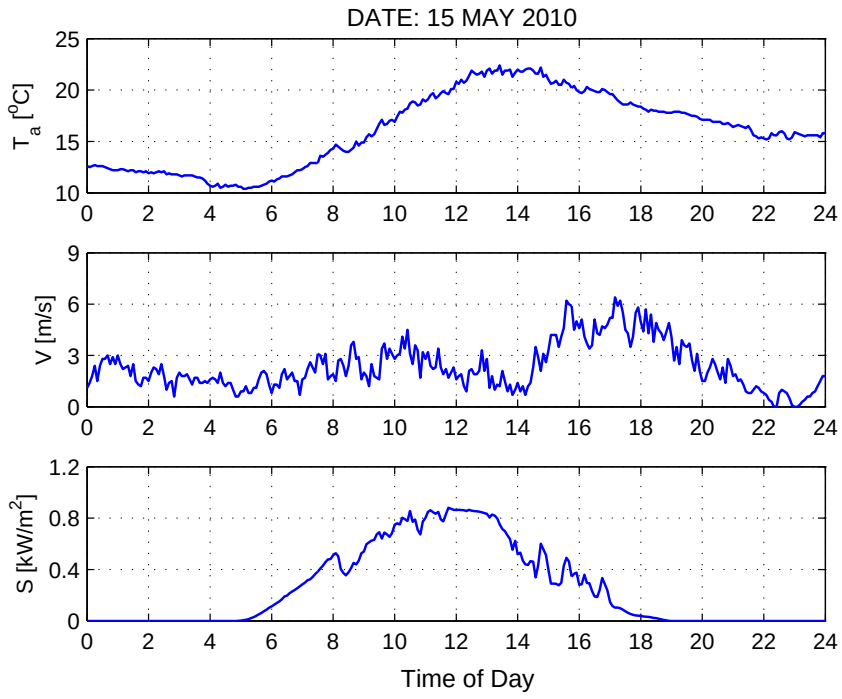

(a)

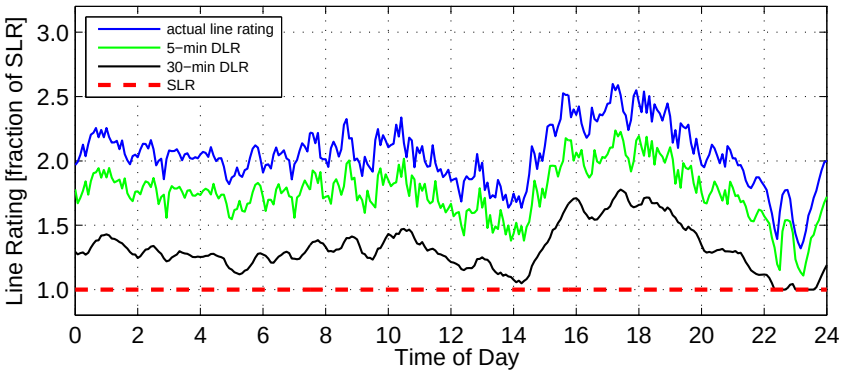

(b)

Fig. 5.14: Illustration of: (a) weather conditions and (b) line ratings for a 24-hour period.

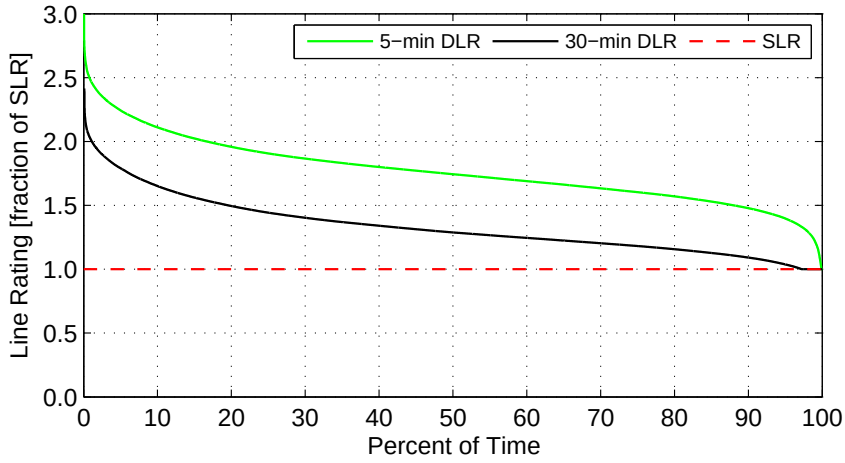

Fig. 5.15: Line rating duration curves showing extra line capacity from DLR.

while applying the safety factor $\gamma = 0.86$ for the 5-minute DLR and $\gamma = 0.75$ for the 30-minute DLR. The actual line rating and the static line ratings are also shown.

The plots of Fig. 5.14 show that application of the safety factors reduces the chances of using a real-time line rating that is higher than the actual line rating. However, the applied line rating is still, in most cases, higher than the static line rating. It is also noted that the 5-minute rating (transient rating) is significantly higher than the 30-minute rating (steady-state rating). This is because of the conductor's thermal inertia, which allows for relatively larger fluctuations in line current.

The extra line capacity resulting from the DLR is quantified for the whole year, and Fig. 5.15 shows the rating duration curves for both the 5-minute and 30-minute DLRs. The area between the DLR and the SLR curves represent the extra available line capacity (EALC) due to DLR. For the data set used in these simulation, the 5-minute DLR results in a 77% increase in line capacity while the 30-minute DLR results in a 33% increase in line capacity at a 0.1% risk level.

5.5.4 Consideration of forecasting uncertainties

The values of the safety factors obtained from (5.5) are a consequence of the uncertainties in the forecasts of weather parameters. The results discussed in this section describe uncertainties due to temporal variations in weather conditions. However, such uncertainties could also be due to [7]:

- spatial variations between the location of the weather station and the relevant transmission line
- errors in measurements of weather parameters and conductor current
- errors in the mathematical model used to estimate conductor temperature.

It is thus noted that an implementation of real-time dynamic line ratings would require a thorough assessment of these uncertainties and relatively accurate monitoring systems so as to minimize any risks that may result from application of such ratings.

5.6 Transmission line overload risk assessment based on a simplified conductor temperature model

The fluctuations inherent in IRE generation leads to increased fluctuations in power flowing through the transmission system. This increased variability increases the risk of transmission line overload i.e. the probability of violating the transmission line's thermal ratings. In this section, an assessment of line overload risk in a system with significant IRE generation is illustrated. The risk assessment methodology uses probabilistic models of ambient weather conditions around the transmission lines to determine the probability of violating the maximum conductor temperature limit rather than the traditional maximum conductor current limit. The application of the simplified conductor temperature model presented in Section 4 in the risk assessment procedure results in significant computation time savings.

5.6.1 Line overload risk assessment procedure

Usually, the transmission line rating is specified as a maximum current (ampacity) value calculated as the steady-state current that would result in the maximum conductor temperature for given ambient weather conditions. The static line rating (SLR) is calculated for worst-case weather conditions while the dynamic line rating (DLR) is calculated for real-time (short-term forecasts) weather conditions [6]. The transmission line overload would then refer to an occurrence in which the conductor current exceeds the pre-defined ampacity. However, conductor manufacturers define the conductor thermal limit as a maximum operating temperature limit rather than an ampacity value. If the ambient weather conditions in which a conductor is operating are monitored, then it is possible to estimate the conductor temperature and therefore determine line overload directly from the temperature value rather than from the current value. Therefore, the risk of transmission line overload is defined here as the probability of the conductor temperature exceeding the maximum allowed value.

This is achieved through Monte Carlo simulations of current flowing through a transmission line with varying ambient weather conditions. Conductor temperature is then calculated for each scenario. The probability distribution of conductor temperature is obtained from the results and the risk of transmission line overload is determined as the percentage of all scenarios in which the conductor temperature exceeds the maximum allowed value.

5.6.2 Illustrative example

The simple two-generator, two-bus test system shown in Fig. 5.16 is used to illustrate the line overload risk assessment. A 230 kV transmission line connects the two buses. The line is constructed using an 810 mm^2 TACSR conductor that is commonly used in the Japanese transmission network. The conductor parameters are shown in Table 4.1.

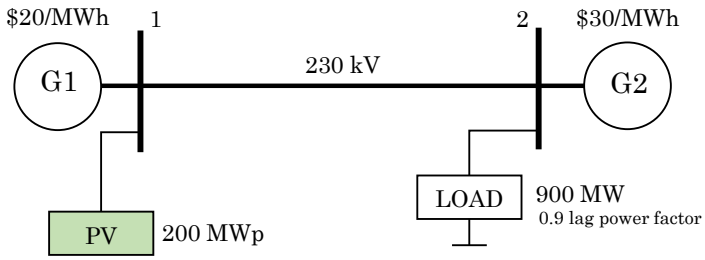

Fig. 5.16: Two-generator, two-bus test system with load and PV generator.

As shown in Fig. 5.16, in addition to the two thermal generators at the two buses, a PV source is also connected to bus 1. The fluctuations in PV output are assumed to be covered by the more expensive thermal generator at bus 2 so that the PV power output fluctuations propagate as power flow fluctuations in the transmission line.

The solar radiation probabilistic model presented in Chapter 3 and [20] was used to generate fluctuations in PV generation. Similarly, probabilistic models for ambient

temperature and wind speed were developed[4] and assumed for the weather conditions around the transmission line. Fig. 5.17 shows the probability distributions of 15-minute ahead forecasted weather conditions where the expected values of ambient temperature, wind speed, and solar radiation are 25°C, 1.2 m/s and 704 W/m^2 respectively. Under these weather conditions, the line DLR is 2433 A (25% higher than the SLR of 1942 A).

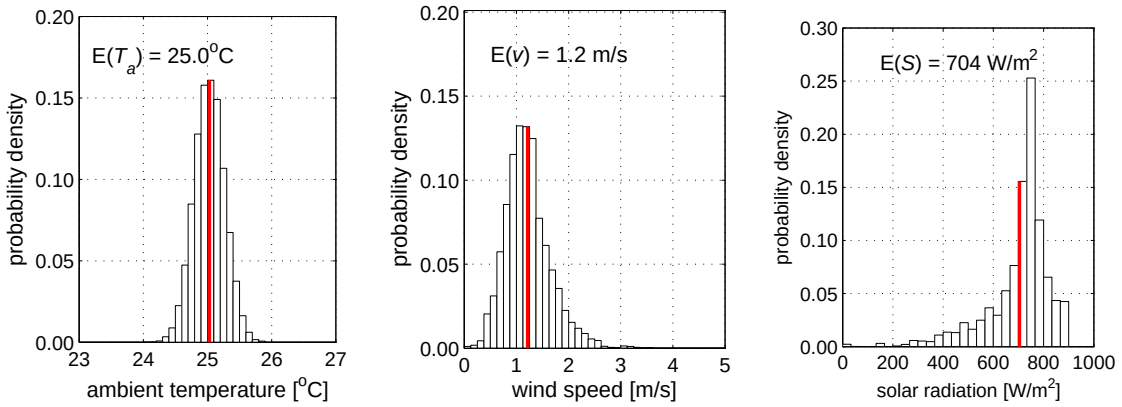

Fig. 5.17: Probability distributions of 15-minute ahead forecasted weather conditions.

The line overload risk assessment is started from a deterministic optimal power flow (DOPF) solution. Two DOPF solutions are considered: i) using the SLR and 2) using the DLR. With the SLR, the lower line ampacity means that the cheaper generator G1 is restricted to 632 MW while G2 is scheduled at 162 MW. However, with the DLR G1 is scheduled to supply the entire system net load (plus losses) of 813 MW while G2 is scheduled at 0 MW i.e. G2 is used only for reserve purposes. The line overload risk assessment is then carried out by Monte Carlo simulations – running 20,000 scenarios of PV generation and ambient weather conditions around the conductor.

Two power flow models and two conductor temperature models are considered. For the power flow models, either the full ac power flow model or a linear power flow model is used. In the linear power flow case, the nonlinear power flow equations are linearized around the original DOPF solution. For the conductor temperature model, either the full CIGRE model [8] or the simplified model [21] is used.

Figs. 5.18(a) and (b) show the obtained conductor temperature probability distributions under the SLR and DLR respectively. As expected, the plots show that the conductor temperatures are higher with the DLR. All four simulation models give relatively similar probability distribution curves. Table 5.2 shows that the risk of line overload is higher with the DLR as compared to the SLR. The simplified model however gives slightly higher overload risk values because the simplified model is constructed from a slightly conservative point-of-view [21]. Table 5.3, compares the risk assessment computation time for each of the four simulation cases and shows significant computation time savings when the linear power flow model and the simplified conductor temperature models are used.

The relationship between line rating and line overload risk is illustrated by running

[4]The probabilistic models were developed using actual single geographical point data taken from a weather station located in Osaka, Japan

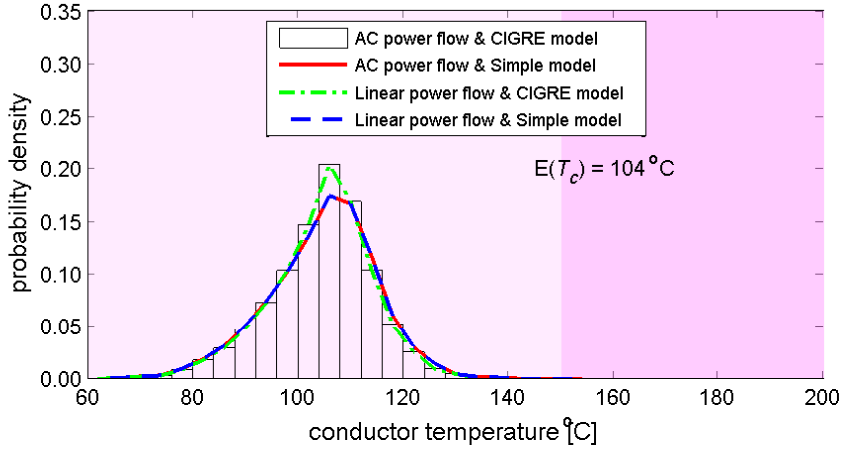

(a)

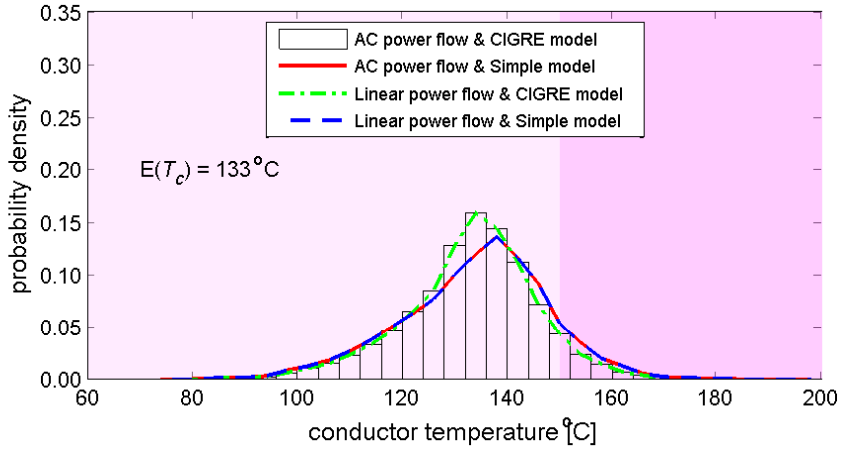

(b)

Fig. 5.18: Probability distributions of conductor temperature without generation re-dispatch for (a) SLR and (b) DLR.

Table 5.2: Probability of transmission line overload

Simulation	AC power flow		Linearized power flow	
conditions	CIGRE model	Simplified model	CIGRE model	Simplified model
SLR	$< 0.01\%$	0.02%	$< 0.01\%$	0.02%
DLR	9.11%	10.50%	9.09%	10.44%

Table 5.3: Comparison of computation time (in seconds)

Simulation	AC power flow		Linearized power flow	
conditions	CIGRE model	Simplified model	CIGRE model	Simplified model
SLR	109.8	80.2	34.6	5.8
DLR	107.9	81.8	35.2	6.2

the risk assessment procedure for different values of line rating. An effective line rating $I_{\max}^{\text{eff}}$ is defined as:

$$I_{\max}^{\text{eff}} = I_{\max}^{\text{SLR}} + \gamma\left(I_{\max}^{\text{DLR}} - I_{\max}^{\text{SLR}}\right) \tag{5.6}$$

where $I_{\max}^{\text{SLR}}$ and $I_{\max}^{\text{DLR}}$ are the SLR and the DLR respectively, and γ is the line rating safety factor. By varying γ between 0 and 1, $I_{\max}^{\text{eff}}$ varies between the SLR and the DLR. The variation of line overload risk with line rating is shown in Fig. 5.19. Also shown in Fig. 5.19 is the expected thermal generation costs illustrating the trade-off between line overload risk and operational costs. Fig. 5.19 suggests that, using an acceptable value of line overload risk, the system operator can vary the system power generation costs.

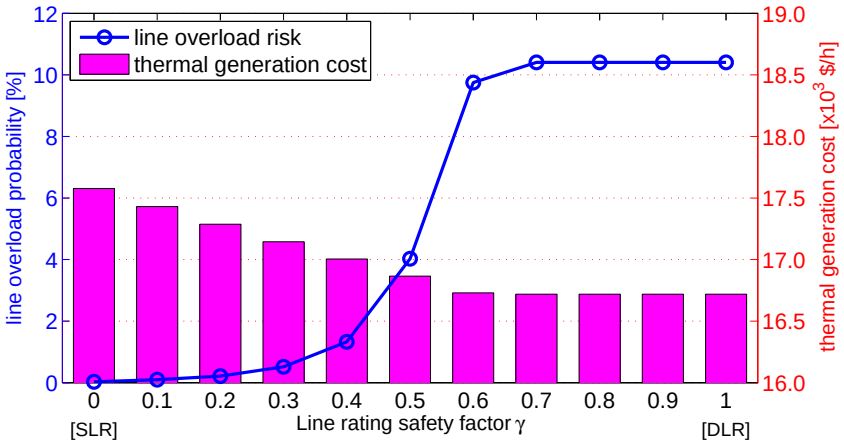

Fig. 5.19: Variation of line overload risk and thermal generation cost with line rating.

5.7 Summary

Several concepts concerning the thermal ratings of an overhead transmission line are discussed in this chapter. These can be summarized as follows:

1. A short-term dynamic thermal rating termed the dynamic electro-thermal rating (DETR) that incorporates the overhead conductor thermal inertia characteristic is presented. Simulation results show that DETR gives higher ratings than the traditional DLR especially when applied for short durations such as 5 or 10 minutes. DETR could therefore be especially useful in allowing short duration fluctuations in current as a result of increased integration of IRE sources in power networks.
2. A methodology for determining DLR safety factors to ensure that forecasted line ampacity is not higher than actual line ampacity is presented. Simulation results show that even with the application of such safety factors, real-time ratings (DLR) still result in significant increases in line loadability. However, care should be taken to ensure that all sources of uncertainty are included in the determination of DLR safety factors.
3. A methodology for assessment of the risk of overhead transmission line overload is illustrated. The application of a simplified conductor temperature model and a linear power flow model in the risk assessment procedure gives significant savings

in computation time. The methodology is proposed for application in a fast risk assessment algorithm within a probabilistic optimal power flow environment.

Each of the above approaches are intended to provide a new way of setting thermal ratings of overhead transmission lines. The main conclusions are that real-time ratings of overhead conductors based on real-time monitoring of ambient weather conditions can result in significant benefits and, as seen in Fig. 5.19, the risk of line overload can be regulated by varying the line rating.

5.8 References

[1] M. Simms and L. Meegahapola, "Comparative analysis of dynamic line rating models and feasibility to minimise energy losses in wind rich power networks," *Energy Conversion and Management*, vol. 75, pp. 11 – 20, 2013. doi: https://doi.org/10.1016/j.enconman.2013.06.003.

[2] C. J. Wallnerström, Y. Huang, and L. Söder, "Impact from dynamic line rating on wind power integration," *IEEE Transactions on Smart Grid*, vol. 6, pp. 343–350, Jan 2015. doi: https://doi.org/10.1109/TSG.2014.2341353.

[3] D. A. Douglass, D. C. Lawry, A. A. Edris, and E. C. Bascom, "Dynamic thermal ratings realize circuit load limits," *IEEE Computer Applications in Power*, vol. 13, pp. 38–44, Jan 2000. doi: https://doi.org/10.1109/67.814665.

[4] B. O. Ngoko, H. Sugihara, and T. Funaki, "A short-term dynamic thermal rating for accommodating increased fluctuations in conductor current due to intermittent renewable energy," in *2016 IEEE PES Asia-Pacific Power and Energy Engineering Conference (APPEEC)*, pp. 141–145, Oct 2016. doi: https://doi.org/10.1109/APPEEC.2016.7779486.

[5] B. Ngoko, H. Sugihara, and T. Funaki, "Methodology for the determination of real-time dynamic line ratings for secure operation of overhead conductors," in *2017 IEEE PES Innovative Smart Grid Technologies Conference Europe (ISGT-Europe)*, pp. 1–6, Sept 2017. doi: https://doi.org/10.1109/ISGTEurope.2017.8260151.

[6] S. D. Foss and R. A. Maraio, "Dynamic line rating in the operating environment," *IEEE Transactions on Power Delivery*, vol. 5, pp. 1095–1105, Apr 1990. doi: https://doi.org/10.1109/61.53127.

[7] CIGRE Working Group B2.36, "Guide for application of direct real-time monitoring systems," June 2012. CIGRE Technical Brochure.

[8] CIGRE Working Group 22.12, "Thermal behaviour of overhead conductors," August 2002. CIGRE Technical Brochure, Available from: https://e-cigre.org/publication/207-thermal-behaviour-of-overhead-conductors.

[9] "IEEE standard for calculating the current-temperature relationship of bare overhead conductors," *IEEE Std 738-2012 (Revision of IEEE Std 738-2006 - Incorporates IEEE Std 738-2012 Cor 1-2013)*, pp. 1–72, Dec 2013. doi: https://doi.org/10.1109/IEEESTD.2013.6692858.

[10] K. W. Cheung and J. Wu, "Enhancement of real-time operational efficiency by applying dynamic line ratings," in *Proceedings of the 2016 IEEE PES Asia-Pacific Power and Energy Conference, Xi'an, China*, pp. 103–107, Nov 2016. doi: https://doi.org/10.1109/APPEEC.2016.7779477.

[11] B. Xu, A. Ulbig, and G. Andersson, "Impacts of dynamic line rating on power dispatch performance and grid integration of renewable energy sources," in *IEEE PES ISGT Europe 2013*, pp. 1–5, Oct 2013. doi: https://doi.org/10.1109/ISGTEurope.2013.6695410.

[12] H. Banakar, N. Alguacil, and F. D. Galiana, "Electrothermal coordination part I: theory and implementation schemes," *IEEE Transactions on Power Systems*, vol. 20, pp. 798–805, May 2005. doi: https://doi.org/10.1109/TPWRS.2005.846196.

[13] N. Alguacil, M. H. Banakar, and F. D. Galiana, "Electrothermal coordination part II: case studies," *IEEE Transactions on Power Systems*, vol. 20, pp. 1738–1745, Nov 2005. doi: https://doi.org/10.1109/TPWRS.2005.857836.

[14] T. Krontiris, A. Wasserrab, and G. Balzer, "Weather-based loading of overhead lines - consideration of conductor's heat capacity," in *2010 Modern Electric Power Systems*, pp. 1–8, Sept 2010. Available from: https://ieeexplore.ieee.org/iel5/5996359/6007154/06007162.pdf.

[15] C. R. Black and W. A. Chisholm, "Key considerations for the selection of dynamic thermal line rating systems," *IEEE Transactions on Power Delivery*, vol. 30, pp. 2154–2162, Oct 2015. doi: https://doi.org/10.1109/TPWRD.2014.2376275.

[16] T. Ringelband, P. Schäfer, and A. Moser, "Probabilistic ampacity forecasting for overhead lines using weather forecast ensembles," *Electrical Engineering*, vol. 95, pp. 99–107, Jun 2013. doi: https://doi.org/10.1007/s00202-012-0244-8.

[17] X. Sun, P. B. Luh, K. W. Cheung, and W. Guan, "Probabilistic forecasting of dynamic line rating for over-head transmission lines," in *2015 IEEE Power Energy Society General Meeting*, pp. 1–5, July 2015. doi: https://doi.org/10.1109/PESGM.2015.7286604.

[18] F. Fan, K. Bell, and D. Infield, "Probabilistic weather forecasting for dynamic line rating studies," in *2016 Power Systems Computation Conference (PSCC)*, pp. 1–7, June 2016. doi: https://doi.org/10.1109/PSCC.2016.7540854.

[19] R. J. Hyndman and G. Athanasopoulos, *Forecasting: Principles and Practice*. OTexts, Oct. 2013, Available online from: www.otexts.org/book/fpp.

[20] B. Ngoko, H. Sugihara, and T. Funaki, "Synthetic generation of high temporal resolution solar radiation data using markov models," *Solar Energy*, vol. 103, pp. 160 – 170, 2014. doi: https://doi.org/10.1016/j.solener.2014.02.026.

[21] B. Ngoko, H. Sugihara, and T. Funaki, "Validation of a simplified model for estimating overhead conductor temperatures under dynamic line ratings," *IEEJ Transactions on Power and Energy*, vol. 138, no. 4, pp. 284–296, 2018. doi: https://doi.org/10.1541/ieejpes.138.284.

CHAPTER 6

Optimal system operation with dynamic line ratings and intermittent renewable generation

6.1 Introduction

This chapter presents a new formulation of the optimal power flow (OPF) problem considering uncertainty costs due to the IRE sources and explicit conductor temperature limits calculated from monitored ambient weather conditions. The thermal characteristics of monitored overhead conductors are incorporated into the OPF formulation using the simplified conductor temperature model presented in Chapter 4. A key difference with the classical OPF formulations is that the proposed formulation considers not only the cost of conventional generation, but also the costs due to uncertainty of IRE sources in the power system. A detailed analysis and discussion of the effects of monitored weather conditions on generation scheduling and related costs is also presented.

6.2 Literature review of optimal power system operation with IRE and DLR

As outlined in Chapter 2, environmental concerns, government support, and advances in technology render intermittent renewable energy (IRE) sources economically viable, resulting in steady increases in their proportions in electric power networks [1]. While the advantages of these green energy sources are numerous, one of the main operational challenges is the high uncertainty in their output. Forecasts of the power available from the IRE sources used for establishing the system-generation schedules are generally characterized by uncertainty levels that are higher than typical in traditional load and generation forecasts [2]. This increased uncertainty in the available generation necessitates the operation of relatively more expensive, fast-acting spinning reserves to substitute for the generation shortages in real time, which result from the overestimation of the available IRE power in the system [3, 4].

Energy management, i.e., economic dispatch (ED), unit commitment (UC), and optimal power flow (OPF) in networks with significant proportions of generation from IRE

sources require mechanisms for handling the increased uncertainty owing to the intermittency of these sources. Practically, this can be realized in two ways: The first approach involves the application of stricter reserve requirements to ensure generation adequacy, even with large overestimations of the IRE output [5, 6]. The reserve requirements can be set deterministically for worst-case forecasting conditions or stochastically, considering the statistical distribution of the IRE forecasts [7]. Alternatively, a risk-based approach, which adds an IRE-output uncertainty-related cost in the problem objective function, can be adopted. Several risk-based energy management approaches have been proposed in literature, utilizing stochastic programing techniques [8, 9], chance-constrained approaches [10, 11, 12], and robust optimization [13, 14]. While the underlying formulations and solution approaches may differ, the IRE uncertainty (risk) cost increases with the increase in the scheduled IRE output; the cost curve being dependent on the IRE source statistical characteristics (expected value and variance of the IRE output; and the statistical distribution of the forecasting error).

In addition to affecting the operational costs, increased IRE generation alters the line flows in a power system, which in turn increase the probability of violating the thermal limits of the transmission lines [15]; this mostly occurs in networks where the IRE sources are concentrated at particular locations in the system. Traditionally, highly conservative approaches are used in setting the line-flow limits; the maximum conductor current (or power) is calculated assuming poor cooling conditions (low wind speeds and high ambient temperature) [16, 17]. The resultant rating, referred to as the static line rating (SLR), can be expensive because it may restrict the use of certain transmission paths carrying power from cheaper generation sources. Additionally, this may impact the scheduled IRE generation, which is characterized by near-zero fuel costs.

Ambient weather conditions around overhead transmission lines have a significant impact on conductor cooling and consequently, on their thermal limits [18, 19, 20]. Therefore, the conservativeness enforced by the SLR approach can be relaxed by monitoring the ambient weather conditions around the conductor and by utilizing this data to estimate the conductor temperature and loadability. An approach in which line rating (in terms of power or current carrying capacity) is continuously varied based on monitoring of prevailing weather conditions is referred to as dynamic line rating (DLR) [16, 21].

It has been variously demonstrated that the less conservative approach of setting transmission line loadability based on conductor monitoring can results in benefits for both system operators and electricity consumers. Reference [22] shows that DLR could increase area-to-area transmission capacity thereby impacting electricity prices and benefiting electricity consumers. Reference [23] demonstrates reductions in the optimal system operating costs based on a solution of the conventional UC problem with DLR. Reference [21] illustrates an increase in the utilization of wind power owing to increased loadability of a transmission line connected to a wind farm. Similar results are reported by [24] who demonstrate that more wind power can be integrated into the grid with reduced load and IRE generation curtailments. The explicit incorporation of the overhead-conductor thermal characteristics in power system energy management tools is illustrated in [25],

under the concept of electro-thermal coupling (ETC). The authors extend their work by illustrating possible practical applications of ETC in [26].

While the potential benefits are clearly apparent, a challenge exists in the direct use of the conductor temperature limits in the solution of the OPF and UC problems because of the complex, nonlinear nature of the equations that model the heat transfer processes acting on the conductor. In [27] the problem complexity is reduced by ignoring the variations of conductor heating and cooling rates with temperature. Similarly, in [25] and [26] constant conductor heating and cooling rates are assumed resulting in an over-simplified formulation though the simulations illustrate the benefits of DLR. Additionally, formulations that study the link between IRE integration and relaxed transmission line ratings such as [24] assume perfect IRE forecasts thereby neglecting costs due to the uncertainty of the IRE sources.

This chapter deals with the formulation and solution of the OPF problem considering uncertainty costs due to the IRE sources and explicit conductor temperature limits calculated from monitored ambient weather conditions. The simplified conductor temperature model described in detail in Chapter 4 is used to simplify the integration of the conductor thermal characteristics in the traditional OPF model. Numerical simulations conducted on a typical test system demonstrate the effects of the IRE uncertainty costs and the economic benefits of conductor-temperature monitoring, based on the OPF solutions. In addition, sensitivity analyses illustrate the dependence of the obtained generation schedules on the IRE uncertainty costs and the monitored conductor temperature.

6.3 Conductor temperature calculation

The simplified conductor temperature model described in Chapter 4 and in reference [28] is used to simplify the calculation of conductor temperature within the OPF calculations. The steady state equation is re-written here as:

$$T_c = \beta_0 + \beta_1 I_c^2 + \beta_2 I_c^4, \tag{6.1}$$

where T_c is the conductor temperature, I_c is the conductor current, and β_0, β_1, and β_2 are model constants [28].

Equation (6.1) expresses T_c as an explicit quadratic function of the square of the current, where the model constants β_0, β_1, and β_2 are dependent only on the weather parameters and the electrical and physical characteristics of the conductor. The validity of the approximate model in approximating the conductor temperature is discussed in detail in [28].

6.4 OPF problem formulation with IRE sources and conductor temperature limits

The traditional OPF problem formulation aims to minimize the thermal generation cost in a power system, while meeting the operational constraints, including the generator-output limits, bus-voltage magnitudes, and line flows in terms of the maximum current

(or equivalent maximum power) [29, 30]. In this chapter, the traditional OPF problem formulation is extended to include the costs accounting for the IRE output uncertainty and an explicit use of the maximum conductor temperature, where the conductor temperature is estimated using the monitored ambient weather data and the current magnitudes. The determination of the IRE uncertainty costs is outlined, followed by its integration into the OPF formulation.

6.4.1 Costing uncertainty due to intermittent renewable energy sources

In terms of power generation costs, IRE sources operate at nearly zero variable costs because the operating fuel (solar/wind energy) is free. Owing to the low marginal costs of the IRE sources compared to those of the thermal generators, any optimal solution based on the operating costs will schedule the IRE sources at the maximum possible value; the usual practice being to schedule the forecasted (expected) value. The main operating cost relating to IRE sources then arises from the fact that the available IRE power may be less than scheduled due to unpredictability. The uncertainty of the IRE sources has to be covered by reserve generation that is typically more expensive than the conventional generation. In a manner similar to the fuel costs of thermal generators, the cost of covering for IRE uncertainty can be used to decide on an optimal value for the scheduled IRE generation.

The approach proposed in [31] is used here to model the IRE uncertainty costs. Let $f(p_r)$ be the probability distribution of the actual output p_r of an IRE source and P_r be the scheduled value. If the actual IRE generation is lower than the scheduled value ($p_r < P_r$), generation reserves have to be operated to cover for the shortfall due to the overestimation which will incur an associated IRE overestimation cost. On the other hand, if at the time of operation, actual IRE generation is higher than the scheduled value ($p_r > P_r$), the system operator may have to either curtail the extra IRE power due to underestimation, or by fast re-dispatch reduce the amount of power bought from thermal generation incurring a penalty cost for loss of revenue for generation companies. These actions can be modeled by an IRE underestimation cost [31].

If a constant unit cost for IRE overestimation κ_o [\$/MWh] is assumed and similarly, a constant unit cost for IRE underestimation κ_u [\$/MWh] is assumed, then the expected cost due to IRE uncertainty C_r will be given by:

$$C_r\left(P_r\right) = \kappa_o \overline{p_{ro}} + \kappa_u \overline{p_{ru}} \qquad [\$/\text{h}] \tag{6.2}$$

where $\overline{p_{ro}}$ [MW] and $\overline{p_{ru}}$ [MW] are the expected values of the IRE overestimate and underestimate respectively and are dependent on P_r i.e.:

$$\overline{p_{ro}} = \frac{\int_0^{P_r} \left(P_r - p_r\right) f\left(p_r\right) dp_r}{\int_0^{P_r} f\left(p_r\right) dp_r} \tag{6.3}$$

and

$$\overline{p_{ru}} = \frac{\int_{P_r}^{P_r^{max}} (P_r - p_r)\, f(p_r)\, dp_r}{\int_{P_r}^{P_r^{max}} f(p_r)\, dp_r} \tag{6.4}$$

Consider an IRE resource whose probability distribution is as shown in Fig. 6.1. The values of $\overline{p_{ro}}$ and $\overline{p_{ru}}$ for a scheduled value P_r will be as shown. The variation of IRE uncertainty costs with scheduled IRE generation for different values of the mean IRE forecast and forecast error standard deviation will be as shown in Fig. 6.2. The IRE uncertainty cost curves depend on the cost coefficients κ_o and κ_u as shown in [31].

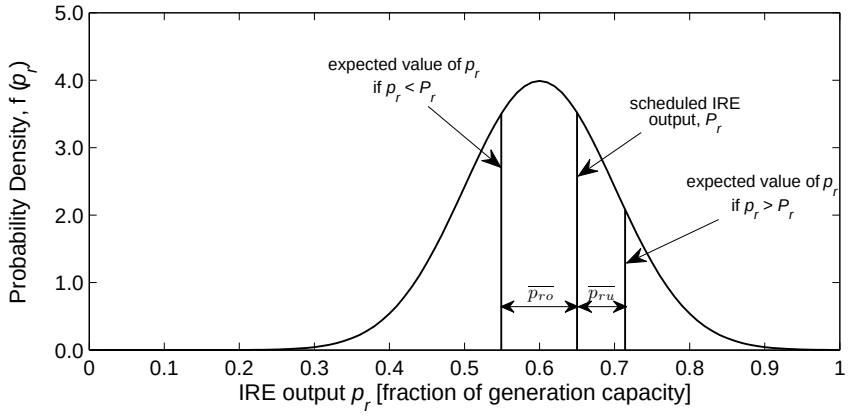

Fig. 6.1: Probability distribution of IRE generation illustrating expected values of overestimation and underestimation for a particular scheduled value.

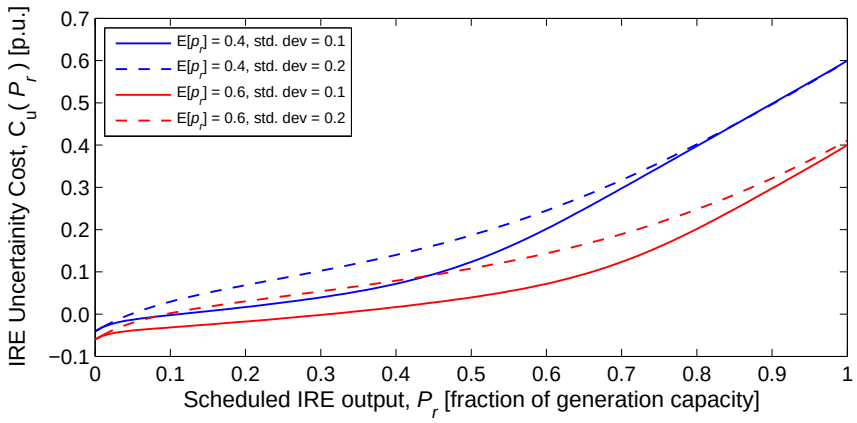

Fig. 6.2: IRE uncertainty cost curves ($\kappa_o = 1$ and $\kappa_u = 0.1$).

Fig. 6.2 shows that the IRE uncertainty cost increases as the scheduled IRE output increases with the cost coefficients κ_o and κ_u dictating the nature of the curve. However, as the magnitude of the scheduled IRE-source output increases, the portion of the system load accounted for by conventional generators decreases, resulting in a reduction in the conventional generation costs.

6.4.2 Problem formulation and solution methodology

The AC OPF problem with IRE sources and conductor temperature constraints is formulated as

$$\min_{P_{gi},\, P_{rj}} \quad \sum_{i\in\mathcal{G}} C_{gi}\left(P_{gi}\right) + \sum_{j\in\mathcal{R}} C_{rj}\left(P_{rj}\right). \tag{6.5}$$

Subject to:

$$P_{gi} + P_{ri} - P_{di} = \sum_{j\in\Omega_i} Y_{ij}V_iV_j\cos\left(\theta_{ij} - \delta_i + \delta_j\right), \quad \forall i \in \mathcal{N} \tag{6.6}$$

$$Q_{gi} - Q_{di} = \sum_{j\in\Omega_i} Y_{ij}V_iV_j\sin\left(\theta_{ij} - \delta_i + \delta_j\right), \quad \forall i \in \mathcal{N} \tag{6.7}$$

$$I_{ij}^2 = \frac{V_i^2 + V_j^2 - 2V_iV_j\left(\cos\delta_i - \cos\delta_j\right)}{R_{ij}^2 + X_{ij}^2}, \quad \forall i,j \in \mathcal{N} \tag{6.8}$$

$$T_{c,ij} = \beta_{0,ij} + \beta_{1,ij}I_{ij}^2 + \beta_{2,ij}I_{ij}^4, \quad \forall ij \in \mathcal{L} \tag{6.9}$$

$$P_{gi}^{min} \le P_{gi} \le P_{gi}^{max}, \quad \forall i \in \mathcal{G} \tag{6.10}$$

$$0 \le P_{ri} \le P_{ri}^{max}, \quad \forall i \in \mathcal{R} \tag{6.11}$$

$$V_i^{min} \le V_i \le V_i^{max}, \quad \forall i \in \mathcal{N} \tag{6.12}$$

$$T_{a,ij} \le T_{c,ij} \le T_{c,ij}^{max}, \quad \forall ij \in \mathcal{L}. \tag{6.13}$$

In (6.5)–(6.13), i and j are the bus indices, $\mathcal{N}$ is the set of indices of all the buses, $\mathcal{G}$ and $\mathcal{R}$ are the sets of bus indices with connected thermal and IRE generators, respectively and Ω_i is the set of bus indices for the buses connected to bus, i. ij is a network-branch index for a branch connecting buses i and j, and $\mathcal{L}$ is the set of all transmission-line indices. P_{di} and Q_{di} are the real and reactive power demands, respectively, at bus i; P_{gi} and Q_{gi} are the scheduled real and reactive power outputs, respectively, of the thermal generator at bus, i; P_{ri} is the scheduled power output of the IRE source connected to bus, i. V_i^{min} and V_i^{max} are the minimum and maximum voltage magnitudes, respectively, at bus, i; R_{ij} and X_{ij} are the resistance and reactance, respectively, of the network branch connecting buses i and j; Y_{ij} and θ_{ij} are the magnitude and angle, respectively, of the impedance of the branch connecting buses i and j; V_i and δ_i are the voltage magnitude and angle, respectively, at bus, i, and $I_{c,ij}$ is the magnitude of the current flowing between buses i and j.

The objective function (6.5) is a sum of the generation cost of the conventional generators and the total uncertainty cost owing to the IRE sources. The IRE-source uncertainty cost for a generator at bus i is given by (6.2), while a quadratic cost function is assumed for the thermal generators, as follows:

$$C_{gi}\left(P_{gi}\right) = a_{0i} + a_{1i}P_{gi} + a_{2i}P_{gi}^2, \tag{6.14}$$

where a_{0i}, a_{1i}, and a_{2i} are the cost function coefficients for the thermal generator connected to bus, i.

Constraints (6.6) and (6.7) represent the active and reactive power balances at bus i, respectively. The square of the magnitude of the current flowing through the branch connecting buses i and j is obtained from (6.8), which is used in (6.9) to determine the temperature of the conductor connecting buses i and j. Constraints (6.10)–(6.13) represent the physical limits for each of the decision variables.

It is to be noted that a constant conductor resistance value, R_{ij}, is used in the determination of $I^2_{c,ij}$ in (6.8). Although the resistance of the conductor varies with the conductor temperature, since the reactance, X_{ij}, is generally much larger than R_{ij}, the effect of the variation in resistance with temperature can be neglected.

6.5 Numerical simulations

In this section, the performance of the OPF formulation with IRE sources and explicit conductor-temperature limits is investigated using a modified version of the IEEE 30-bus benchmark system [32, 33]. The bus and branch data for the system is given in Appendix D. The nonlinear optimization problem described by (6.5)–(6.13) is solved using the MATLAB interior point solver (MIPS) available in the MATPOWER package [34]. The solution approach leverages the existing architecture in MATPOWER, which is generally used for solving power-flow and optimal-power-flow problems, with extensions to deal with the extra decision variables (scheduled outputs of the IRE sources) and the conversion of the branch flow constraints from maximum current/power to maximum temperature, using the simplified version of the heat balance equation described in Chapter 4. The interior point solver MIPS requires the first and second derivatives of the objective function in the solution algorithm [34].

6.5.1 Test system

The configuration of the modified IEEE 30-bus test system in Fig. 6.3 shows that the system has 41 branches, i.e., 36 transmission lines and 5 transformers. The transmission network is operated at two nominal voltage levels: 132 kV on the upper- side of the three main transformers and 33 kV on the lower side. All the conductors are assumed to be 160mm^2 ACSR overhead conductors; their data are listed in Table 6.1. The maximum conductor temperature of 90°C corresponds to an SLR of 471 A (107 MVA for the 132 kV lines and 27 MVA for the 33 kV lines). Six conventional generators are located at buses 1, 2, 13, 22, 23, and 27, as shown in Fig. 6.3, with the generator data as given in Table 6.2. The generator cost coefficients are scaled from the 1997 data given in [33] to give more realistic energy costs and the maximum generator limits are increased by 50% to enable the simulation of a more heavily loaded system. Similarly, load levels 50% higher

Table 6.1: 160 mm^2 ACSR conductor data [35]

Property	D [mm]	$R_{ac}^{20^\circ C}$ [Ω/km]	α [/°C]	T_c^{max} [°C]	SLR [A]
Value	18.2	0.1711	0.004	90	471

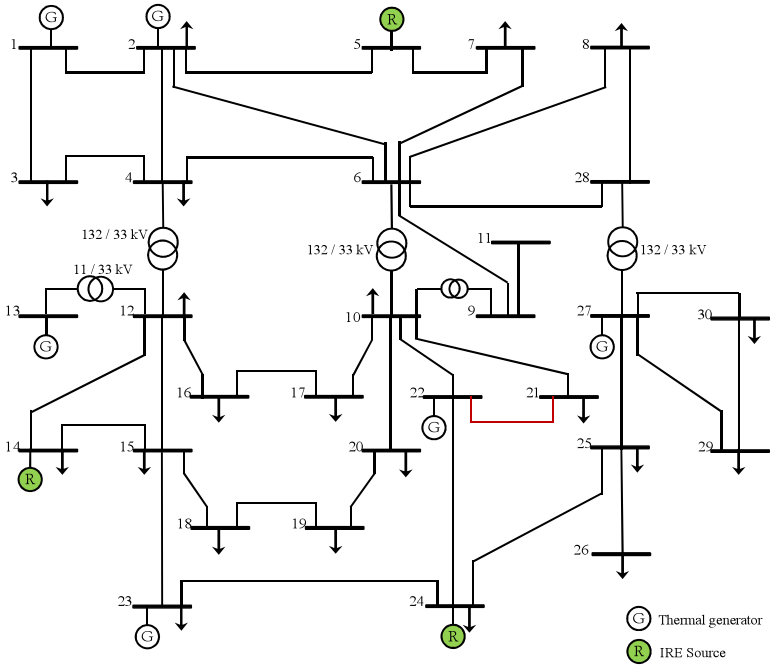

Fig. 6.3: Modified IEEE 30-bus test system.

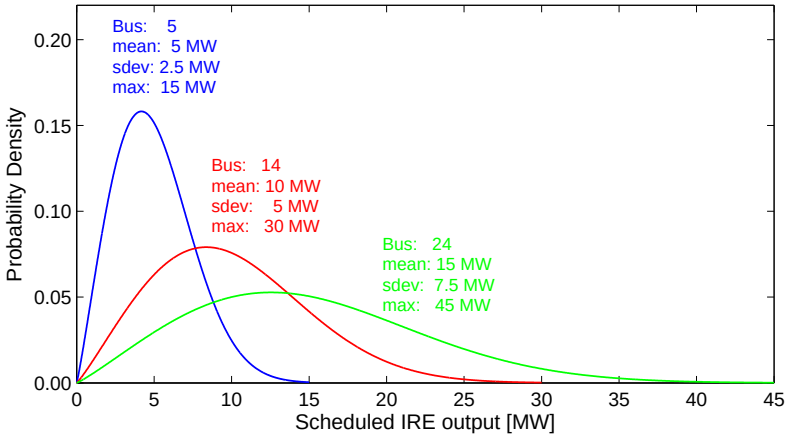

Fig. 6.4: IRE source probability density functions.

Table 6.2: Conventional generator data

Bus	Cost Coefficients			Generator Limits	
#	a_0 [$/h]	a_1 [$/MWh]	a_2 [$/MW^{2}h]	P_g^{min} [MW]	P_g^{max} [MW]
1	0	10.00	0.1000	0	120
2	0	8.75	0.0875	0	120
13	0	15.00	0.1250	0	60
22	0	5.00	0.3125	0	75
23	0	15.00	0.1000	0	45
27	0	16.25	0.0417	0	80

than the magnitudes given in [32] are applied. In addition to the conventional generators, three IRE sources are introduced, which are located at buses 5, 14, and 24. The random IRE-source outputs are assumed to follow a Weibull distribution [36] with probability distributions as shown in Fig. 6.4. Using an assumption of no cost for IRE curtailment, the underestimation cost coefficient κ_u is set to zero while the overestimation cost coefficient κ_o is set to \$80/MWh in the base case simulation, for each of the three IRE sources. Since $\kappa_u = 0$, the rest of the discussion refers to κ_o simply as the uncertainty cost coefficient.

6.5.2 Simulation cases

The OPF problem with IRE sources and explicit conductor-temperature limits for the described test system is solved for three simulation cases.

Case A The conventional OPF problem, which uses worst-case weather conditions to set the conductor thermal limits and neglects the IRE uncertainty costs in the problem formulation, is solved. In this case, the IRE sources are scheduled at their forecasted (expected) outputs and the corresponding IRE uncertainty costs are determined from the OPF solution. The use of the worst-case weather conditions to calculate the conductor temperature is equivalent to the use of SLRs.

Case B In this case, the IRE uncertainty costs are considered, i.e., the outputs of the IRE sources are optimization decision variables. When compared to *Case A*, these results demonstrate the effect of including the IRE uncertainty costs on the scheduling decisions. As with *Case A*, worst-case weather conditions are assumed for all the overhead conductors.

Case C This case is similar to *Case B* but it is assumed that the ambient weather conditions on line 21–22 are monitored. A wind speed value of 2 m/s and an ambient temperature of 25°C are used in the simulations. This case shows the effect of using monitored weather conditions on the scheduling of both conventional generation and IRE sources.

6.5.3 Simulation results

The OPF problem was solved for the three cases and the obtained optimal solutions are presented in Tables 6.3, 6.4, and 6.5, and Fig. 6.5. Table 6.3 compares the obtained optimal objective function values for the three simulation cases, whereas Table 6.4 lists the corresponding generation schedules for both conventional generators and IRE sources. The transmission line connecting buses 21 and 22 is the only conductor operated at its temperature limit in all the three cases; Table 6.5 compares the current, power flow, conductor temperature, and congestion shadow price (CSP) corresponding to line 21-22. Fig. 6.5 shows the locational marginal prices (LMPs) at each of the system's 30 buses.

The CSP, μ_{ij}, associated with the line connecting buses i and j, is the ratio of the incremental change in the objective function value to that in the constraint limit. In this case, the maximum conductor temperature is the limiting constraint; hence, the unit is \$/h·°C. If the constraint is binding, μ_{ij} has a non-negative value; else, it is zero. Then,

Table 6.3: OPF solution - objective function values [$/h]

	Case A	Case B	Case C	Difference	
				B − A	C − B
Gen. Cost	4356.68	4551.43	4365.09	+194.75	−186.35
IRE Cost	589.34	350.15	419.33	−239.19	+69.17
Obj. Fcn. Value	4946.02	4901.59	4784.41	−44.43	−117.17

Table 6.4: OPF solution - generation schedules [MW]

	Case A	Case B	Case C	Difference	
				B − A	C − B
P_{g1}	63.94	63.68	55.49	−0.26	−8.19
P_{g2}	80.92	81.40	71.72	+0.48	−9.68
P_{g13}	32.42	33.04	27.51	+0.62	−5.53
P_{g22}	11.59	14.74	27.41	+3.15	+12.67
P_{g23}	19.29	21.82	25.82	+2.53	+3.99
P_{g27}	52.80	56.76	57.64	+3.96	+0.88
Total P_g	260.95	271.44	265.58	+10.49	−5.86
P_{r5}	5.00	4.22	3.84	−0.78	−0.38
P_{r14}	10.00	8.29	7.84	−1.71	−0.44
P_{r24}	15.00	7.01	11.56	−7.99	+4.56
Total P_r	30.00	19.52	23.24	−10.48	+3.72

Table 6.5: OPF solution - operating condition of line 21–22

	Case A	Case B	Case C	Difference	
				B − A	C − B
Current [A]	469.3	469.3	717.3	0	+248.0
Power [MVA]	25.8	25.8	42.7	0	+16.9
T_c [°C]	90.0	90.0	86.8	0	−3.2
CSP [$/h·°C]	3.72	3.14	0	−0.58	−3.14

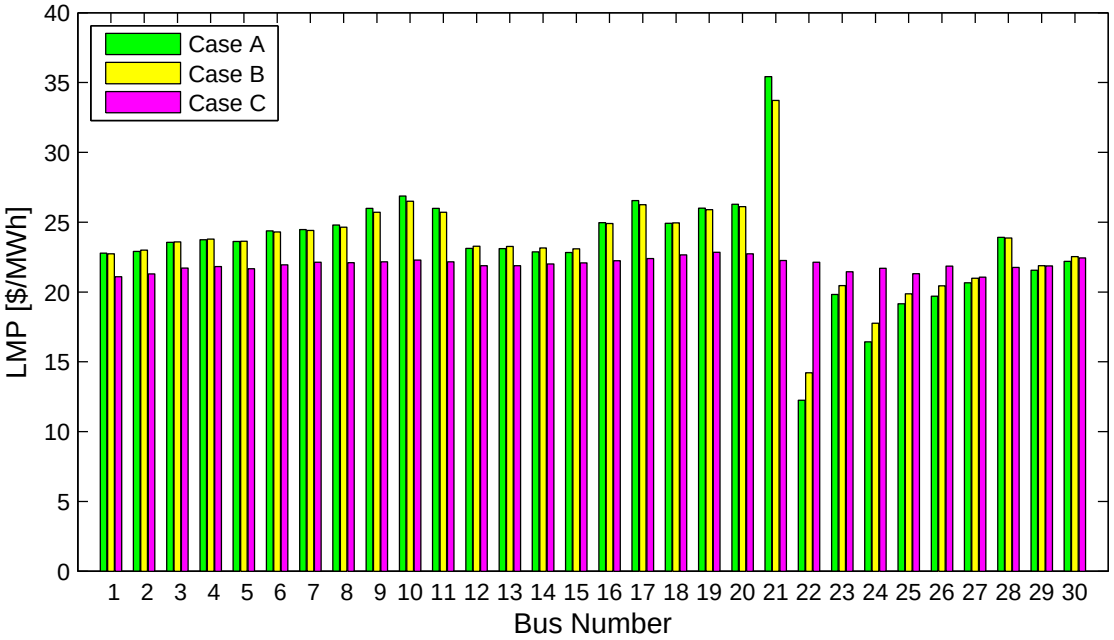

Fig. 6.5: Comparison of the LMPs at all the buses for the three simulation cases.

the marginal cost at bus, i, due to the congestion on line, ij, is given by

$$MC_i^{congestion,ij} = \mu_{ij} \frac{\partial T_{c,ij}}{\partial P_{di}}, \tag{6.15}$$

where $\partial T_{c,ij}/\partial P_{di}$ is the incremental change in the temperature of conductor, ij, due to an additional unit of power demanded at bus, i. μ_{ij} is a system congestion metric and has the effect of increasing the system cost because a non-zero value of μ_{ij} indicates that the objective function value would be reduced, if the corresponding congestion constraint was not binding. The LMP at bus i is the marginal cost of supplying the next increment of electric power demanded at a given bus, without violating any operational constraint. $MC_i^{congestion,ij}$ is a component of the LMP.

Effect of the IRE uncertainty costs

A comparison of the values corresponding to *Cases A* and *B* in Tables 6.3 and 6.4 shows that the inclusion of the IRE uncertainty costs in the objective function alters the generation schedules and the corresponding costs. This result can be obtained from the column corresponding to the differences between *Cases B* and *A* (5^{th} column). Here, the scheduled IRE generation is reduced in *Case B*, thereby reducing the associated uncertainty costs. Although the scheduled outputs of the thermal units are subsequently increased, the net result is a 0.9% (44.43 MW) reduction in the objective function value of the optimal solution in *Case B*.

Although the scheduled outputs of all the three IRE sources are reduced in *Case B*, compared to *Case A*, it is seen that the reduction is relatively larger at bus 24, compared to buses 5 and 14. The percentage reductions in the scheduled IRE generation are 15.4%, 17.2%, and 53.3% at buses 5, 14, and 24, respectively. This is attributed to the differences

in the LMPs at the three buses. As seen from Fig. 6.5, the LMPs at buses 5 and 14 (approximately \$23/MWh) are higher than that at bus 24 (approximately \$17/MWh). Thus, the unit IRE uncertainty cost of \$80/MWh is 4.7 times higher than the electricity cost at bus 24; however, it is only 3.5 times higher than the costs at buses 5 and 14, rendering it relatively cheaper to operate IRE sources at buses 5 and 14, compared to bus 24. Hence, the reduction in the scheduled IRE generation at bus 24 is higher than those at the other two buses.

A comparison of the temperature of the monitored conductor (line 21-22) in Table 6.5 shows that despite the differing schedules in Table 6.4, the line is operated at its maximum allowable temperature in both *Cases A* and *B*, carrying the SLR current[1]. However, there is a reduction in the CSP from \$3.72/h $\cdot^\circ$ C in *Case A* to \$3.14/h $\cdot^\circ$ C in *Case B*. This reduction implies that the marginal cost of increasing the system demand is lower in *Case B* than in *Case A*, translating to a reduction in the objective function value observed in Table 6.3.

Effect of conductor-temperature monitoring

A comparison of the results of *Cases B* and *C* in Table 6.5 demonstrates that favorable conductor-cooling conditions (higher wind speed and lower ambient temperature) reduce the conductor temperature, enabling more power to flow through the conductor, before the maximum permitted conductor temperature is attained. As seen from Table 6.5, although line 21-22 carries 65% more power in *Case C* than that in *Case B*, it operates at a temperature (86.8°C) that is lower than the maximum permissible value. Therefore, better conductor-cooling conditions have an effect of reducing the conservativeness of the maximum conductor-temperature constraint enforced on the line in the solutions of *Cases A* and *B*. As the maximum conductor-temperature limit constraint is not binding in *Case C* (the temperature of line 21-22 is lower than the maximum 90°C), the CSP corresponding to this case is zero.

The effect of the relaxation of the conductor thermal-limit constraint on the OPF problem optimal solution and generation schedules is observed in Tables 6.3 and 6.4. The reduced congestion in line 21-22 enables increased generation from the relatively cheaper thermal generators at buses 22, 23, and 27, and reductions in the scheduled outputs of the more expensive generators at buses 1, 2, and 13. Similarly, the scheduled output of the IRE source at bus 24 is increased, whereas those at buses 5 and 14 are reduced. The variation in the scheduled IRE sources at different buses results in an increase in the scheduled IRE generation in the system, which increases the associated IRE risk costs, as observed in Table 6.3. However, this is compensated by a reduction in the conventional generation and the net result is an overall 2.4% (117.17 MW) reduction in the objective function value. This reduction is a measure of the benefit of monitoring the temperature of the constrained line.

[1]The current of 469.3 A, corresponding to the maximum conductor temperature in Table 6.5 is marginally lower than the SLR of 471.1 A (Table 6.1) because the simplified conductor temperature model used in the OPF formulation is slightly conservative with respect to the original CIGRE model.

6.5.4 Sensitivity analysis

The simulation results described above are dependent on the values of the various parameters used in the calculations. In this section, we analyze the OPF-solution sensitivity with respect to the IRE-uncertainty-cost coefficient and the values of the monitored ambient weather conditions (ambient temperature and wind speed).

Effect of the IRE Uncertainty cost coefficient

The OPF problem was solved again, varying the IRE uncertainty cost coefficient from \$30/MWh–\$150/MWh; the effect on the scheduled IRE generation and objective function value is shown in Figs. 6.6(a) and 6.6(b), respectively. From Fig. 6.6(a), it can be observed that the scheduled IRE generation reduces as the value of κ_o increases. This is expected because an increase in κ_o increases the risk costs associated with the IRE sources, indicating a more conservative approach in the scheduling of the IRE sources. For κ_o values greater than \$120/MWh, zero IRE generation is scheduled. Fig. 6.6(a) also demonstrates that the scheduled IRE generation in *Case B* is more than that in *Case C*

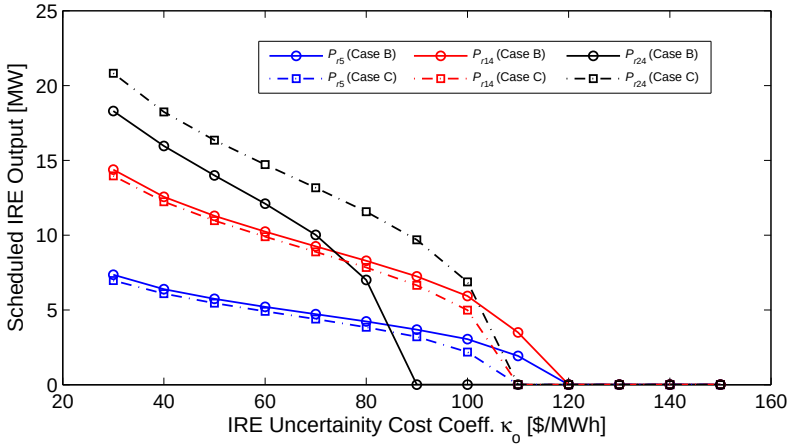

(a)

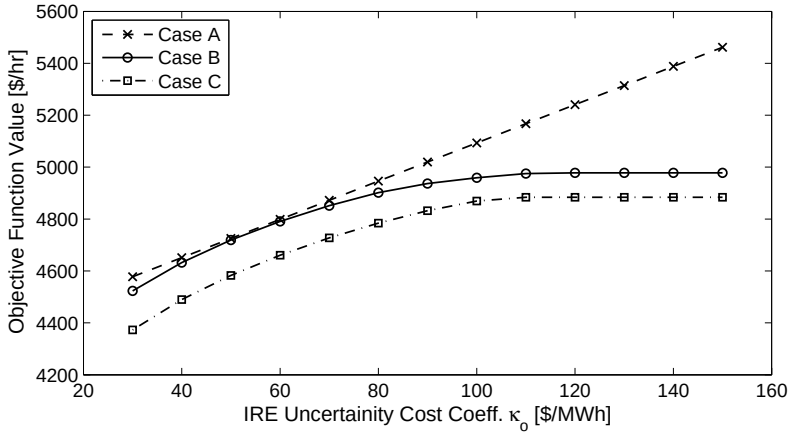

(b)

Fig. 6.6: Effect of the IRE-source uncertainty cost coefficient on the scheduled IRE generation and OPF objective function value.

for the IRE source at bus 24, whereas the converse is true for buses 5 and 14. This is because the LMP at bus 24 is increased by the relaxation of the thermal constraint on line 21-22 in *Case C*, whereas the LMPs at buses 5 and 14 are reduced, rendering the relative cost of IRE generation lower at bus 24, and higher at buses 5 and 14.

Fig. 6.6(b) shows the effect of κ_o on the obtained objective function value. In *Case A*, as the IRE generation is scheduled at the expected value, the IRE uncertainty costs increase linearly with κ_o, whereas the thermal generation costs remain constant. Therefore, the objective function value also increases linearly with κ_o. In *Cases B* and *C*, the scheduled IRE generation reduces as κ_o increases. The resulting increase in thermal generation is greater than the reduction in the IRE uncertainty costs; hence, the objective function values increase steadily to a maximum value, corresponding to the point of zero scheduled IRE generation. The curve corresponding to *Case C* is lower than that corresponding to *Case B*, indicating the effect of relaxing the maximum conductor temperature constraint on line 21-22.

Effect of the monitored ambient weather conditions

The effect of the ambient weather conditions (ambient temperature and wind speed) on the OPF problem solution was analyzed by the OPF problem again, for various values of

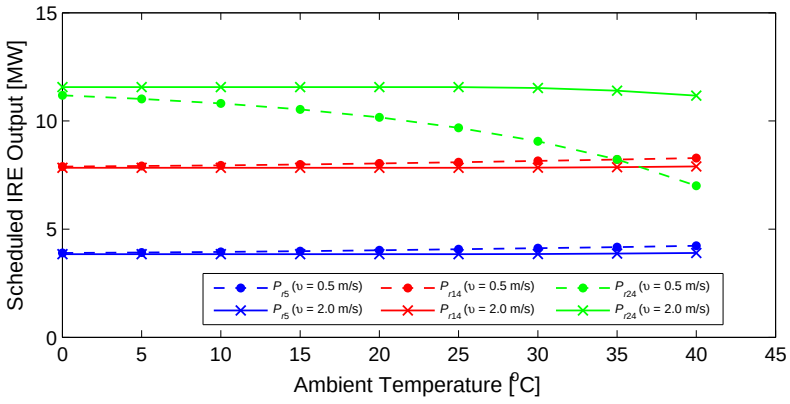

(a)

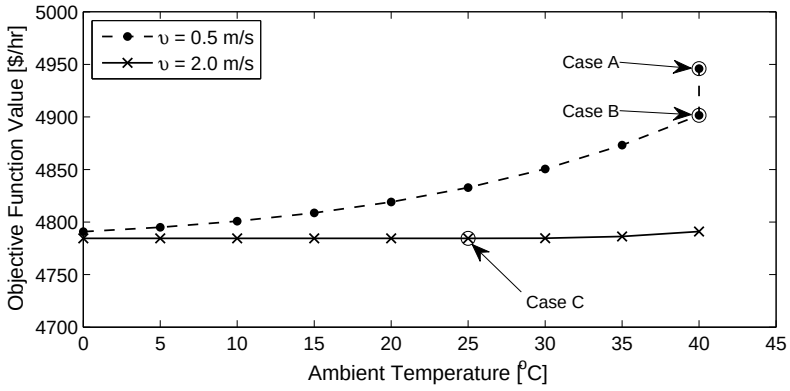

(b)

Fig. 6.7: Effect of the measured ambient temperature around line 21-22 on the scheduled IRE generation and OPF objective function value.

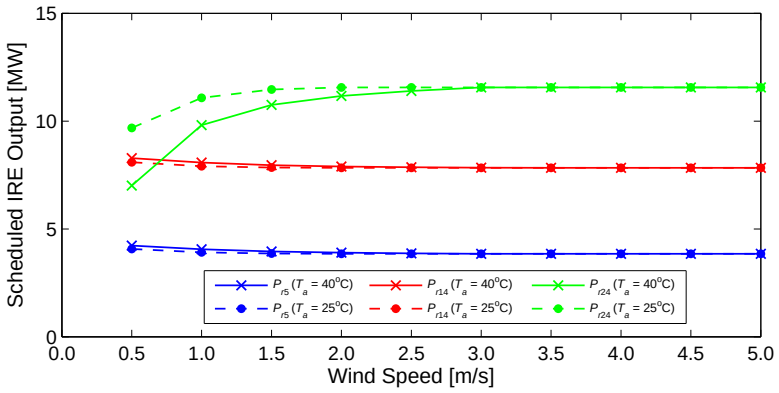

(a)

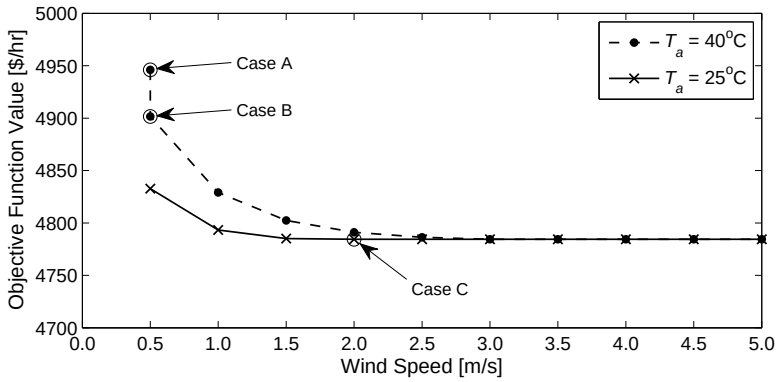

(b)

Fig. 6.8: Effect of the measured ambient wind speed across line 21-22 on the scheduled IRE generation and OPF objective function value.

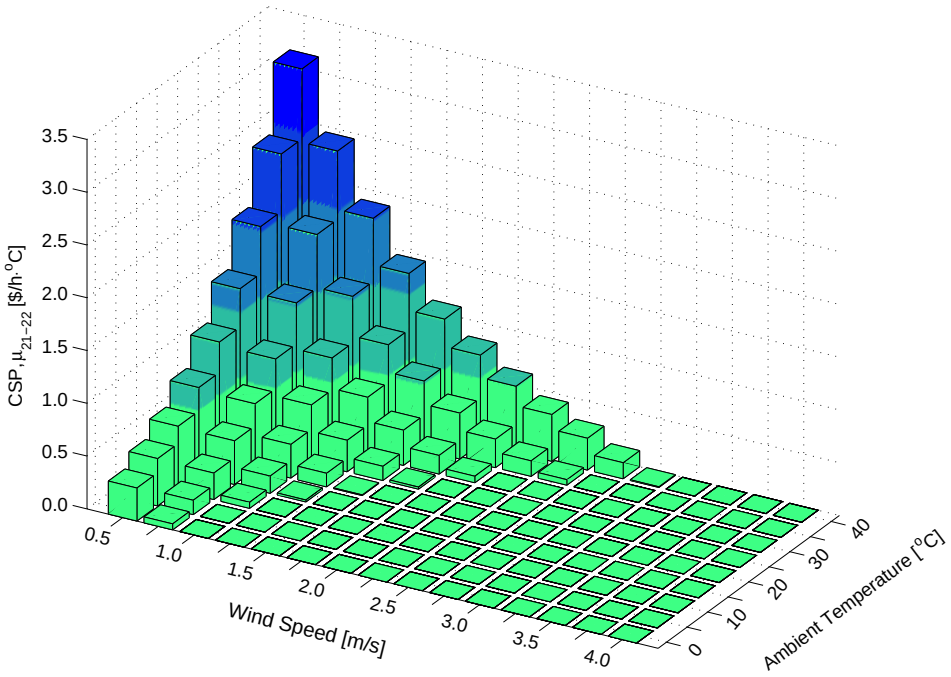

Fig. 6.9: Effect of the measured weather conditions across line 21-22 on the line's congestion shadow price.

the ambient temperature and wind speed across line 21-22. The effect of the monitored ambient temperature on the scheduled IRE generation is shown in Fig. 6.7(a). The plot shows that the scheduled IRE generation at bus 24 is more significantly affected by the value of the ambient temperature, compared to the schedules at buses 5 and 14. At bus 24, the scheduled IRE generation increases as the ambient temperature reduces, whereas the converse is true at buses 5 and 14 to a lesser degree. As observed from Fig. 6.7(b), the overall effect on the objective function value is a reduction, as the ambient temperature decreases. As seen from Fig. 6.8, similar results are obtained with the variation in wind speed. The scheduled IRE generation at bus 24 increases with the increase in wind speed across the monitored conductor; the effect is inverse on the IRE generation at buses 5 and 14. The objective function value reduces as the wind speed increases up to the point, where the maximum conductor temperature constraint is no longer binding.

The operational cost owing to the congestion of line 21-22 is measured by the value of its CSP, μ_{21-22}. Fig. 6.9 shows the variation in μ_{21-22} with the monitored ambient weather conditions, i.e., the ambient temperature, T_a and the wind speed, v. Fig. 6.9 shows that the CSP and hence, the system congestion costs due to the congestion on this line reduce as the conductor cooling conditions improve (T_a reduces and v increases). At $T_a = 40°C$, μ_{21-22} reduces from \$3.14/h·°C at SLR weather conditions to zero, for wind speeds higher than 3.0 m/s. The wind speeds corresponding to the zero congestion costs are even lower, as the ambient temperature decreases.

Computational performance and problem scalability

When compared to the classical OPF solution [34], the problem formulation proposed in this chapter adds extra decision variables in the form of scheduled IRE generation at various buses. In terms of operational constraints, line flow limits for transmission lines whose ambient cooling conditions are monitored require an extra computation of conductor temperature based on ambient weather conditions. Other than the system size (number of buses, conventional generators etc) these extensions add to the problem complexity. An analysis of the complexity in terms of computation time, simulation *Case C* was run for different number of IRE sources and monitored lines. Table 6.6 shows the average time taken by a single iteration of the interior point algorithm used to solve the optimization problem. As deduced from Table 6.6, simulation time increases as the number of IRE

Table 6.6: Average iteration computation time for different number of IRE sources and monitored transmission lines ($\times 10^{-2}$ sec)

No. of monitored lines	No. of IRE sources			
	3	6	9	12
5	1.41	2.36	3.60	4.31
10	1.45	2.41	3.74	4.63
15	1.58	2.60	3.92	4.89
20	1.64	2.76	4.11	5.18

sources and monitored transmission lines increase. The number of IRE sources has a larger influence on the simulation time because the numerical evaluations of the integrals and derivatives takes a longer time. Also, the simplified line temperature model makes evaluations related to the line temperature constraints much faster. The average time taken to run an iteration is shown since different operating conditions converge after different number of iterations. Typically, the simulations whose results are shown in Table 6.6 converged in 10 to 15 iterations.

The scalability of the proposed OPF model to larger systems was tested by running simulations for larger systems i.e. modified versions of the IEEE 118-bus and the PEGASE 1354-bus test systems [37]. In the simulations, IRE sources are introduced in 10% of the buses and the 5% most heavily loaded lines are monitored. The simulation times are shown in Table 6.7. As expected, computation time increases as the network size increases. However, even the PEGASE 1354-bus test system with 1,991 branches takes only about 30 seconds to converge. All calculations were performed on a laptop computer with a 2.40-GHz Intel Core i7 processor running MATLAB 2010a.

Table 6.7: Computation time for systems of different sizes

Test System	No. of conventional generators	No. of IRE sources	No. of monitored transmission lines	No. of iterations	Computation time per iteration [sec]
IEEE 30 – bus	6	3	2	12	0.014
IEEE 118 – bus	54	12	9	16	0.116
PEGASE 1354 – bus	260	135	100	38	0.835

6.6 Remarks on scheduling with conductor temperature constraints

6.6.1 Influence of conductor resistance - temperature dependence

In the problem formulation proposed in this chapter, a constant value of conductor resistance is used in the power flow equations (6.8) even though the resistance of a conductor is dependent on its temperature. In the simulations, the resistance value corresponding to the SLR current is used as a conservative approach. A constant value of R_{ij} is used in (6.8) because current is only slightly dependent on resistance – and hence only slightly dependent on conductor temperature – since X_{ij} is typically much greater than R_{ij}. The effect of this approximation is quantified by re-solving the OPF problem (*Case C*) while incorporating the conductor resistance–temperature dependence in the simulations. This is done using an algorithm that iteratively updates the values of conductor resistance after each OPF solution until the largest change in conductor temperature after successive iterations is less than a pre-defined threshold (set at 0.1°C). Table 6.8 shows the objective function values and simulation times for the cases with and without the conductor

resistance-temperature dependence. As seen from the results, the incorporation of conductor resistance-temperature dependence in the problem formulation considerably increases the simulation time without significantly altering the objective function values.

Table 6.8: Effect of conductor resistance-temperature dependence on OPF solution

Simulation Case C	Constant resistance in power flow	Resistance−temperature dependence in power flow	Difference (%)
Gen. Cost [$/h]	4365.09	4360.32	−0.11%
IRE Cost [$/h]	419.33	416.01	−0.79%
Obj. Fcn. Value [$/h]	4784.41	4776.33	−0.17%
Simulation Time [sec.]	0.172	0.850	+394.2%

6.6.2 Use of forecasted ambient weather conditions

In the simulations presented in this chapter, conductor temperature calculations are done using fixed values of wind speed, wind direction, ambient temperature, and solar radiation. Since OPF calculations are run prior to operation, such values will be forecasted values which – in a manner similar to generation by IRE sources – will exhibit uncertainties. The use of expected values of ambient weather parameters could therefore yield overly optimistic results meaning that care has to be taken with these values. Generally speaking, such uncertainties can be handled in one of two ways: i) safety factors could be applied on the values of the weather parameters used to give a slightly more conservative approach but not as conservative as the use of the SLR. The values of such safety factors would require a prior quantification based on an analysis of the forecast errors; ii) the OPF problem formulation could be modified to a risk based formulation where the risk of transmission line overload is either added as a penalty to the objective function or as a risk constraint.

6.6.3 Problem complexity in extended formulations

The OPF problem formulation presented in this chapter is for a single period OPF problem – typically solved in the short-term (e.g. hour-ahead time period) – whereby the committed generation units are known and IRE forecasts errors are relatively small. An extension of the problem formulation to a multi-period framework that introduces generator ramping limits and binary turn-on and turn-off variables will render the problem non-convex and more difficult to solve. Other newer electricity market characteristics such as combined energy and reserve market clearing, multi-period pricing, and flexible ramping units would add to the problem non-convexity.

6.7 Summary

A new OPF formulation incorporating power generation from IRE sources and explicit maximum conductor-temperature limits was developed and is presented in this chapter. The simplified conductor temperature–current model presented in Chapter 4 was used to easily incorporate the conductor thermal characteristics in the OPF problem formulation. Numerical simulations on standard test systems demonstrated that the IRE sources uncertainty costs and ambient weather conditions across critical conductors significantly affect the optimal schedules obtained from the solution of the OPF problem. In general, the main contributions can be summarized as follows:

1. The thermal characteristics of monitored overhead conductors are incorporated using a simplified version of the heat balance equation (HBE) that retains the dependence of conductor temperature on ambient weather conditions. The simplicity of the HBE model reduces the computational effort and computation time needed for the solution of the difficult OPF problem.
2. The proposed formulation considers not only the cost of conventional generation but also the costs due to uncertainty of IRE sources in the power system. This approach allows a form of control on the levels of uncertainty due to IRE sources that are accepted into the power system.
3. A detailed analysis and discussion of the effects of monitored weather conditions on generation scheduling and related costs is also presented. The scheduled IRE source generation could be higher or lower than the expected value depending on the IRE uncertainty cost coefficient. Also, the location of the IRE source in the system influences its optimal schedule especially in cases where there are large variations in the system LMPs.

In conclusion, conductor-temperature monitoring, through real-time monitoring of the ambient weather conditions around the lines operated at or near their thermal limits, can have significant effects on the resulting generation schedules. The relaxation of the conductor thermal constraints during periods of ambient conditions favorable to conductor cooling allows for use of cheaper transmission network paths and hence a reduction in thermal generation costs. The savings from the reduced system congestion can be used to accommodate more uncertainty in power generation due to IRE sources i.e. a reduction in thermal generation costs allows for an increase in IRE uncertainty costs. This result translates into an increase in IRE utilization. Clearly, the potential operational-cost savings and increased IRE utilization justify the application of conductor-temperature monitoring in power systems.

6.8 References

[1] REN21, "Renewables 2017 Global Status Report," *Paris: REN21 Secretariat*, 2017. Available from: http://www.ren21.net/gsr-2017/.

[2] R. Wang, P. Wang, G. Xiao, and S. Gong, "Power demand and supply management in microgrids with uncertainties of renewable energies," *International Journal of Electrical Power & Energy Systems*, vol. 63, pp. 260 – 269, 2014. doi: https://doi.org/10.1016/j.ijepes.2014.05.067.

[3] M. A. Ortega-Vazquez and D. S. Kirschen, "Estimating the spinning reserve requirements in systems with significant wind power generation penetration," *IEEE Transactions on Power Systems*, vol. 24, pp. 114–124, Feb 2009. doi: https://doi.org/10.1109/TPWRS.2008.2004745.

[4] Živa Bricman Rejc and M. Čepin, "Estimating the additional operating reserve in power systems with installed renewable energy sources," *International Journal of Electrical Power & Energy Systems*, vol. 62, pp. 654 – 664, 2014. doi: https://doi.org/10.1016/j.ijepes.2014.05.019.

[5] R. Doherty and M. O'Malley, "A new approach to quantify reserve demand in systems with significant installed wind capacity," *IEEE Transactions on Power Systems*, vol. 20, pp. 587–595, May 2005. doi: https://doi.org/10.1109/TPWRS.2005.846206.

[6] F. Liu, Z. Bie, S. Liu, and T. Ding, "Day-ahead optimal dispatch for wind integrated power system considering zonal reserve requirements," *Applied Energy*, vol. 188, pp. 399 – 408, 2017. doi: https://doi.org/10.1016/j.apenergy.2016.11.102.

[7] J. Wang, M. Shahidehpour, and Z. Li, "Security-constrained unit commitment with volatile wind power generation," *IEEE Transactions on Power Systems*, vol. 23, pp. 1319–1327, Aug 2008. doi: https://doi.org/10.1109/TPWRS.2008.926719.

[8] F. Bouffard and F. D. Galiana, "Stochastic security for operations planning with significant wind power generation," vol. 23, pp. 306–316, May 2008. doi: https://doi.org/10.1109/TPWRS.2008.919318.

[9] A. Papavasiliou, S. S. Oren, and R. P. O'Neill, "Reserve requirements for wind power integration: A scenario-based stochastic programming framework," *IEEE Transactions on Power Systems*, vol. 26, pp. 2197–2206, Nov 2011. doi: https://doi.org/10.1109/TPWRS.2011.2121095.

[10] L. Chao, Y. Jun, D. Zhi, H. Jifeng, and L. Mingsong, "Day-ahead economic dispatch of wind integrated power system considering optimal scheduling of reserve capacity," *Energy Procedia*, vol. 75, pp. 1044 – 1051, 2015. doi: https://doi.org/10.1016/j.egypro.2015.07.463.

[11] L. Roald, M. Vrakopoulou, F. Oldewurtel, and G. Andersson, "Risk-based optimal power flow with probabilistic guarantees," *International Journal of Electrical Power & Energy Systems*, vol. 72, pp. 66 – 74, 2015. doi: https://doi.org/10.1016/j.ijepes.2015.02.012.

[12] T. Summers, J. Warrington, M. Morari, and J. Lygeros, "Stochastic optimal power flow based on conditional value at risk and distributional robustness," *International Journal of Electrical Power & Energy Systems*, vol. 72, pp. 116 – 125, 2015. doi: https://doi.org/10.1016/j.ijepes.2015.02.024.

[13] R. A. Jabr, "Adjustable robust OPF with renewable energy sources," *IEEE Transactions on Power Systems*, vol. 28, pp. 4742–4751, Nov 2013. doi: https://doi.org/10.1109/TPWRS.2013.2275013.

[14] R. A. Jabr, S. Karaki, and J. A. Korbane, "Robust multi-period OPF with storage and renewables," *IEEE Transactions on Power Systems*, vol. 30, pp. 2790–2799, Sept 2015. doi: https://doi.org/10.1109/TPWRS.2014.2365835.

[15] M. Schlapfer and P. Mancarella, "Probabilistic modeling and simulation of transmission line temperatures under fluctuating power flows," *IEEE Transactions on Power Delivery*, vol. 26, no. 4, pp. 2235–2243, 2011. doi: https://doi.org/10.1109/TPWRD.2011.2145394.

[16] D. A. Douglass, "Weather-dependent versus static thermal line ratings [power overhead lines]," *IEEE Transactions on Power Delivery*, vol. 3, pp. 742–753, Apr 1988. doi: https://doi.org/10.1109/61.4313.

[17] J. Heckenbergerová, P. Musilek, and K. Filimonenkov, "Quantification of gains and risks of static thermal rating based on typical meteorological year," *International Journal of Electrical Power & Energy Systems*, vol. 44, no. 1, pp. 227 – 235, 2013. doi: https://doi.org/10.1016/j.ijepes.2012.07.005.

[18] B. Weedy, "Dynamic current rating of overhead lines," *Electric Power Systems Research*, vol. 16, no. 1, pp. 11 – 15, 1989. doi: https://doi.org/10.1016/0378-7796(89)90032-1.

[19] T. Krontiris, A. Wasserrab, and G. Balzer, "Weather-based loading of overhead lines - consideration of conductor's heat capacity," in *2010 Modern Electric Power Systems*, pp. 1–8, Sept 2010. Available from: https://ieeexplore.ieee.org/iel5/5996359/6007154/06007162.pdf.

[20] G. Kosec, M. Maksić, and V. Djurica, "Dynamic thermal rating of power lines - model and measurements in rainy conditions," *International Journal of Electrical Power & Energy Systems*, vol. 91, no. Supplement C, pp. 222 – 229, 2017. doi: https://doi.org/10.1016/j.ijepes.2017.04.001.

[21] M. Simms and L. Meegahapola, "Comparative analysis of dynamic line rating models and feasibility to minimise energy losses in wind rich power networks," *Energy Conversion and Management*, vol. 75, pp. 11 – 20, 2013. doi: https://doi.org/10.1016/j.enconman.2013.06.003.

[22] S. Uski, "Estimation method for dynamic line rating potential and economic benefits," *International Journal of Electrical Power & Energy Systems*, vol. 65, pp. 76 – 82, 2015. doi: https://doi.org/10.1016/j.ijepes.2014.09.034.

[23] M. Nick, O. Alizadeh-Mousavi, R. Cherkaoui, and M. Paolone, "Security constrained unit commitment with dynamic thermal line rating," *IEEE Transactions on Power Systems*, vol. 31, pp. 2014–2025, May 2016. doi: https://doi.org/10.1109/TPWRS.2015.2445826.

[24] B. Xu, A. Ulbig, and G. Andersson, "Impacts of dynamic line rating on power dispatch performance and grid integration of renewable energy sources," in *IEEE PES ISGT Europe 2013*, pp. 1–5, Oct 2013. doi: https://doi.org/10.1109/ISGTEurope.2013.6695410.

[25] H. Banakar, N. Alguacil, and F. D. Galiana, "Electrothermal coordination part I: theory and implementation schemes," *IEEE Transactions on Power Systems*, vol. 20, pp. 798–805, May 2005. doi: https://doi.org/10.1109/TPWRS.2005.846196.

[26] N. Alguacil, M. H. Banakar, and F. D. Galiana, "Electrothermal coordination part II: case studies," *IEEE Transactions on Power Systems*, vol. 20, pp. 1738–1745, Nov 2005. doi: https://doi.org/10.1109/TPWRS.2005.857836.

[27] M. X. Wang and X. S. Han, "Study on electro-thermal coupling optimal power flow model and its simplification," in *IEEE PES General Meeting*, pp. 1–6, July 2010. doi: https://doi.org/10.1109/PES.2010.5589644.

[28] B. Ngoko, H. Sugihara, and T. Funaki, "Validation of a simplified model for estimating overhead conductor temperatures under dynamic line ratings," *IEEJ Transactions on Power and Energy*, vol. 138, no. 4, pp. 284–296, 2018. doi: https://doi.org/10.1541/ieejpes.138.284.

[29] S. Duman, U. Güvenç, Y. Sönmez, and N. Yörükeren, "Optimal power flow using gravitational search algorithm," *Energy Conversion and Management*, vol. 59, pp. 86 – 95, 2012. doi: https://doi.org/10.1016/j.enconman.2012.02.024.

[30] S. S. Reddy and P. Bijwe, "Day-ahead and real time optimal power flow considering renewable energy resources," *International Journal of Electrical Power & Energy Systems*, vol. 82, no. Supplement C, pp. 400 – 408, 2016. doi: https://doi.org/10.1016/j.ijepes.2016.03.033.

[31] J. Hetzer, D. C. Yu, and K. Bhattarai, "An economic dispatch model incorporating wind power," *IEEE Transactions on Energy Conversion*, vol. 23, pp. 603–611, June 2008. doi: https://doi.org/10.1109/TEC.2007.914171.

[32] University of Washington, "Power system test case archive." Available from http://www.ee.washington.edu/research/pstca/, Accessed: July 17, 2017.

[33] R. W. Ferrero, S. M. Shahidehpour, and V. C. Ramesh, "Transaction analysis in deregulated power systems using game theory," *IEEE Transactions on Power Systems*, vol. 12, pp. 1340–1347, Aug 1997. doi: https://doi.org/10.1109/59.630479.

[34] R. D. Zimmerman, C. E. Murillo-Sanchez, and R. J. Thomas, "Matpower: Steady-state operations, planning, and analysis tools for power systems research and education," *IEEE Transactions on Power Systems*, vol. 26, pp. 12–19, Feb 2011. doi: https://doi.org/10.1109/TPWRS.2010.2051168.

[35] Midal Cables, "Overhead Conductor Data Sheets," 2016. Available from: https://www.midalcable.com/sites/default/files/ACSR-metric.PDF.

[36] W. Weibull, "A statistical distribution function of wide applicability," *ASME Journal of Applied Mechanics*, pp. 293 – 297, 1951. Available from: https://pdfs.semanticscholar.org/88c3/7770028e7ed61180a34d6a837a9a4db3b264.pdf.

[37] C. Josz, S. Fliscounakis, J. Maeght, and P. Panciatici, "AC power flow data in MATPOWER and QCQP format: iTesla, RTE snapshots, and PEGASE," March 2016. arXiv preprint, Available from: https://arxiv.org/abs/1603.01533.

CHAPTER 7

Conclusions

This dissertation focuses on the optimal operation of the power system with a target of increasing the utilization of intermittent renewable energy (IRE) sources i.e. solar PV and wind in the power system. More specifically, a less conservative approach to setting transmission line ratings – referred to as dynamic line rating (DLR) – is studied.

Recent trends in electric power generation point to an increase in power supply by IRE sources. The motivations for this trend include environmental concerns and more cost competitiveness of these sources due to improvements in technology. While there are strong motivations for increased power generation by IRE sources, their fluctuating nature introduces new challenges to the system operator. Traditional power systems are generally relatively predictable as years of operation mean that load forecasting tools are generally very accurate and economic generation scheduling including reserve allocation is simple enough. However, the intermittency of IRE sources increases variability and uncertainty not only in power generation within the network, but also in power flows within various system branches including transmission lines. As a result, there is an increased need for power system researches to propose ways of handling the new operational challenges.

Overall conclusion

The work carried out in this dissertation shows that dynamic line rating of overhead transmission lines – carried out through real-time temperature monitoring of the conductors (either directly or indirectly) – can lead to a more economic operation of a power system that has significant power generation from intermittent renewable energy sources. Simulations carried out on a test power system shows a 2.4% reduction in operational costs realized by relaxing the conservativeness of the traditional static line rating on heavily loaded transmission lines. Moreover, the reduced thermal generation costs resulting from less transmission congestion in the system allows for increased "uncertainty costs" due to fluctuating IRE sources. Allowing more uncertainty in the system increases the utilizable IRE generation. Simulations show a 19.1% increase in scheduled IRE generation for the chosen test system.

Itemized conclusions

The main work carried out in this thesis can be categorized into three main topics: (1) probabilistic modeling of IRE generation, specifically PV generation, for synthetically generating solar PV scenarios in probabilistic studies of the power system; (2) proposing a simplified overhead conductor temperature model for integration in system operation tools using DLRs; and (3) developing a new optimal power flow model with explicit conductor temperature limits with the specific target of handling the uncertainty due to IRE sources. The conclusions from these three main topics can be summarized as follows:

1. **Probabilistic model for solar PV power (Chapter 3)**

   An empirical probabilistic model for high temporal resolution (1-minute) solar radiation data which can be used to simulate fluctuations in solar PV generation is developed. The model is constructed by treating the process generating a normalized form of the 1-minute clearness index as a second-order Markov process. Model construction details including data trend removal and model order selection are discussed in the text.

   Conclusions drawn from a comparison of data synthetically generated using the proposed model and actual 1-minute solar irradiation data include:

   - The ordinary moments i.e. mean, standard deviation, skewness, and kurtosis are well reproduced by the proposed Markov model.
   - The probability distribution plots are also well matched. Significantly, the proposed model reproduces the bimodal distribution characteristic of the 1-minute irradiation data that would not be reproduced by a typical ARMA model.
   - The autocorrelation characteristics of the observed and synthetic data sets are well matched including the significant lag-2 partial autocorrelation for cloudy days i.e. days with a clearness index less than 0.3.
   - The minute-to-minute fluctuations in solar irradiation are also well reproduced. The highest percentage of large fluctuations (defined as 1-minute fluctuations larger than 200 W/m^2) is found to be about 3% and occurs on moderately cloudy days i.e. days with a clearness index between 0.45 and 0.6.

   The proposed model can be a fundamental tool for probabilistic studies of the power system specifically regarding the effects of increased integration of PV power generation.

2. **Simplified overhead conductor temperature model (Chapter 4)**

   A simple mathematical model for estimating the temperature of an overhead conductor under varying weather conditions is developed and verified. The model is developed by proposing approximations to various components of the more complex CIGRE conductor temperature model. The proposed model is verified by both numerical and experimental methods.

   A comparison of measured conductor temperature with values calculated using both the original CIGRE model and the simplified version lead to the following conclusions:

- Approximation errors in conductor temperature determination using the simplified model when compared to the full CIGRE model are within 3°C in both steady state and transient state.
- Measured conductor temperature values are well matched with the model values at high wind speeds. However, the measurements were slightly higher for low wind speeds.
- Since the simplified model is developed from a slightly conservative point of view, it gives lower time constants than both the CIGRE model and lab measured values.
- The simplified model reduces the computation effort in conductor temperature calculation and realizes significant computation time savings when compared with the full CIGRE model. Simulations showed that the CIGRE model takes on average 4.5 times longer than the simplified model to complete a single conductor temperature calculation.

The proposed model is applied in a new optimal power flow (OPF) formulation and improves the tractability of the OPF solution algorithm.

3. Optimal power flow with DLR and IRE generation (Chapter 6)

A new formulation of the optimal power flow (OPF) problem incorporating the thermal characteristics of overhead conductors for a system with significant IRE-source generation is proposed. One of the main extensions proposed in the new OPF formulation is the incorporation of costs due to IRE uncertainty modeled as a function of expected IRE power overestimation. Also, instead of the traditional conductor current limits, conductor temperature limits are applied explicitly in the OPF problem formulation whereby conductor temperature is calculated using a simplified conductor temperature model based on monitored weather conditions.

The following conclusions are drawn from numerical simulations carried out on a modified version of the standard IEEE 30-bus test system with IRE generation at several buses:

- Monitoring of ambient weather conditions around lines operated at or near their thermal limits significantly improves the OPF solution. In the simulations, there is a 2.4% reduction in the objective function value (power supply costs) when assumed actual weather parameters are used as compared to the conventional static line rating.
- The use of monitored weather parameters (i.e. DLR) allows for increased uncertainty in power supply which results in increased utilization of IRE generation. In the simulations, the relaxation of the line thermal limits results in a 19.1% increase in scheduled generation by IRE sources.
- Various sensitivity analyses carried out show that the monitored weather conditions and the unit cost of IRE uncertainty have a significant effect on the OPF solutions.

- The application of the simplified conductor temperature model significantly reduces the OPF problem solution time.

Apart from these main topics, other applications of more flexibility in transmission line ratings were also carried out. The conclusions from these are summarized as:

i. A real-time transmission line rating for handling IRE fluctuations (Section 5.4)

A short-term transient rating which incorporates both conductor thermal dynamics and changes in ambient weather conditions is proposed. The rating, referred to as dynamic electro-thermal rating (DETR), gives line loadability limits that are less conservative than the classic DLR.

Simulation results show that the DETR would allow for higher fluctuations in conductor current as compared to the steady-state DLR and can therefore be especially useful for conductors that experience large power fluctuations due to increased IRE generation. Simulations on a simple two-bus system shows a 37% reduction in current curtailment when a 15-min DETR is used when compared to the DLR. The reduction in current curtailment increases to 91% when the much faster 5-min DETR is used.

ii. Secure operation of transmission lines with DLRs (Section 5.5)

A methodology for determining DLR safety factors that ensure a safe operation of transmission lines is illustrated. A risky operation of the transmission line is defined as having a forecasted value of line rating that may be higher than the actual line rating due to uncertainties in ambient weather forecasts. In order to avoid such risky operations, DLR safety factors are estimated.

Numerical simulations using actual weather data result in safety factor values of around 0.86 for 5-minute (transient-state) ratings and 0.75 for 30-minute (steady-state) ratings corresponding to 0.1% risk levels. However, even with these safety factors there is still a 33% increase in line loadability for the 30-minute DLR and a 77% increase in line loadability for the 5-minute DLR.

iii. Transmission line overload risk assessment with DLRs (Section 5.6)

An assessment of line overload risk in a system with significant IRE generation is illustrated. The risk assessment methodology uses probabilistic models of ambient weather conditions around the transmission lines to determine the probability of violating the maximum conductor temperature limit rather than the traditional maximum conductor current limit.

Simulations carried out on a simple two-bus test system shows the possible trade-off between thermal generation costs and line overload risk. For example, a 1% increase in line overload risk would produce a 3% reduction in thermal generation costs. The application of the simplified conductor temperature model coupled with a linear power flow model in the risk assessment procedure results in significant computation time savings.

APPENDIX A

Publications

Journal papers

1. **B.O. Ngoko**, H. Sugihara, and T. Funaki, "Optimal power flow considering line-conductor temperature limits under high penetration of intermittent renewable energy sources," *International Journal of Electrical Power & Energy Systems*, vol. 101, pp. 255 - 267, October, 2018 (in press).

2. **B.O. Ngoko**, H. Sugihara, and T. Funaki, "Validation of a simplified model for estimating overhead conductor temperatures under dynamic line ratings - comparison with the CIGRE model," *IEEJ Transactions on Power and Energy*, vol. 138, No. 4, pp. 284 - 296, April, 2018.

3. **B.O. Ngoko**, H. Sugihara, and T. Funaki, "Synthetic generation of high temporal resolution solar radiation data using Markov models," *Solar Energy*, vol. 103, pp. 160 - 170, May, 2014.

International conference proceedings

1. **B.O. Ngoko**, H. Sugihara, and T. Funaki, "Effect of dynamic line ratings on optimal dispatch considering uncertainty costs due to intermittent renewable energy," *to be presented at the 10^{th} Symposium on Control of Power and Energy Systems (CPES2018)*, Tokyo, Japan, September, 2018.

2. **B.O. Ngoko**, H. Sugihara, and T. Funaki, "Methodology for the determination of real-time dynamic line ratings for secure operation of overhead conductors," *in 2017 IEEE PES Innovative Smart Grid Technologies Conference Europe (ISGT-Europe)*, Torino, Italy, pp. 1 – 6, September, 2017.

3. **B.O. Ngoko**, H. Sugihara, and T. Funaki, "A short-term dynamic thermal rating for accommodating increased fluctuations in conductor current due to intermittent renewable energy," *in 2016 IEEE PES Asia-Pacific Power and Energy Engineering Conference (APPEEC)*, Xi'an, China, pp. 141 – 145, October, 2016.

Domestic conference proceedings

1. **B.O. Ngoko**, H. Sugihara, and T. Funaki, "Transmission line overload risk assessment based on a simplified conductor temperature model," *to be presented at the 2018 Annual Conference of Power & Energy Society IEE of Japan*, Tokushima, Japan, September, 2018.

2. **B.O. Ngoko**, H. Sugihara, and T. Funaki, "Experimental validation of a simplified model for calculating the temperature of overhead conductors under dynamic line ratings," *in Proceedings of the 2018 IEE of Japan Annual Conference*, Kyushu, Japan, March, 2018.

3. **B.O. Ngoko**, H. Sugihara, and T. Funaki, "Analyzing the effects of temperature–dependent overhead line resistance on the optimal power flow solution with dynamic line ratings," *in Proceedings of the 2017 IEE of Japan Annual Conference*, Toyama, Japan, March, 2017.

4. **B.O. Ngoko**, H. Sugihara, and T. Funaki, "A simplified model and its validation for estimating overhead conductor temperature under dynamic line ratings," *in Proceedings of the 2016 Annual Conference of Power & Energy Society IEE of Japan*, Kyushu, Japan, September, 2016.

5. **B.O. Ngoko**, H. Sugihara, and T. Funaki, "Synthetic generation of solar radiation data using Markov models for power system studies," *in Proceedings of the 2012 Kansai-section Joint Convention of Institutes of Electrical Engineering*, Osaka, Japan, July, 2012.

APPENDIX B

Calculation of statistical moments

The following formulae are used to calculate the mean, standard deviation, skewness and kurtosis of k'_t.

1. *Mean*

   The mean μ of k'_t is given by:

   $$\mu = \frac{\sum_{t=1}^{N} k'_t}{N} \tag{B.1}$$

   where N is the number of observations.

2. *Standard Deviation*

   The standard deviation σ of k'_t is given by:

   $$\sigma = \sqrt{\frac{1}{N}\sum_{t=1}^{N}\left(k'_t - \mu\right)^2} \tag{B.2}$$

3. *Skewness*

   The skewness γ_1 of k'_t is given by:

   $$\gamma_1 = \frac{m_3}{m_2^{3/2}} = \frac{\frac{1}{N}\sum_{t=1}^{N}\left(k'_t - \mu\right)^3}{\left(\frac{1}{N}\sum_{t=1}^{N}\left(k'_t - \mu\right)^2\right)^{3/2}} \tag{B.3}$$

   where m_3 is the third central moment and m_2 is the variance $\left(\sigma^2\right)$.

4. *Kurtosis*

   The kurtosis γ_2 of k'_t is given by:

   $$\gamma_2 = \frac{m_4}{m_2^2} - 3 = \frac{\frac{1}{N}\sum_{t=1}^{N}\left(k'_t - \mu\right)^4}{\left(\frac{1}{N}\sum_{t=1}^{N}\left(k'_t - \mu\right)^2\right)^2} - 3 \tag{B.4}$$

   where m_4 is the fourth central moment and m_2 is the variance $\left(\sigma^2\right)$. The -3 at the end of the formula is a correction used to make the kurtosis of the normal distribution equal to zero.

APPENDIX C

Solar geometry fundamentals

The instantaneous solar radiation intensity outside the earth's atmosphere also known as the instantaneous extraterrestrial solar radiation intensity H_e in $\mathrm{W/m^2}$ directly above a given location on the earth at a given time instant is given by:

$$H_e = RE_{sc} \sin h_s \qquad \left[\mathrm{W/m^2}\right]. \tag{C.1}$$

where R is the sun-earth correction factor, $E_{sc} = 1367$ $\mathrm{W/m^2}$ is the solar constant, and h_s is the solar elevation angle.

- R is given by:

$$R = \left(\frac{r_0}{r}\right)^2 \tag{C.2}$$

  where r/r_0 is the earth-sun distance approximated by:

$$\frac{r}{r_0} = \left[1 + 0.034 \cos\left(\frac{360 d_n}{365}\right)\right]^{-1/2} \tag{C.3}$$

  where d_n is the day number ($d_{Jan1} = 1, d_{Feb1} = 32, \dots$).

- E_{sc} is the average solar radiation intensity falling on an imaginary surface perpendicular to the sun's rays and at the edge of the earth's atmosphere. An approximate value of 1367 $\mathrm{W/m^2}$ is normally used.

- h_s is given by:

$$h_s = \sin^{-1}\left(\cos\omega \cos\delta \cos\theta + \sin\delta \sin\theta\right) \tag{C.4}$$

  where ω is the hour angle, δ is the declination angle, and θ is the local latitude.

  - ω is 0° at solar noon i.e. when the sun is directly above the local longitude. The hour angles before the solar noon are negative while those after the solar noon are positive.

    The solar time differs from the local clock time by Δt minutes:

$$\Delta t = 4 \times (\Lambda_{loc} - \Lambda_{std}) \tag{C.5}$$

    where Λ_{loc} is the local longitude and Λ_{std} is the standard longitude from which the clocks are set.

Also, the solar time changes slightly with respect to local standard time. This time difference is called the *equation of time* (EOT) approximated by:

$$EOT = 9.87 \sin 2x - 7.53 \cos x - 1.5 \sin x \tag{C.6}$$

where $x = 2\pi(d_n - 81)/364$.

Therefore the solar time (in hours) is given by:

$$T_s = T_l + (\Delta_t + EOT)/60 \tag{C.7}$$

and ω (in radians) is then given by:

$$\omega = \pi (T_s - 12)/12 \tag{C.8}$$

- δ is approximated by:

$$\delta = 0.40928 \sin \left(\frac{2\pi (d_n - 81)}{365} \right) \tag{C.9}$$

The zenith angle is obtained from the solar elevation angles by:

$$z = \pi/2 - h_s \tag{C.10}$$

Fig. C.1 depicts the solar elevation angle and the zenith angle.

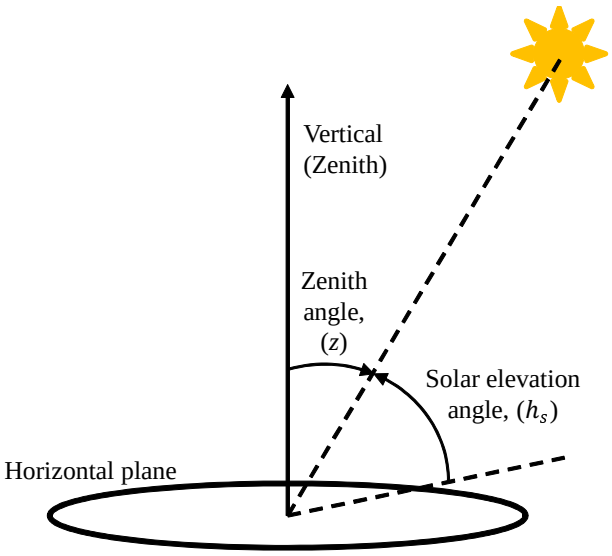

Fig. C.1: Solar elevation and zenith angles.

APPENDIX D

Test system data

Table D.1: IEEE 30-bus test system: Bus and load data

Bus no.	bus type*	P_d (MW)	Q_d (MVAr)	V_{max} (p.u.)	V_{min} (p.u.)
1	3	0.0	0.0	1.05	0.95
2	2	21.7	12.7	1.10	0.95
3	1	2.4	1.2	1.05	0.95
4	1	7.6	1.6	1.05	0.95
5	1	0.0	0.0	1.05	0.95
6	1	0.0	0.0	1.05	0.95
7	1	22.8	10.9	1.05	0.95
8	1	30.0	30.0	1.05	0.95
9	1	0.0	0.0	1.05	0.95
10	1	5.8	2.0	1.05	0.95
11	1	0.0	0.0	1.05	0.95
12	1	11.2	7.5	1.05	0.95
13	2	0.0	0.0	1.10	0.95
14	1	6.2	1.6	1.05	0.95
15	1	8.2	2.5	1.05	0.95
16	1	3.5	1.8	1.05	0.95
17	1	9.0	5.8	1.05	0.95
18	1	3.2	0.9	1.05	0.95
19	1	9.5	3.4	1.05	0.95
20	1	2.2	0.7	1.05	0.95
21	1	17.5	11.2	1.05	0.95
22	2	0.0	0.0	1.10	0.95
23	2	3.2	1.6	1.10	0.95
24	1	8.7	6.7	1.05	0.95
25	1	0.0	0.0	1.05	0.95
26	1	3.5	2.3	1.05	0.95
27	2	0.0	0.0	1.10	0.95
28	1	0.0	0.0	1.05	0.95
29	1	2.4	0.9	1.05	0.95
30	1	10.6	1.9	1.05	0.95

*for the bus types: 1 - load bus; 2 - PV (generator) bus; and 3 - slack (reference) bus

Table D.2: IEEE 30-bus test system: Branch data

Line no.	from bus	to bus	series impedance		half charging susceptance (p.u.)
			R (p.u.)	X (p.u.)	
1	1	2	0.02	0.06	0.03
2	1	3	0.05	0.19	0.02
3	2	4	0.06	0.17	0.02
4	3	4	0.01	0.04	0.00
5	2	5	0.05	0.20	0.02
6	2	6	0.06	0.18	0.02
7	4	6	0.01	0.04	0.00
8	5	7	0.05	0.12	0.01
9	6	7	0.03	0.08	0.01
10	6	8	0.01	0.04	0.00
11	6	9	0.00	0.21	0.00
12	6	10	0.00	0.56	0.00
13	9	11	0.00	0.21	0.00
14	9	10	0.00	0.11	0.00
15	4	12	0.00	0.26	0.00
16	12	13	0.00	0.14	0.00
17	12	14	0.12	0.26	0.00
18	12	15	0.07	0.13	0.00
19	12	16	0.09	0.20	0.00
20	14	15	0.22	0.20	0.00
21	16	17	0.08	0.19	0.00
22	15	18	0.11	0.22	0.00
23	18	19	0.06	0.13	0.00
24	19	20	0.03	0.07	0.00
25	10	20	0.09	0.21	0.00
26	10	17	0.03	0.08	0.00
27	10	21	0.03	0.07	0.00
28	10	22	0.07	0.15	0.00
29	21	22	0.01	0.02	0.00
30	15	23	0.10	0.20	0.00
31	22	24	0.12	0.18	0.00
32	23	24	0.13	0.27	0.00
33	24	25	0.19	0.33	0.00
34	25	26	0.25	0.38	0.00
35	25	27	0.11	0.21	0.00
36	28	27	0.00	0.40	0.00
37	27	29	0.22	0.42	0.00
38	27	30	0.32	0.60	0.00
39	29	30	0.24	0.45	0.00
40	8	28	0.06	0.20	0.02
41	6	28	0.02	0.06	0.01